

ESD ACCESSION LIST

DRI Call No. 88368

Copy No. 1 of 2 cys.

ESD-TR-77-268
Final Report
August 1977

FILE COPY

ANALYSIS OF DISTRIBUTED-EMISSION
CROSSED-FIELD AMPLIFIERS

Prepared by

Shared Applications, Inc.
Ann Arbor, Michigan 48104

Prepared for

Massachusetts Institute of Technology
Lincoln Laboratory

Under Purchase Order No. CX-1256

Prime Contract F19628-76-C-0002

ARPA Order 600

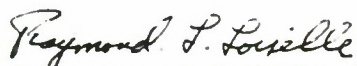
Approved for public release;
distribution unlimited.

ADA050185

The views and conclusions contained in this document are those of the contractor and should not be interpreted as necessarily representing the official policies, either expressed or implied, of the United States Government.

This technical report has been reviewed and is approved for publication.

FOR THE COMMANDER



Raymond L. Loiselle, Lt. Col., USAF
Chief, ESD Lincoln Laboratory Project Office

REPORT DOCUMENTATION PAGE		READ INSTRUCTIONS BEFORE COMPLETING FORM
1. REPORT NUMBER ESD-TR-77-268	2. GOVT ACCESSION NO.	3. RECIPIENT'S CATALOG NUMBER
4. TITLE (and Subtitle) Analysis of Distributed-Emission Crossed-Field Amplifiers		5. TYPE OF REPORT & PERIOD COVERED Final Report
		6. PERFORMING ORG. REPORT NUMBER
7. AUTHOR(s) Dr. Donald M. MacGregor Dr. Joseph E. Rowe		8. CONTRACT OR GRANT NUMBER(s) F19628-76-C-0002
9. PERFORMING ORGANIZATION NAME AND ADDRESS Shared Applications, Inc. under Purchase Order No. CX-1256 to M.I.T. Lincoln Laboratory		10. PROGRAM ELEMENT, PROJECT, TASK AREA & WORK UNIT NUMBERS: ARPA Order 600 Program Element No. 62301E Project No. 7E20
11. CONTROLLING OFFICE NAME AND ADDRESS Defense Advanced Research Projects Agency 1400 Wilson Boulevard Arlington, VA 22209		12. REPORT DATE August 1977
		13. NUMBER OF PAGES 136
14. MONITORING AGENCY NAME & ADDRESS (if different from Controlling Office) Electronic Systems Division Hanscom AFB Bedford, MA 01731		15. SECURITY CLASS. (of this report) Unclassified
		15a. DECLASSIFICATION DOWNGRADING SCHEDULE
16. DISTRIBUTION STATEMENT (of this Report) Approved for public release; distribution unlimited.		
17. DISTRIBUTION STATEMENT (of the abstract entered in Block 20, if different from Report)		
18. SUPPLEMENTARY NOTES None		
19. KEY WORDS (Continue on reverse side if necessary and identify by block number)		
computer simulation amplifiers tubes		electron dynamics RF power
20. ABSTRACT (Continue on reverse side if necessary and identify by block number) Computer simulation has been used to aid in the development of the Raytheon QKS 1705 and QKS 1842 backward-wave distributed-emission crossed-field amplifiers. At present, Shared Applications, inc. models a reentrant tube with a planar electrode configuration. The results give insight into the electron dynamics and show good qualitative agreement with measurements. Apparently no steady RF state exists; instead the output power and anode current fluctuate by several percent over the transit time around the tube (fifteen RF periods). To simulate a backward-wave amplifier with the planar model, it is necessary to supply an estimate of RF output power and derive the RF drive power. An alternative cylindrical model has demonstrated the ballistic starting mechanisms in the CFA. This model is capable of including the space-charge forces and the complete RF interaction in both forward- and backward-wave tubes and is recommended for further development.		

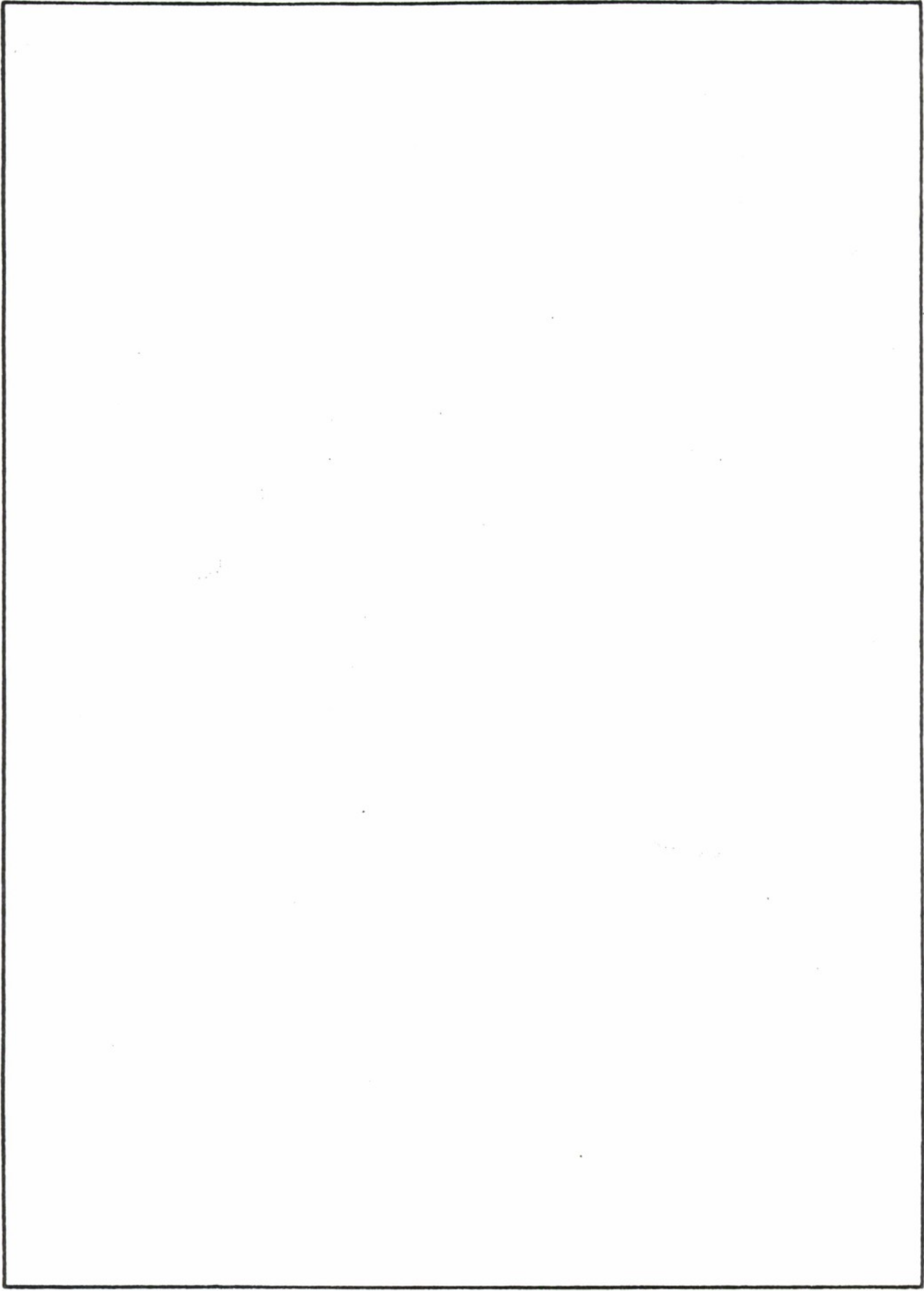


TABLE OF CONTENTS

	<u>Page</u>
LIST OF ILLUSTRATIONS	v
LIST OF TABLES	vii
I. INTRODUCTION	1
II. COMPUTED RESULTS FOR THE QKS 1842	2
A. Numerical Results	2
B. Charge Distribution	6
C. Power Balance	6
D. Secondary Emission	9
E. Hartree Voltage	11
F. RF Synchronism	13
G. Time-Dependent Effects	16
III. VARIATION OF FREQUENCY IN THE QKS 1705 CFA	17
IV. RESULTS FOR THE VARIAN SFD-243 FORWARD-WAVE CFA	27
V. RF PHASE DELAY	30
VI. THE OFF-CENTER CATHODE	35
VII. MODIFIED CIRCUIT EQUATIONS	40
VIII. PROGRAM TESTS WITH A REDUCED TIME STEP AND INCREASED NUMBER OF RODS AND MODIFIED MOTION EQUATIONS	42
IX. STARTING CONDITIONS	51
A. Introduction	51
B. Experimental Results	52
C. Analytical Theory	52
D. Cylindrical Ballistic Computation	59
E. Other Starting Mechanisms	69
F. Conclusions	70
X. ALTERNATIVE SIMULATION METHODS	71
A. Statement of the Problem	71
B. Time-Dependent Simulation	72
C. Iterative Procedure	75
D. Assumptions and Approximations	79
E. Proposed Cylindrical Model	85

	<u>Page</u>
XI. COMPUTATION TIME AND COST	88
XII. SUMMARY AND CONCLUSIONS	91
A. General Objectives	91
B. Comparison of the QKS 1705 and QKS 1842 Tubes	92
C. Summary of Results	93
D. Further Work Proposed	95
APPENDIX A: POWER-TRANSFER EQUATIONS FOR THE RF CIRCUIT IN A CFA	96
APPENDIX B: LINEARIZED TRANSMISSION-LINE EQUATIONS	107
APPENDIX C: EQUATIONS OF MOTION WITH RECTANGULAR GEOMETRY	112
APPENDIX D: EQUATIONS OF MOTION WITH CYLINDRICAL GEOMETRY	115
APPENDIX E: RF-CIRCUIT FIELDS IN THE CYLINDRICAL CFA MODEL	118
REFERENCES	125

LIST OF ILLUSTRATIONS

<u>Figure</u>		<u>Page</u>
1	Computed Charge Distribution near the RF Output of the QKS 1842 DECFA	7
2	Computed Phase Lag of RF Circuit Current from RF Circuit Voltage Around Backward-Wave DECFA	14
3	Computed Gain vs. Distance Around the Backward-Wave DECFA	15
4	RF Gain Computed over Two Cycles Around Backward-Wave DECFA	21
5	Computed Phase Lag of RF Circuit Current from RF Circuit Voltage for Two Cycles Around Backward-Wave DECFA	22
6	Charge Distribution Computed near RF Output of Forward-Wave DECFA	31
7	RF Gain Computed over Two Cycles Around Forward-Wave DECFA	32
8	RF Current Phase Lag from RF Voltage Computed for Two Cycles Around the DECFA Circuit	33
9	Computed RF Current Phase Lag in Backward-Wave CFA for Cycle 3 with Cathode (a) Centered, (b) Shifted away from, (c) Shifted Toward RF Output	39
10	Computed RF Gain in Backward-Wave CFA for Cycle 3 with Cathode (a) Centered, (b) Shifted away from, (c) Shifted Toward RF Output	41
11	Computed RF Current Phase Lag in Backward-Wave CFA with 6,787 Simulation Rods	46
12	Computed RF Current Phase Lag in the QKS 1842 with Amended Equations of Motion	49
13	Methods of Assigning the Charge of a Particle on a Difference Mesh for the Solution of Poisson's Equation	50
14	Measured Minimum RF Drive Power for Starting the QKS 1705 at Various Frequencies and Magnetic Fields	53

		<u>Page</u>
15	Computed and Analytical Cathode Back-bombardment Energy in the QKS 1842 at 9.75 GHz	61
16	Computed and Analytical Phase Gain per Emission-Impact Cycle in the QKS 1842	63
17	Computed Cathode Impact Energy as a Function of Frequency and Magnetic Field in the QKS 1705 with 10 kW RF Drive	66
18	Computed Phase Gain per Impact on Cathode in the QKS 1705	68
19	Comparisons of Dependent and Independent Variables in the CFA and the Simulation Models	76
E.1	Comparison of Exact Values and Single Space Harmonic of RF-Circuit Fields in the QKS 1842 at Radius 9.2 mm	122
E.2	Comparison of Exact Values and Single Space Harmonic of RF-Circuit Fields in the QKS 1842 at 9.6 mm	123
E.3	Comparison of Exact Values and Single Space Harmonic of RF-Circuit Fields in the Sever Region of the QKS 1842	124

LIST OF TABLES

<u>Table</u>		<u>Page</u>
1	QKS 1842 Measured Performance	4
2	Computed and Measured Results for the QKS 1842 at 9.75 GHz (Backward-Wave Interaction)	5
3	Computed Power Balance in the QKS 1842 at 24.3 kV	8
4	Anode and Hartree Voltages in the QKS 1842 at 9.75 GHz	12
5	Measured Current, Voltage and RF Power for the QKS 1705 over the Operating Frequency Band	18
6	Results for the QKS 1705 CFA Computed with 0.35 T Magnetic Field	20
7	Computed Power Balance in the QKS 1705 at Operating Frequency Band	23
8	Measured Power Balance in the QKS 1705	24
9	Parameter Variations with Frequency in the QKS 1705	26
10	Comparison of the SFD-243, QKS 1705 and QKS 1842 Operating Data	28
11	Computed Results for the SFD-243 CFA with 0.224 T Magnetic Field (Forward-Wave Interaction)	29
12	Computed Results for the QKS 1842 with Varied Cathode Position	37
13	Comparison of Results for Two RF-Circuit Models	43
14	Comparisons of Time Step and Rod Size in the QKS 1842 Simulation at 24.3 kV	45
15	Computed Results in the QKS 1842 at 24.3 kV Before and After Amendment of Equations of Motion	48
16	Operating Voltages and Magnetic Fields Used for Measuring Starting Conditions in the QKS 1705 CFA	54

		<u>Page</u>
17	Calculated and Measured RF Drive Powers for Starting the QKS 1705 and QKS 1842 CFA's	58
18	Computed and Analytical Cathode Impact Energy and Phase Gain in the QKS 1842	62
19	Computed Results for the QKS 1842 at 24.3 kV with Integration in the Direction of Power Gain	74
20	Iterated Anode Current and RF Output Power in the QKS 1842 for Two Values of Impedance	78
21	Computer Comparison for DECFA Simulation with 300 Time Steps and a Maximum 4,000 Rods	89

ANALYSIS OF DISTRIBUTED-EMISSION CROSSED-FIELD AMPLIFIERS

I. Introduction

This final report describes the work performed by Shared Applications, Inc. toward the computer simulation of distributed-emission crossed-field amplifiers since the previous report¹ of January 1977, and summarizes the results of the entire project.

The Raytheon Company Microwave and Power Tube Division, Waltham, Massachusetts, is manufacturing the QKS 1842 tube to provide 175 kW peak output power over a narrow bandwidth with 5.5 kW of RF drive. Consequently, the effort at SAI has been directed toward improved simulation of the QKS 1842 at a single frequency of 9.75 GHz (see Section II). This report also describes earlier results for the QKS 1705 over the 9.5-10 GHz frequency band (Section III) and contrasts the computed behavior of the backward-wave CFA's with that of a forward-wave CFA, the Varian SFD-243 (Section IV).

A physical explanation for the hot-to-cold variation of the RF-circuit phase delay (Section V) shows that the measured delay is increased if the RF circuit current lags the RF voltage wave and is reduced if the RF current leads. The measured delay is seen externally to act in the forward-wave direction in both forward- and backward-wave tubes.

An investigation of the off-center cathode (Section VI) yielded predictions of greater RF gain and greater anode

current but reduced efficiency. Tests of the program with ten and twenty steps per cyclotron period, up to 6,787 simulation particles, and alternative RF-circuit and motion equations show that model refinement gives quantitative improvement at the penalty of increased computational cost (Sections VII and VIII, Appendices A, B and C). For qualitative purposes, however, the 4,000-rod model with twenty time steps per cyclotron period is considered adequate.

The starting conditions in a cold-cathode CFA are being treated as a separate problem from the steady-state operation. The analytical ballistic theory of Shaw² has been applied to the Raytheon tubes. However, the results show only partial agreement with measurement (Section IX). A full ballistic computation in cylindrical geometry (Appendices D and E) gives similar results to Shaw's theory.

Section X describes alternative methods that SAI has tested for deriving the RF output power in the backward-wave tube instead of supplying this as an input variable as is done at present. The model of the entire reentrant tube, developed in this study for the ballistic starting calculations, has considerable potential, and the computer capacity for a larger simulation program of this type is considered in Section XI. Section XII reviews the work of the project.

II. Computed Results for the QKS 1842

A. Numerical Results. Simulation runs have been performed for the QKS 1842 using the voltage and RF power

levels supplied by Raytheon and shown in Table 1. The results (Table 2) show at least good qualitative agreement with measured values and clarify the physical mechanisms acting in the tube.

Adjustments to the parameters supplied to the program are as follows:

1. The magnetic field is reduced to compensate for the rectangular geometry (the experimental device has cylindrical geometry), with the value chosen to provide near synchronism of the RF current and voltage on the circuit.
2. The RF impedance is doubled to 15Ω from the measured value of 7.5Ω in order to increase the computed gain to a realistic value.
3. Twenty time steps per cyclotron period are used.
4. The maximum number of simulation rods allowed is 4,000. (The number actually interacting varies during the run approximately between 2,000 and 3,000.)
5. For the first cycle around the tube, a Brillouin hub beam is injected. The tabulated results are averages over three subsequent cycles.

In these runs, the RF output power is supplied and the RF input power derived from a stepwise integration around the tube following the beam. Although the measured RF drive values of 5 kW are not reached in the calculations, it is noteworthy that the computed anode currents are close to the measured values. In the QKS 1705 runs described in the SAI progress report,³ the computed anode currents are too

TABLE 1
QKS 1842 MEASURED PERFORMANCE

RF Drive Power 5.5 kW
Frequency 9.75 GHz

<u>Tube Number*</u>	<u>Magnetic Field (T)</u>	<u>Anode-Sole Voltage (kV)</u>	<u>Anode Current (A)</u>	<u>RF Output Power (kW)</u>
Not known	0.4114	25.5	17.1	175.0
8A	0.4114	24.3	17.1	168.0
8A	0.3788	22.2	15.0	124.0

*Raytheon supplied two sets of data: no tube number was given with first set supplied in September 1976; data for Tube 8A were supplied in January 1977.

TABLE 2

COMPUTED AND MEASURED RESULTS FOR THE QKS 1842
 AT 9.75 GHz (BACKWARD-WAVE INTERACTION)

	<u>High</u> Magnetic Field	<u>Intermediate</u> Magnetic Field	<u>Low</u> Magnetic Field
Input Data			
Magnetic field, T	0.37	0.35	0.322
Anode-sole voltage, V	25.5	24.3	22.2
RF impedance, Ω	15.0	15.0	15.0
RF output power, kW	175.0	168.0	124.0
Computed			
(3-cycle averages)			
Anode current, A	17.67	16.25	16.59
RF drive, kW	18.291	23.546	7.228
RF gain, dB	9.81	8.53	12.34
Efficiency, %	34.78	36.58	31.71
Measured			
Magnetic field, T	0.4114	0.4114	0.3788
Anode current, A	17.1	17.1	15.0
RF drive, kW	5.5	5.5	5.5
RF impedance, Ω	7.5	7.5	7.5
Efficiency, %	38.87	39.11	35.59

high by a factor of up to 1.5 and a beam width correction appears necessary. No experimental information is yet available to explain the necessity for a width correction factor or total current correction factor in the case of the QKS 1705.

B. Charge Distribution. Figure 1 shows a typical charge distribution near the output of the QKS 1842. From such results it is estimated that the charge density exceeds one-fourth the Brillouin density over more than three-fourths of the anode-sole region, but is less than the full Brillouin density in both the QKS 1705 and QKS 1842 tubes. The spreading of the beam over most of the anode-sole region increases the anode bombardment during all parts of the RF cycle, whether favorable or unfavorable for power transfer to the circuit and, hence, limits the efficiency of the tube. Clearly, the simple model of rotating spokes of charge is unrealistic.

C. Power Balance. The power balance (Table 3) shows the computed anode and sole heating with all values averaged over three cycles. The differences in the totals are due in part to the coarseness of the model and also to variations in the flow of beam kinetic energy and the rate of supply of beam potential energy between successive cycles. About 59 percent of the direct input power is dissipated on the anode and 9 percent on the sole (with the magnetic field chosen as 0.35 T).



16.43 MM FROM START

SOLE Y= 0.0 MM

20.52 MM FROM START

FIG. 1 COMPUTED CHARGE DISTRIBUTION NEAR THE RF OUTPUT OF THE QKS 1842 DECFA.

TABLE 3
 COMPUTED POWER BALANCE IN
 THE QKS 1842 AT 24.3 kV

	<u>Input (kW)</u>	<u>Output (kW)</u>
RF Drive	24	
Anode Current x Anode Voltage	403	
RF Output		168
RF Attenuation Loss		10
Anode Interception		239
Sole Interception	<u> </u>	<u> 37 </u>
Totals	427	454
Efficiency = 35.7%		

D. Secondary Emission. The computed secondary emission at the sole is sufficient to maintain a stable beam in all these runs. The average primary impact energy computed over a single cycle around the tube is about 280 eV, corresponding to a secondary-emission coefficient of between 1.86 and 2.36. The model of the secondary-emission process is fully described in a previous SAI report.³ The essential features are:

1. Initial energies of 2 eV of emitted electrons,
2. An emission angle of 60 degrees to the surface,
3. Uniform secondary emission over the interaction wavelength irrespective of the points of primary impact,
4. Use of the local potential to correct the primary impact energy for the finite time step,
5. Smoothing of the charge-density array to reduce the spatial fluctuations of the electric field. (The smoothing is done by replacing the charge density at each point by the average of it and the eight neighboring values.)

This model was chosen largely on the basis of trials made with the objectives of maintaining the number of particles in the beam during the RF interaction and the buildup of anode current. It is not expected to be fully accurate because of the finite time step, the discrete potential array and the limited number of particles available in the model.

An estimate of the bombardment energy in the actual tube is readily made from the experimental data. Let V_{pri} (eV) be the average energy of impacting primaries, $I(A)$ be the

net sole current and $P(W)$ be the backbombardment power. The secondary-emission coefficient α is a tabulated function of V_{pri} . Then V_{pri} is given by

$$V_{pri} = (\alpha - 1)P/I_{sole} \quad (1)$$

The separate impact and emission currents are, respectively, $I_{sole}/(\alpha-1)$ and $\alpha I_{sole}/(\alpha-1)$ in magnitude. For the QKS 1842, the values¹ are $P = 60,300$ W, $I_{sole} = 17.1$ A and $\alpha \leq 1.86$ for $V_{pri} \leq 200$ eV or $\alpha \leq 2.53$ for $V_{pri} \geq 1,400$ eV.

Solving Eq. 1 graphically and using the measured impact power to give bounds for the impact current shows that the QKS 1842 operates in either of two regions as follows:

1. $V_{pri} < 200$ eV,
 $\alpha < 1.86$,
 $|\text{impact current}| > 301$ A,
 $|\text{secondary current}| > 318$ A.
2. $V_{pri} > 1,400$ eV,
 $1.4 < \alpha < 2.53$,
 43 A $> |\text{impact current}| > 11$ A,
 60 A $> |\text{secondary current}| > 28$ A,

A more precise solution would require more detailed data on the variation of the secondary-emission coefficient with impact energy, particularly for energies less than 200 eV.

For comparison, the Brillouin circulating current is approximately 78 A, requiring about 2,340 rods of charge in the present model. To reproduce the conditions of solution 1 above in the model then requires approximately 30 charge

rods to be collected on the sole in each of the 298 steps per cycle around the tube.

A similar calculation for the QKS 1705 gives the corresponding regions as follows:

1. $V_{\text{pri}} < 200 \text{ eV}$,
 $\alpha < 1.52$,
 $|\text{impact current}| > 65 \text{ A}$,
 $|\text{secondary current}| > 99 \text{ A}$.
2. $V_{\text{pri}} > 1,400 \text{ eV}$,
 $\alpha < 2.07$,
 $40 \text{ A} > |\text{impact current}| > 32 \text{ A}$,
 $83 \text{ A} > |\text{secondary current}| > 66 \text{ A}$.

In this tube, the values are $P = 56,100 \text{ W}$ and $I_{\text{sole}} = 34 \text{ A}$.

An average impact energy of less than 200 eV (solution 1) is more compatible with the ballistic RF theory² (see Section IX) which predicts a maximum impact energy of approximately 722 eV with 168 kW of RF power for the optimally phased electrons. The peak RF voltage is 1,587 V. The lower impact energy is also closer to the computed value. The higher value would require some form of space-charge instability to produce the required impact energies. For the lower impact energy, a low crossover impact energy, where $\delta = 1$, is important for selecting the cathode material for maximum emission and particularly for rapid starting.

E. Hartree Voltage. The ratios of the anode voltage to the Hartree voltage for the QKS 1842 tube are near unity, as shown in Table 4. The magnetic-field values supplied for

TABLE 4

ANODE AND HARTREE VOLTAGES IN THE QKS 1842 AT 9.75 GHz

Anode Voltage (kV)	Actual Tube (cylindrical geometry)		Computation (linear geometry)	
	Magnetic Field (T)	Anode Voltage (Hartree Voltage)	Magnetic Field (T)	Anode Voltage (Hartree Voltage)
25.5	0.4115	1.038	0.37	1.038
24.3	0.4114	0.990	0.35	1.057
22.2	0.3788	0.998	0.322	1.068

the actual tube may be too high since the anode voltages of 24.3 kV and 22.2 kV are below the Hartree values. However, these runs refute an earlier hypothesis¹ by showing efficiency above 32 percent despite the closeness of the anode and Hartree voltages. Apparently, this is not a significant factor in the steady-state CFA performance.

F. RF Synchronism. The phase of the RF current relative to the RF voltage indicates a lag at the RF output which changes to a lead as the RF power falls along the backward-wave circuit. Eventually, as shown in Fig. 2, the current and voltage become more than 90 degrees out of phase and the electrons may slip entirely out of synchronism. Most runs show this pattern. The departure from synchronism reduces the available output power for a given amplitude of RF current and, hence, limits the attainable efficiency. The computed gain (Fig. 3) oscillates with distance as the current moves out of phase. In some cases, the current and voltage pass back into phase before the sever region is reached and the RF power falls to a few kilowatts.

The power transferred per unit length from the beam to the circuit is reduced by the factor $\cos \theta$ when the current leads or lags the voltage by the phase angle θ . Two possible explanations are suggested for the impedance correction factor that is needed:

1. The actual phase angle θ is less than that computed if loss of synchronism is caused by the finite time step or limited number of rods in the calculation. The results

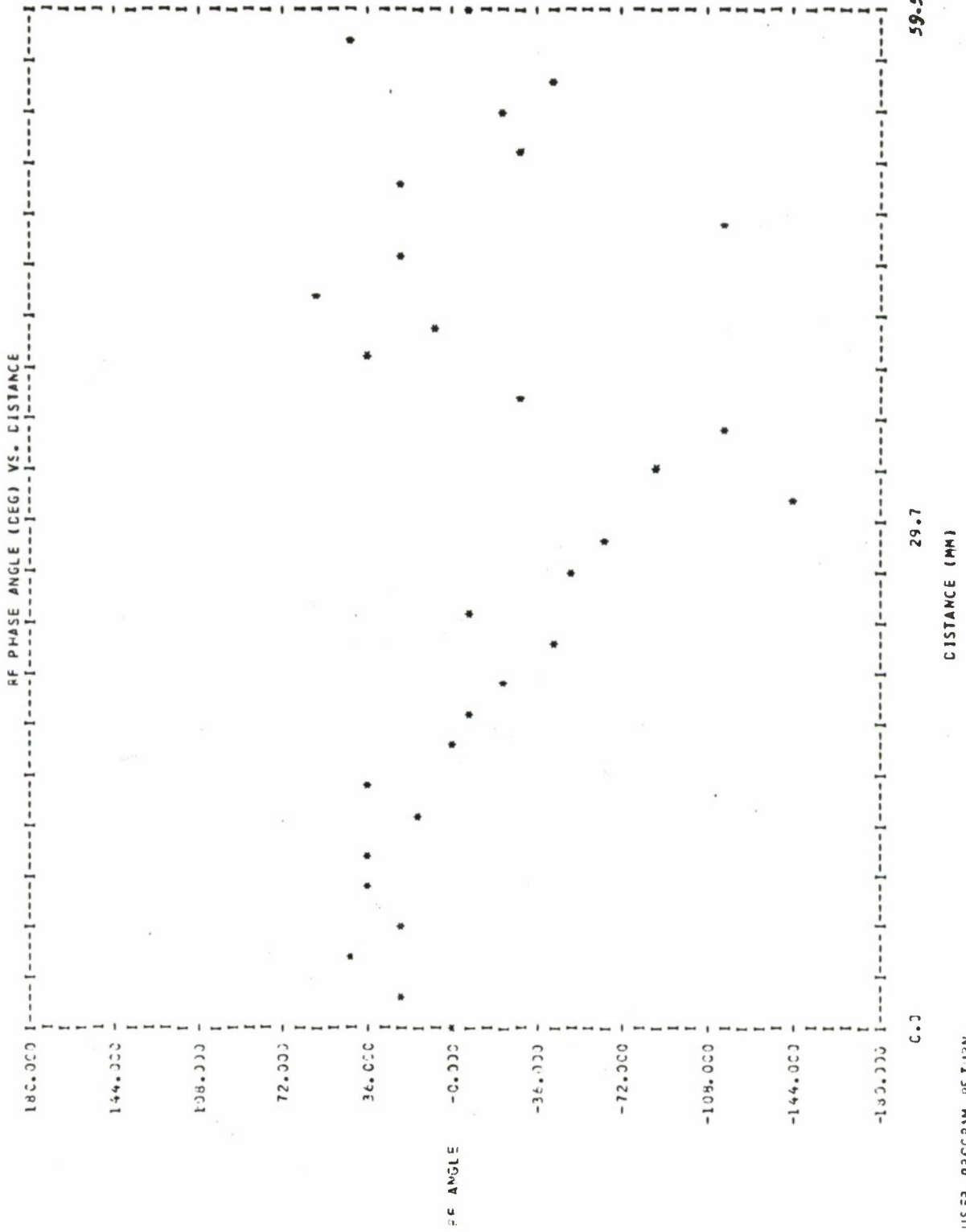


FIG. 2 COMPUTED PHASE LAG OF RF CIRCUIT CURRENT FROM RF CIRCUIT VOLTAGE AROUND BACKWARD-WAVE DECFA.

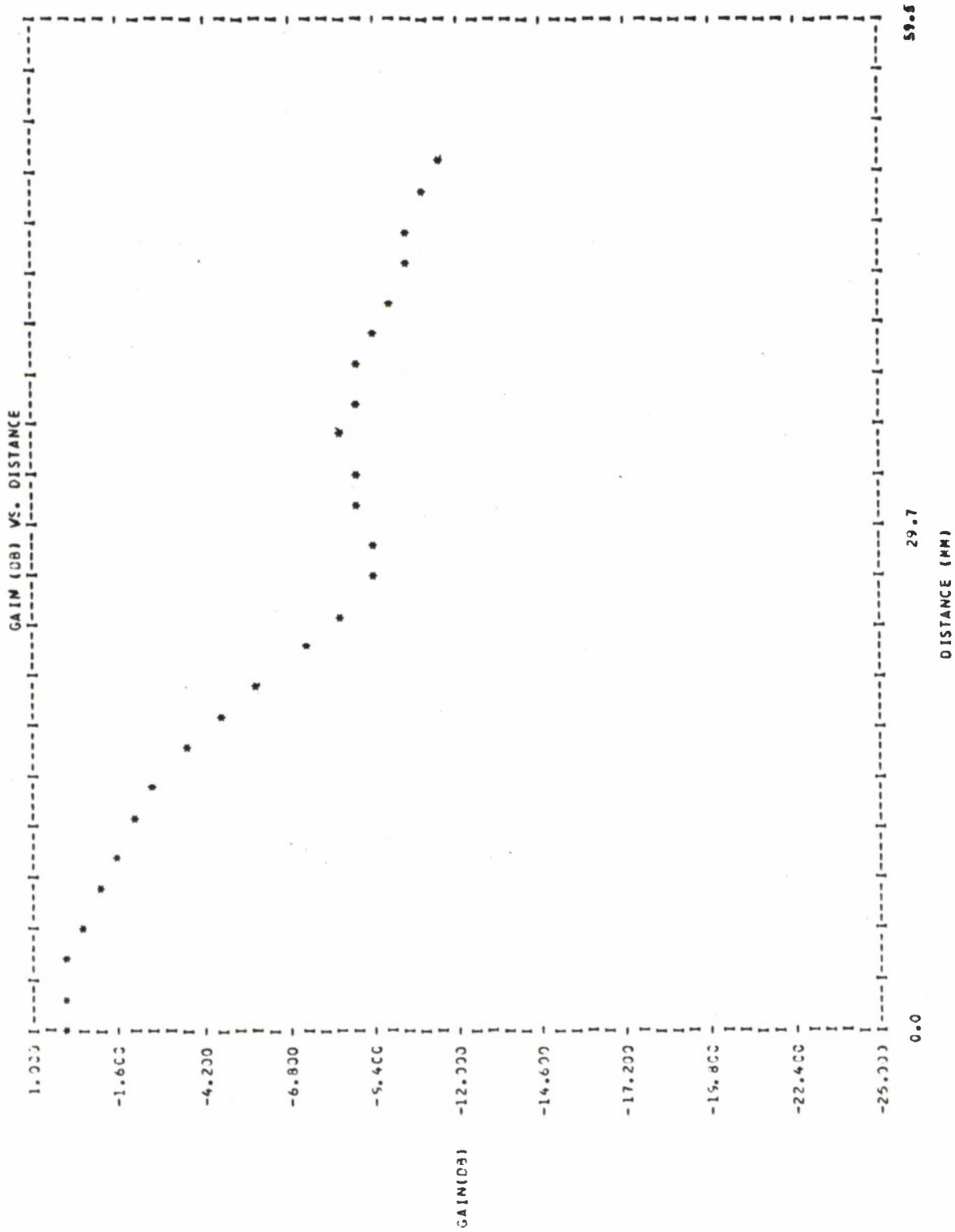


FIG. 3 COMPUTED GAIN VS. DISTANCE AROUND THE BACKWARD-WAVE DECFA.

shown in Section VII support this conclusion. An attempt to improve the synchronism by using adiabatic motion equations (with the acceleration terms neglected) does not appear promising, partly because of the difficulty in modeling the secondary-emission process.

2. The beam actually experiences the total RF field from all space harmonics. A more accurate model should therefore use the vane circuit to provide an anode boundary condition for the RF voltage. SAI has developed this model, and in Appendix E the fields are compared with those of a single space harmonic. The latter is in fact an excellent approximation.

G. Time-Dependent Effects. Successive cycles around the tube do not converge to a single state; instead the computed gain is sensitive to the charge distribution fed through from the previous cycle. A time-smoothing secondary-emission procedure has been tested but it did not affect the differences in the cycles. There is, however, no physical reason for the actual tube to reach a steady state. Indeed, the transit time of the RF current peak around the tube is not, in general, a multiple of the RF period. Moreover, computations show that the sever region does not, in general, remove all beam modulation so that the time to establish a bunch synchronous with the RF wave varies in successive cycles. On this hypothesis, the tube should produce fluctuations of output power, phase and anode current over a few transit times. The transit time around the QKS 1842 with

the cold phase velocity is approximately 14.5 RF periods or 1.5×10^{-9} seconds at 9.75 GHz. Typical pulse lengths range from 1.7 microseconds to 3.4 microseconds, covering from 1,100 to 2,300 cycles around the tube.

All the present simulations assume that the anode voltage seen by the electrons remains constant. This may be realistic if the response time of the modulator to variations in collected electron current exceeds a transit time (as is usually the case). However, it would be interesting to obtain measurements of any observable fluctuations in the power, current and voltage during the steady-state portion of the pulse.

III. Variation of Frequency in the QKS 1705 CFA

Under usual operating conditions, the RF drive power, the magnetic field and the adjustment of the pulse modulator are left unaltered while the drive frequency is varied. Within the operating band, the anode voltage and current readjust automatically to new values, the voltage rising and the current falling as the frequency is increased. Typical measured results, shown in Table 5, show a clear trend of decreasing RF output power as the frequency is raised. In this tube, the lower end of the frequency band is limited by a competing mode which restricts the anode current and output power available.

The causes of these bandwidth limitations are not understood in detail and neither is the exact mechanism by which

TABLE 5
 MEASURED CURRENT, VOLTAGE AND RF POWER
 FOR THE QKS 1705 OVER THE OPERATING FREQUENCY BAND

	<u>Low Frequency</u>	<u>Midband Frequency</u>	<u>High Frequency</u>
Frequency, GHz	9.5	9.75	10.0
Magnetic Field, T	0.36	0.36	0.36
Anode-Sole Voltage, kV	32.1	33.0	34.0
Anode Current, A	34.0	34.0	34.0
RF Drive Power, kW	30.0	30.0	30.0
RF Output Power, kW	546.0	513.0	504.0
Gain, dB	12.6	12.35	12.3
Efficiency, %	45.6	41.1	39.3

the voltage readjusts to synchronize the beam to the new phase velocity corresponding to a new frequency.

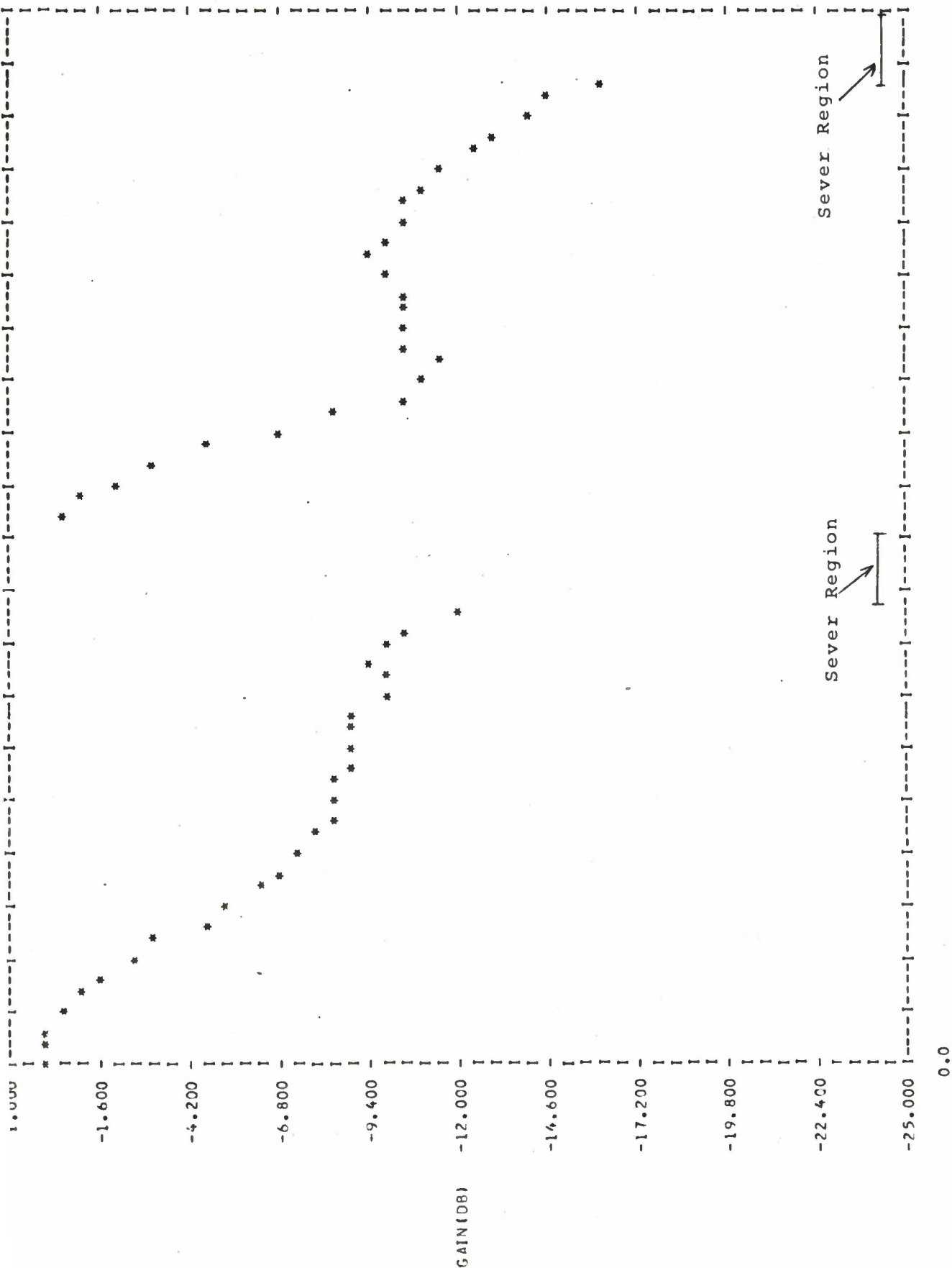
The complexity of the CFA makes it very difficult to obtain a quantitative theoretical prediction of bandwidth and efficiency as a function of frequency. This is certainly beyond the capability of the present simulation program; however, the results provide some insight into the various mechanisms affecting performance.

Computed results for the QKS 1705 at 9.5, 9.75 and 10.0 GHz were presented in the January 1977 progress report.¹ The numerical results are summarized here as Table 6. There is good qualitative agreement with observations with the pattern of beam bunching and RF interaction maintained as the frequency and anode voltage are changed at a constant value of magnetic field (optimized as 0.35 T for the linear geometry of the model). Gain and phase plots for all three frequencies closely resemble Figs. 4 and 5 for 9.75 GHz. Thus, they verify that the changes in anode-sole voltage with frequency maintain synchronism.

The power balance, averaged over three or four cycles, is shown for the three frequencies in Table 7. The measured values are shown for comparison in Table 8. These runs were made with ten time steps per cyclotron period and with twice the given RF impedance values. The computed anode and sole currents, which exceed the measured values by at least 25 percent, are uncorrected for beam width and give correspondingly high heating values, particularly at 10 GHz. Using

TABLE 6
RESULTS FOR THE QKS 1705 CFA COMPUTED WITH 0.35 T MAGNETIC FIELD

Input Data			Computed			Measured With 0.36 T Magnetic Field				
Frequency (GHz)	Anode-Sole Voltage	Impedance (Ω)	RF Output Power (W)	Anode Current (A)	RF Drive Power (W)	RF Gain (dB)	Efficiency (%)	Anode Current (A)	RF Drive Power (W)	Efficiency (%)
9.5	32,100	7.4	546,000	37.43	177,207	4.9	30.7	34.0	30,000	45.6
9.5	32,100	14.8	546,000	47.76	38,550	11.5	33.1	--	--	--
9.75	33,000	8.8	513,000	42.85	80,155	8.1	30.6	34.0	30,000	41.1
9.75	33,000	17.4	513,000	43.43	29,876	12.3	33.7	--	--	--
10.0	34,000	10.4	504,000	43.65	73,265	8.4	29.0	34.0	30,000	39.3
10.0	34,000	20.8	504,000	51.87	5,514	19.6	28.3	--	--	--



DISTANCE (MM)

FIG. 4 RF GAIN COMPUTED OVER TWO CYCLES AROUND BACKWARD-WAVE DECFA.

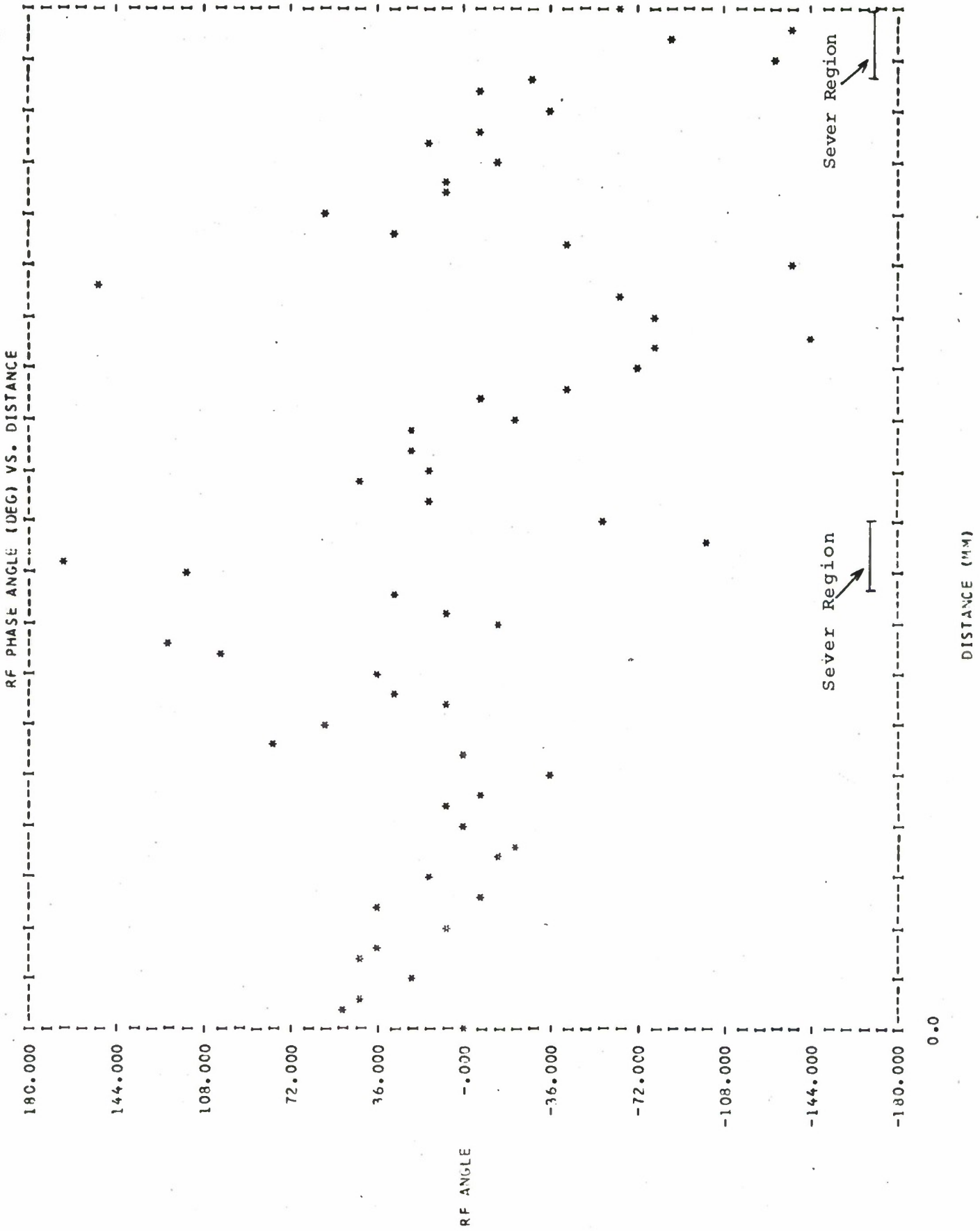


FIG. 5 COMPUTED PHASE LAG OF RF CIRCUIT CURRENT FROM RF CIRCUIT VOLTAGE FOR TWO CYCLES AROUND BACKWARD-WAVE DECFA.

TABLE 7

COMPUTED POWER BALANCE IN QKS 1705 AT OPERATING FREQUENCY BAND

	9.5 GHz, 32.1 kV, 48 A	9.75 GHz, 33 kV, 43 A	10.0 GHz, 34 kV, 52 A
	Input (kW)	Input (kW)	Input (kW)
RF Drive	39	30	5
Dc Input	1,519	1,433	1,764
RF Output	546	513	504
RF Attenuation	26	22	14
Anode Interception	856	845	1,103
Sole Interception	145	164	154
Total	1,558	1,463	1,769
Efficiency	32.9%	34.0%	28.2%

TABLE 8
MEASURED POWER BALANCE IN THE QKS 1705

	9.5 GHz, 32.1 kV, 34 A	9.75 GHz, 33 kV, 34 A	10.0 GHz, 34 kV, 34 A
	Input (kW)	Input (kW)	Input (kW)
RF Drive	30	30	30
Dc Input	1,091	1,122	1,156
RF Output	546	513	504
RF Attenuation and Anode Interception*	488	552	594
Sole Interception*	54	56	58
Total	1,121	1,152	1,186
Efficiency	47.3%	43.0%	41.0%

*Interception and attenuation values are approximate.

the 9.75 GHz computed figures as an example, 59 percent of the direct input power is dissipated as anode heating and 11 percent on the sole, compared with measured values of 47 and 5 percent, respectively.

The computed results show that the correction factors for anode current and RF impedance are frequency-dependent. Interfering modes, which restrict the bandwidth, are not treated in the model. Further, the measured direct current and voltage and the RF output power are averages over the pulse length, or many transits around the tube, rather than values from only a few cycles. These factors contribute to the quantitative discrepancies of the results with measured values. However, by examining the parameters that vary with frequency for the interacting mode, four quantities can be distinguished and the measured fall of output power with frequency can be related qualitatively to a combination of mechanisms.

These significant quantities are as follows:

1. v_p/c , (RF phase velocity)/(speed of light),
2. βa , (2π x anode-sole spacing)/(retarded RF wavelength),
3. $\beta l/2\pi$, (interaction length)/(retarded RF wavelength),
the electrical length of the tube,
4. the RF impedance.

Table 9 shows the values of the above parameters. The lower values of βa at higher frequencies increase the RF fields away from the circuit for a given RF voltage; however, the tube is electrically shorter.

TABLE 9
PARAMETER VARIATIONS WITH FREQUENCY
IN THE QKS 1705

<u>Frequency</u> (GHz)	<u>v_p/c</u>	<u>βa</u>	<u>$\beta \ell / 2\pi$</u>	<u>RF Impedance</u> (Ω)
9.5	0.1524	2.82	13.61	7.4
9.75	0.162	2.72	13.14	8.8
10.0	0.1728	2.62	12.64	10.4

A larger RF impedance gives greater coupling between the beam and the circuit, but also a lower RF power for a given RF voltage, as can be seen in Table 2 of Reference 1. There is probably no single mechanism affecting the interacting mode as the frequency varies; indeed, irregularities in the charts of measured performance indicate this.

IV. Results for the Varian SFD-243 Forward-Wave CFA

This tube⁴ runs at a lower frequency (3.3 GHz) and at a higher relative RF-to-dc voltage level than either the QKS 1705 or QKS 1842. It is relatively easier to simulate with the present model since the direction of beam motion and RF power gain are the same, allowing the RF drive power to be supplied to the program. Full data were presented in an earlier report,³ and the operating conditions are compared with those for the Raytheon tubes in Table 10. The results described in the earlier report³ demonstrated the sensitivity of the anode current and output power to the magnetic field. SAI has made a further run, covering five cycles at 0.225 T, to determine the differences computed between successive cycles around this forward-wave tube. The computed anode current and output power fluctuate (see Table 11), again suggesting a real effect. Varian Associates has computed similar fluctuations in the SFD-261 tube.⁵ No impedance or beam-width corrections are necessary.

SAI has at present a single measured data point (125 kW output at 21 A anode current), and the agreement with the computed results shown in Table 11 is excellent. Additional

TABLE 10

COMPARISON OF THE SFD-243, QKS 1705 and QKS 1842 OPERATING DATA

	Forward-Wave SFD-243	Backward-Wave QKS 1705	Backward-Wave QKS 1842
Midband Frequency, GHz	3.3	9.75	9.75
Anode-Sole Voltage, kV	13	33	24.3
Magnetic Field, T	0.241	0.36	0.411
RF Impedance, Ω	45.0	8.8	7.5
RF Drive Power, kW	8	30	5
RF Output Power, kW	≈ 125	513	175
Anode Current, A	≈ 21.0	34.0	17.1
Efficiency, %	≈ 43.0	41.1	39.1
(Input RF Voltage/Direct Voltage)	0.065	0.022	0.012
(Output RF Voltage/Direct Voltage)	≈ 0.258	0.091	0.065
Maximum Secondary-Emission Coefficient	5.0	2.15	2.63
Primary Impact Energy, eV, for Maximum Secondary Emission	300-500	800-1,000	800-1,000

TABLE 11

COMPUTED RESULTS FOR THE SFD-243 CFA WITH 0.225 T
MAGNETIC FIELD (FORWARD-WAVE INTERACTION)

<u>Cycle Number</u>	<u>Anode Current (A)</u>	<u>Sole Current (A)</u>	<u>RF Output Power (kW)</u>	<u>RF Gain (dB)</u>	<u>Efficiency (%)</u>
1 (starting)	9.06	12.12	5.8933	8.67	43.2
2	25.11	23.40	147.853	12.67	42.8
3	28.42	29.73	179.866	13.52	46.5
4	19.15	18.75	124.480	11.92	46.8
5	26.77	26.63	160.181	13.02	43.7
4-cycle mean	24.86	24.62	153.095	12.82	44.8

data on this or other forward-wave tubes are needed for conclusive results, however. A distinct spoke of charge develops (see Fig. 6), probably because the RF and direct voltages are of comparable magnitude (see Table 10). In the QKS 1705 and QKS 1842 tubes, the ratio of RF to direct voltage is small even at the output. Figures 7 and 8 show the computed gain and RF phase angle; the beam-wave synchronism is closer than in the backward-wave tubes.

V. RF Phase Delay

For maximum efficiency, the RF current induced on the circuit should travel in phase with the interacting space harmonic of the RF voltage. In an actual tube, the current and voltage are not locked in synchronism, as the computed results show (e.g., Figs. 2 and 4). This local phase angle is related to the overall phase difference between the hot and cold RF circuit waves. This phase difference is measurable at the RF output by comparing operating and non-operating tube conditions.

If the current and voltage waves are in phase all along the circuit, the measured hot and cold RF transit times from input to output are equal. They are also approximately equal if the beam and the RF wave are "unlocked" throughout the tube, because the RF driving current is smaller in amplitude than in the synchronous case and its phase relative to the RF voltage changes through 360 degrees several times per cycle around the tube.

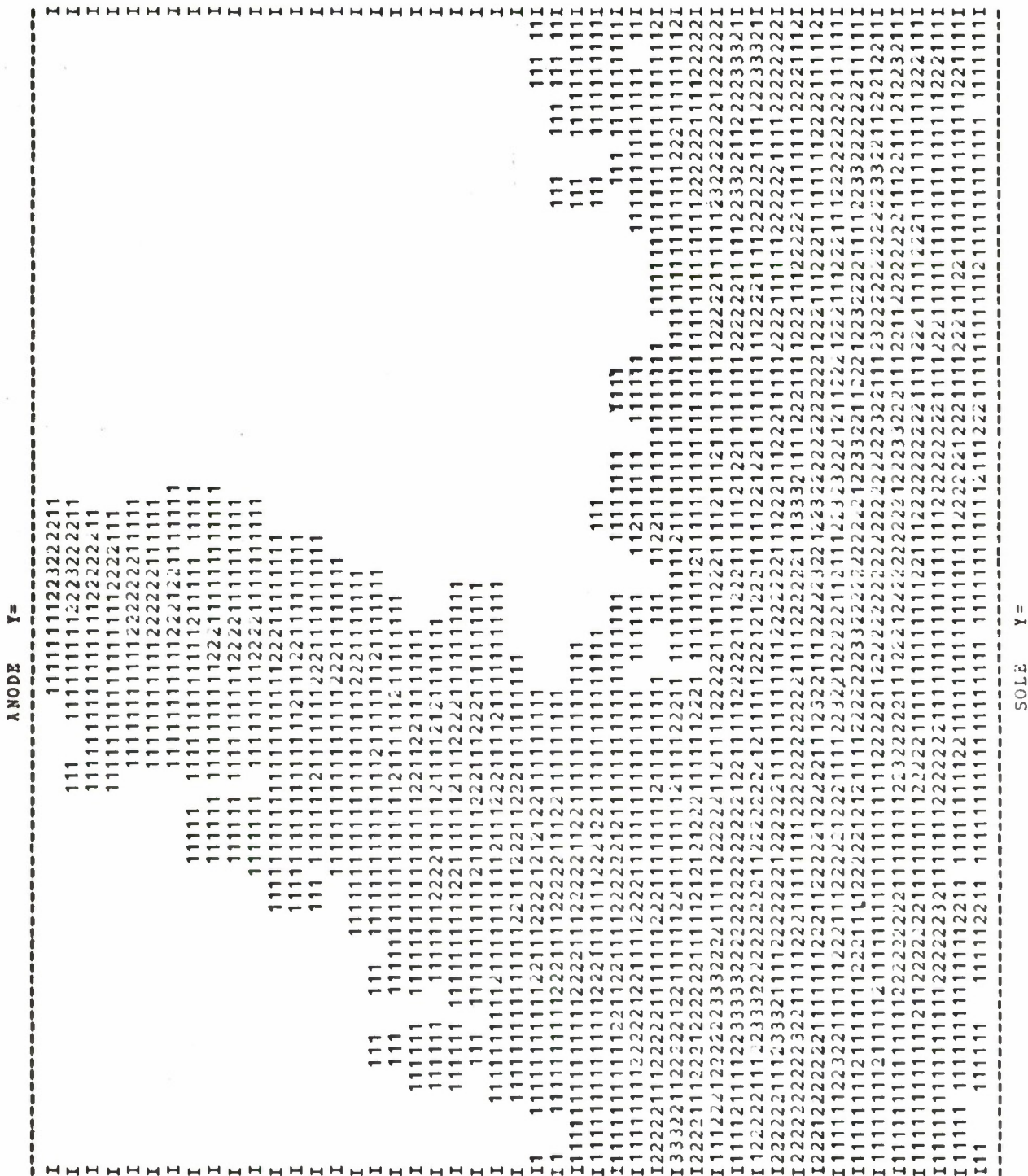


FIG. 6 CHARGE DISTRIBUTION COMPUTED NEAR RF OUTPUT OF FORWARD-WAVE DECFA.

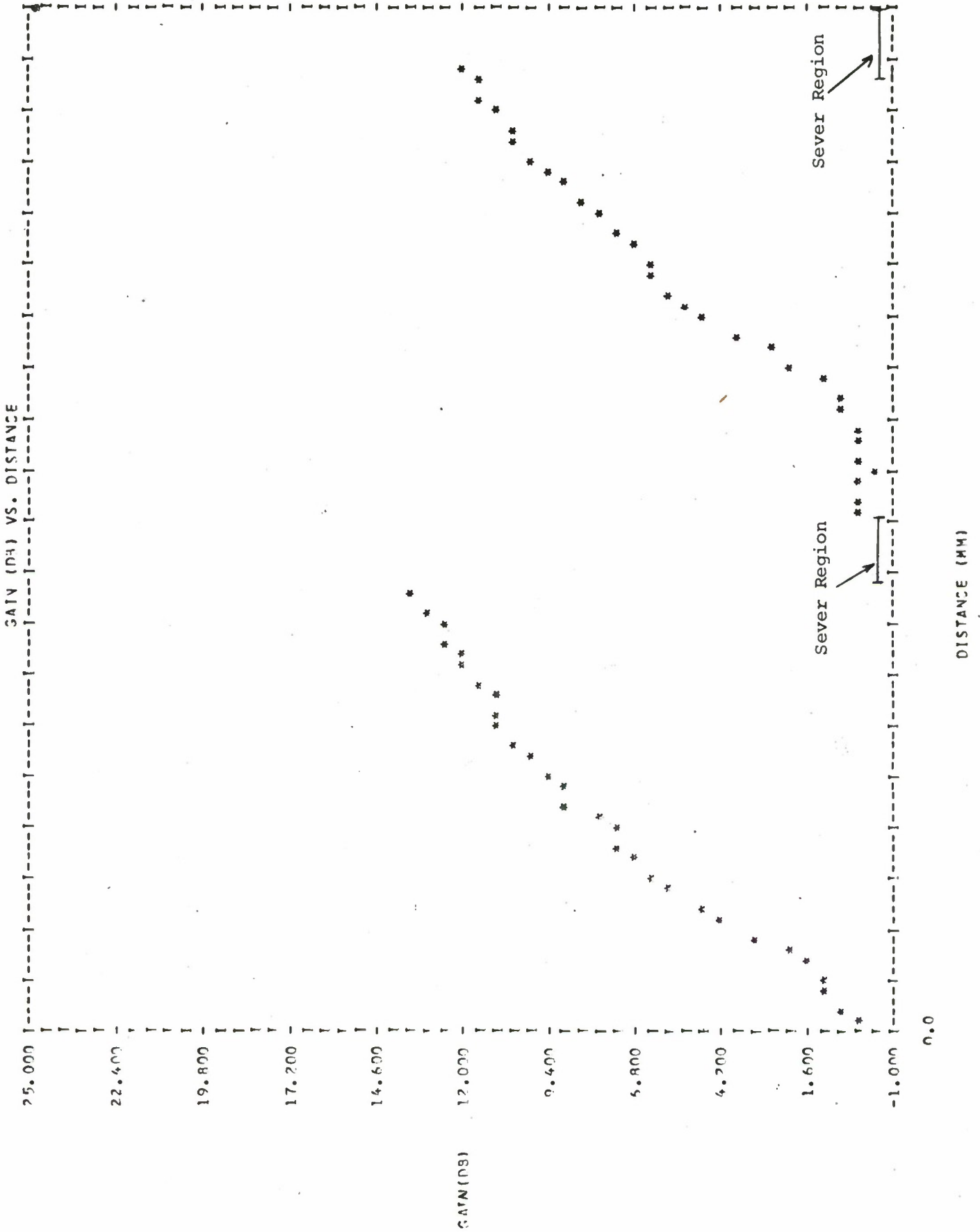


FIG. 7 RF GAIN COMPUTED OVER TWO CYCLES AROUND FORWARD-WAVE DECFA.

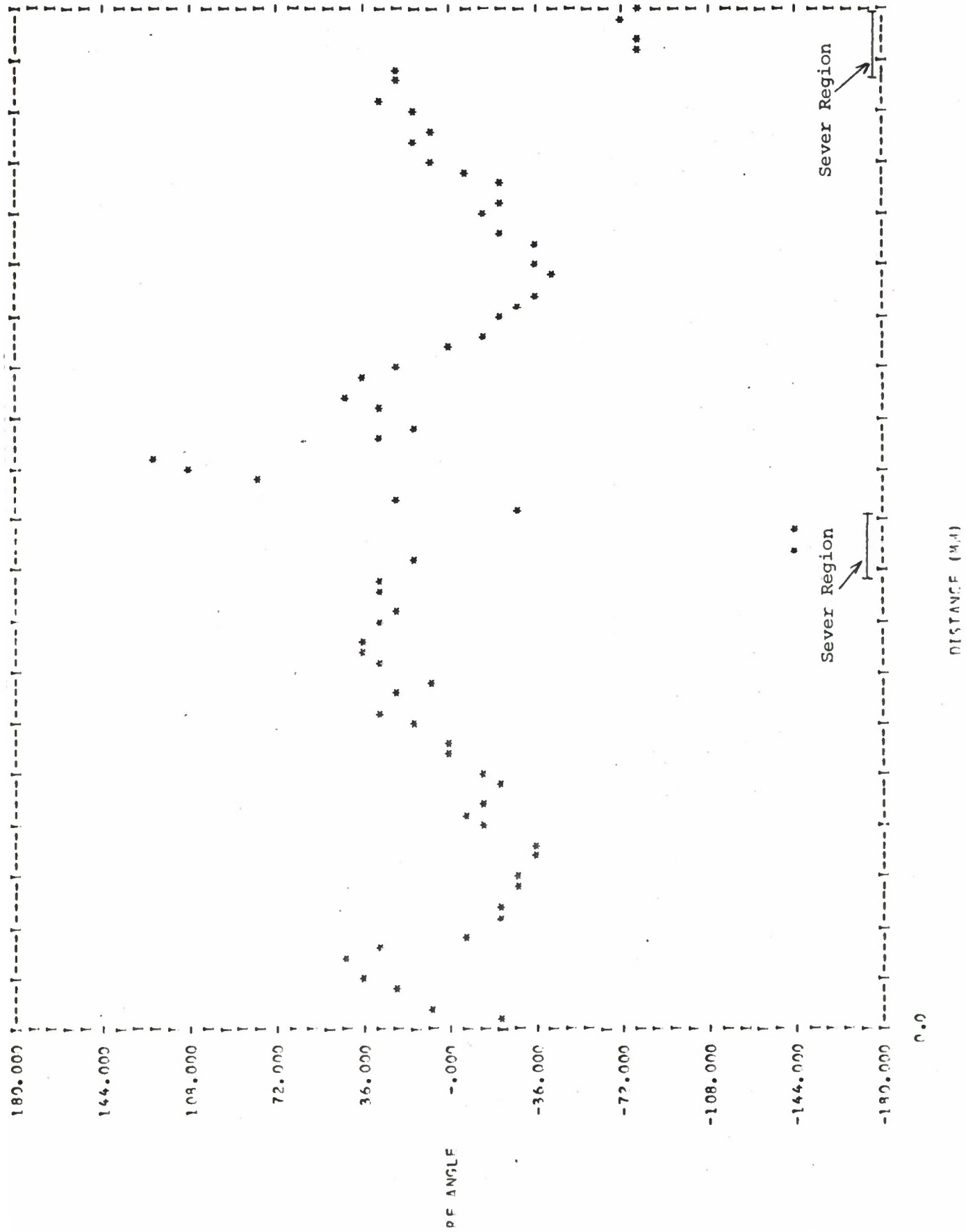


FIG. 8 RF CURRENT PHASE LAG FROM RF VOLTAGE COMPUTED FOR TWO CYCLES AROUND THE DECFA CIRCUIT.

0.0

An increase in the measured RF delay when the tube is turned on results from a net lag of the electron bunch behind the RF wave, under a fixed operating voltage and magnetic field. The full equations for both forward- and backward-wave CFA's are given in Appendix A. It is noted there that the measured phase delay is from input to output although the strapping of the vanes results in a wave seen by the beam which travels in the reverse direction.

A further distinction between forward- and backward-wave CFA's is the sign of the net RF phase delay as seen by the beam. If the electron bunch travels more slowly than the RF wave, the RF wave velocity increases toward the input and increases the phase difference in a backward-wave CFA, whereas in forward-wave interaction, the electron bunch tends to pull the wave along with it and maintain synchronism. This point has been emphasized by Sedin⁶ and it implies that a fine adjustment of the anode-sole voltage is necessary at each drive frequency to maintain maximum gain over the operating band. In practice, this voltage change occurs automatically as the drive frequency is changed within the operating band.

In present simulations, the plots of the phase lag of current relative to voltage vs. distance around the tube provide useful information on the beam behavior. They show whether the beam and wave are near synchronism and aid the optimization of the magnetic field supplied to the program with a given voltage. The computed RF phase delays vary by

approximately six percent of the cold value in successive cycles around the tube and it is hypothesized that similar phase variations occur in practice over a few transit times.

VI. The Off-Center Cathode

In a basic CFA design, the anode and cathode are circular and concentric. However, it is straightforward in practice to shift the cathode away from its geometrical center position and, hence, vary the electric field around the CFA. Experimental results obtained at Varian Associates on a forward-wave CFA⁵ show, for example, that different optimum cathode positions exist for highest efficiency, minimum current, highest power output or best signal-to-noise ratio.

The SAI simulation program allows piecewise linear tapering of the anode or the sole, recomputing the direct and RF fields at each time step and removing the charge rods that are intercepted where the interaction region narrows. It is assumed that the relative change in anode-sole spacing is small over one retarded wavelength around the tube.

For the QKS 1842, the 24.3 kV simulation has been repeated with the circular cathode moved by ten percent of the mean anode-cathode spacing of 1.96 mm. Offsets were made both directly away from the RF output and, in a separate run, toward the output. The program actually treats four linear taper sections of the tube as a good approximation, replacing the cylindrical configuration of the actual

tube with a linear configuration as in all previous calculations. It is expected that similar results would be obtained from a cathode shift directly away from or toward the RF input position since the sever separates the RF output and input by only 50 degrees around the tube. However, additional runs are needed to verify this.

The numerical results, averaged over three cycles around the tube (excluding starting cycles), are given in Table 12 together with the results for a uniform anode-sole spacing. Although these runs do not reproduce the exact operating conditions of the actual tube (for example, with fixed RF drive and varying RF output power), the results show definite trends. The off-center cathode produces an anode current over twice the normal value, and the additional interacting charge yields a greater rate of fall of the RF power level toward the input and a lower value of RF drive power. Existing operational data suggest that interfering modes may prevent operation at this current level, however.

Since these increased currents are calculated for the same RF output power of 168 kW, the calculated efficiency is reduced. Measurements on the Raytheon tubes also show this result.* The magnetic field is uniform (0.35 T in the model) so that the ratio of direct electric to magnetic fields (E/B) increases where the anode and cathode approach and falls where they separate. From the results, it appears

*Private communication from Dr. Walter J. Griffin, Raytheon Company Microwave and Power Tube Division, to Dr. Donald M. MacGregor, Shared Applications, Inc., March 9, 1977.

TABLE 12

COMPUTED RESULTS FOR THE QKS 1842 WITH VARIED CATHODE POSITION

Cathode Position	Input Data			Computed Data				
	Anode-Sole Voltage (kV)	Impedance (Ω)	RF Output Power (kW)	Anode Current (A)	RF Drive Power (kW)	Sole Heating (kW)	RF Gain (dB)	Efficiency (%)
Cathode geometrically centered 1.96 mm spacing from anode	24.3	15.0	168	15.87	19.030	33	9.46	38.63
Cathode displaced 0.196 mm away from RF output	24.3	15.0	168	32.01	8.205	81	13.11	20.54
Cathode displaced 0.196 mm toward RF output	24.3	15.0	168	24.51	4.383	20	15.84	27.5

that the effect of the greater electric field dominates the effect of the reduced electric field opposite, causing the anode current and anode heating to increase for both directions of shift of the cathode. The computed sole bombardment power is increased from 33 kW to 81 kW when the cathode is moved away from the output but reduced to 20 kW when the cathode is moved in the opposite direction. However, in both cases, the backbombardment is sufficient to maintain the beam by secondary emission. For the present magnetic field, near optimum when the cathode and anode are concentric, the computer predicts that a higher efficiency and a greater gain result from moving the cathode toward rather than away from the RF output.

The spatially varying electric field changes the phase angle between the beam RF current and the RF wave. If the cathode is moved toward the RF output, the beam moves faster at the output and gains in phase while the lower electric field opposite the output slows the beam. These computed results vary from cycle to cycle and computed effects such as breakup of the beam bunch and the resulting fluctuating gain with distance make a simple interpretation of the mechanisms difficult. Plots of the RF current phase lag (Fig. 9) from the third cycle of the three runs show that in these cases a phase lead (a negative phase angle on the plots) develops as the RF circuit power falls away from the output in the direction of the beam motion. Shifting the cathode away from the RF output increases this phase lead; shifting

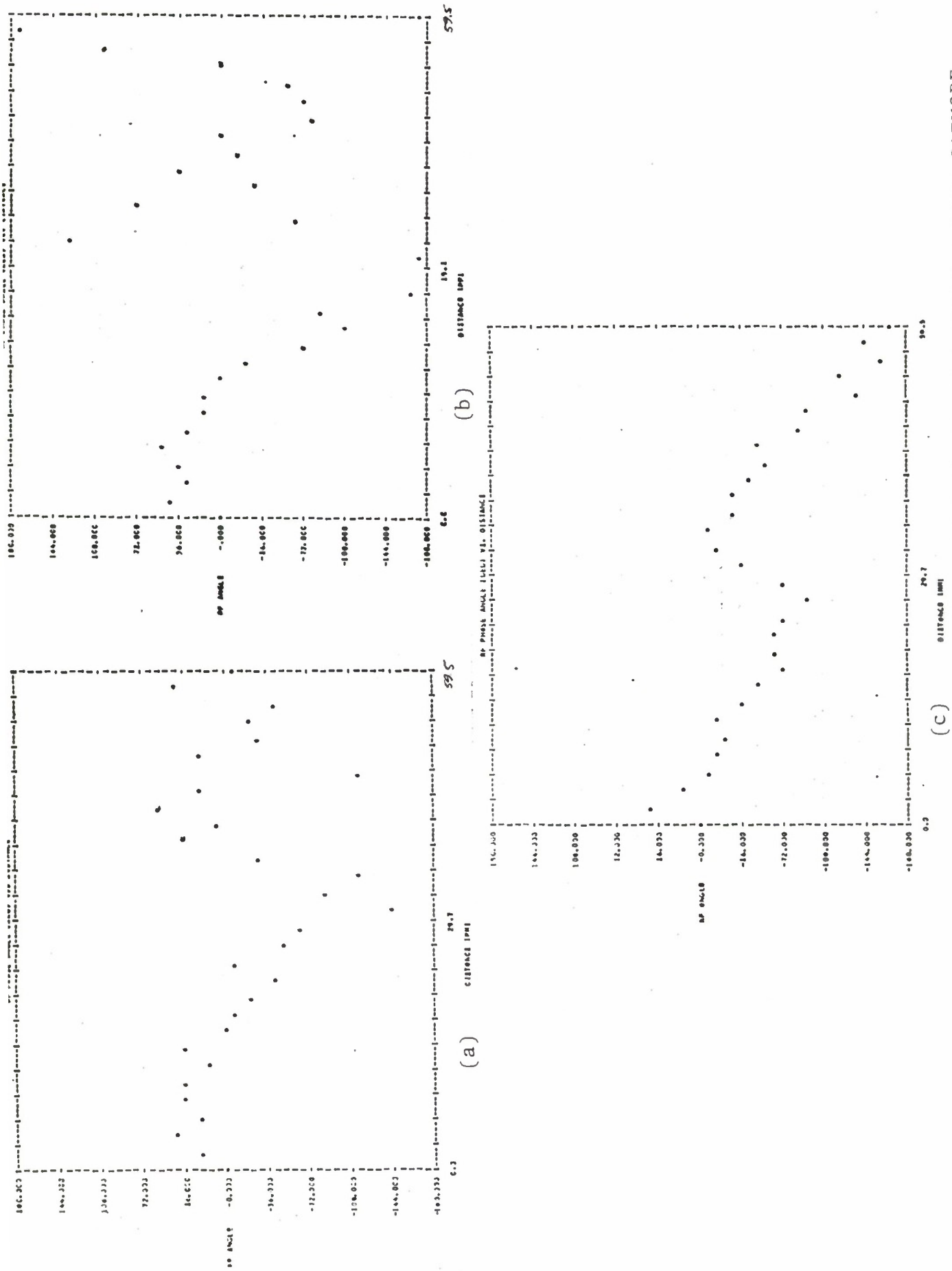


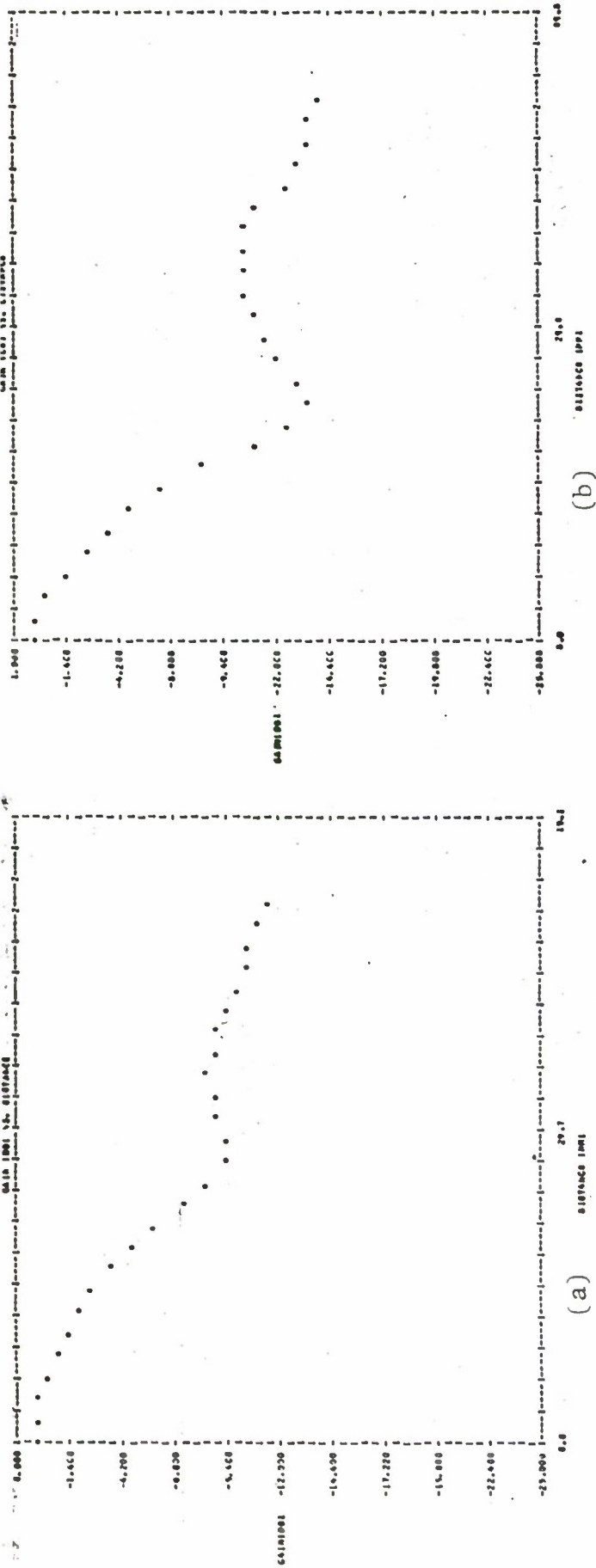
FIG. 9 COMPUTED RF CURRENT PHASE LAG IN BACKWARD-WAVE CFA FOR CYCLE 3 WITH CATHODE (a) CENTERED, (b) SHIFTED AWAY FROM, (c) SHIFTED TOWARD RF OUTPUT.

the cathode toward the output reduces the phase lead and improves the overall synchronism between beam and RF wave. The corresponding RF gains for the three cathode positions are plotted in Fig. 10, which shows clearly that the greatest gain is obtained when the cathode is moved toward the output.

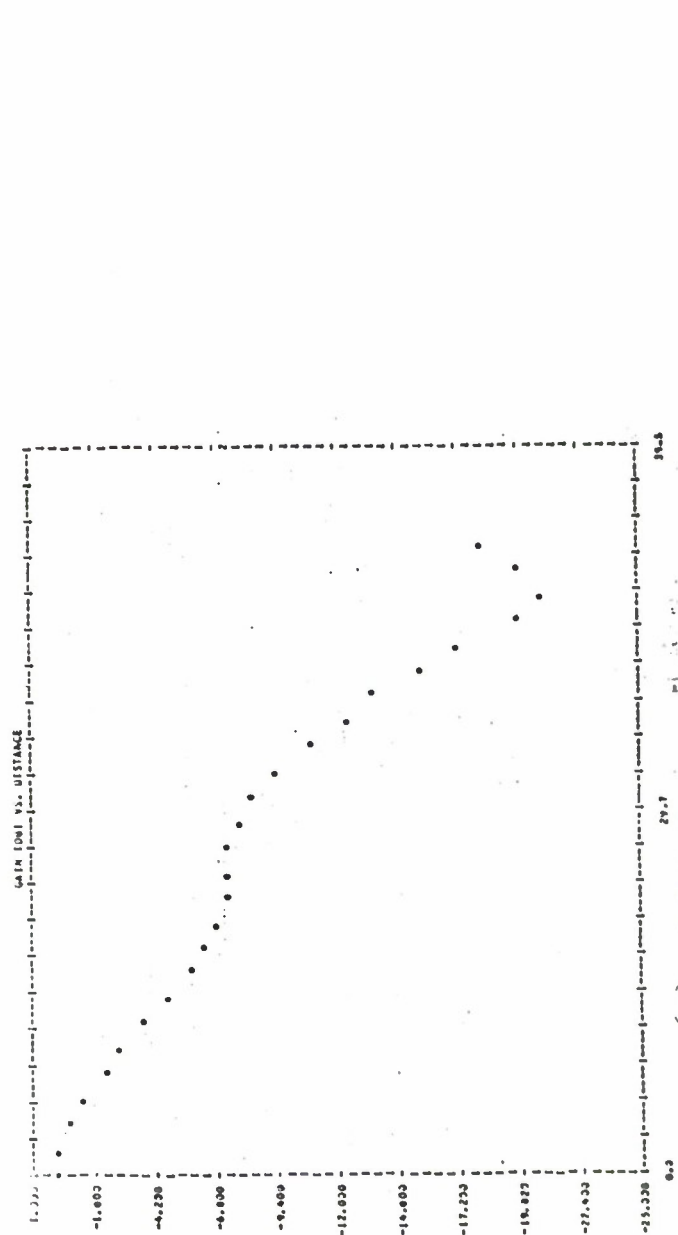
In summary, it is deduced from the present results that an off-center cathode gives increased anode current and greater RF gain but lower efficiency. A shift toward rather than away from the RF output gives the higher efficiency and the lower sole backbombardment power.

VII. Modified Circuit Equations

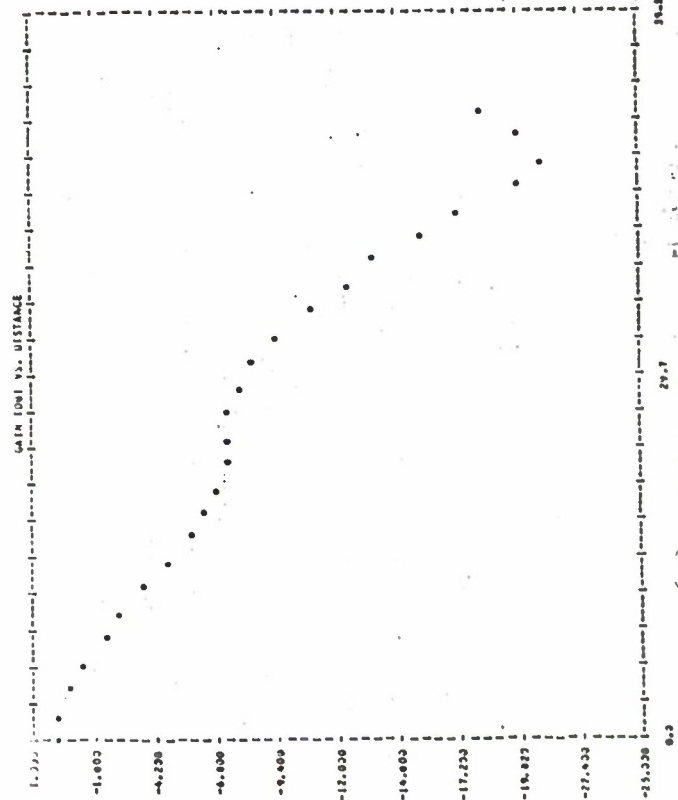
All the present calculations used an equivalent transmission line to model the anode vane circuit with a single interacting space harmonic and corresponding values of phase velocity, interaction impedance and attenuation. Two types of transmission-line equations have been tested: the equations of Rowe⁷ in linearized first-order form and the power-transfer equations of Yu et al.⁸ (with modifications and corrections). The modified equations of Yu et al.⁸ are given in Appendix A of this report, and the Rowe⁷ equations are in Appendix B (Ref. 3: Appendix E, with corrections). In order to obtain sufficient RF interaction to derive a drive power near the measured value, the runs for both the QKS 1705 and QKS 1842 tubes have used interaction impedances of twice the measured values. Two possible reasons for this correction factor were suggested in Section II of this report.



(a)



(b)



(c)

FIG. 10 COMPUTED RF GAIN IN BACKWARD-WAVE CFA FOR CYCLE 3 WITH CATHODE (a) CENTERED, (b) SHIFTED AWAY FROM, (c) SHIFTED TOWARD RF OUTPUT.

The runs described here were intended in part to determine whether the circuit equations have some influence on the results. However, no important qualitative differences resulted from inclusion of the modified circuit equations, and both circuit models apparently require a corrected impedance.

Computed results for the QKS 1842 with twenty time steps per cyclotron period are shown in Table 13. The numerical differences in current and RF drive power are of the same order as those due to variations between successive cycles or to changes in the number of rods or the time steps.

Although no theoretical justification has been found for preferring either set of equations, the equations of Yu et al.⁸ have the advantage of requiring a single definition of interaction impedance both for relating the RF voltage and power and for computing the driving effect of the beam. The power-transfer model also is easier to visualize physically. Consequently, the Yu et al.⁸ equations have been adopted and are used, for example, in the study of the off-center cathode (Section VI).

VIII. Program Tests with a Reduced Time Step and Increased Number of Rods and Modified Motion Equations

The QKS 1842 simulation with an anode voltage of 24.3 kV and a magnetic field of 0.35 T (Table 1) has been used for comparison tests as follows:

1. With ten time steps per cyclotron period and a maximum of 4,000 rods allowed,

TABLE 13
COMPARISON OF RESULTS FOR TWO RF-CIRCUIT MODELS

	<u>Cycle</u>	<u>Anode Current (A)</u>	<u>Sole Current (A)</u>	<u>RF Drive Power (kW)</u>	<u>RF Output* Power (kW)</u>
Transmission-Line Equations	1 (starting)	10.81	6.80	70.952	168
	2	11.14	15.16	32.920	168
	3	18.19	22.18	23.665	168
	4	18.43	23.66	14.054	168
Power-Transfer Equations	1 (starting)	7.822	3.62	104.453	168
	2	12.36	17.94	41.460	168
	3	15.07	20.58	11.562	168
	4	20.19	23.10	4.068	168

*Supplied to program

2. With twenty steps per cyclotron period and up to 4,000 rods allowed (up to 2,721 rods actually used),

3. With twenty steps per cyclotron period, up to 10,000 rods allowed and the charge per rod reduced by a factor of 0.4 (up to 6,787 rods actually used),

4. With amended equations of particle motion,

5. With both the amended equations of motion and an area weighting procedure for computation of the charge density at the computation mesh points and for interpolation of the electric field to rod positions.

Tests 1 through 3 cover four cycles, including the starting cycle around the tube; shorter runs suffice for tests 4 and 5. An RF drive of 168 kW is supplied at the output and the interaction impedance is taken as 15 Ω .

The computed anode and sole currents and RF drive power, shown in Table 14, show that twenty rather than ten steps per cyclotron period are justified despite the extra cost. Increasing the number of rods does not eliminate or even reduce the fluctuations between successive cycles around the tube. The printouts of bunch shape and of the phase angle of the RF current show a similar pattern of interaction in all three runs, but with the additional rods the current and voltage retain phase locking without the scatter of phase angle shown in Fig. 2. As a result, the RF interaction continues and produces a lower computed final power level. Figure 11 shows the RF-current phase lag around cycle 3 of the 6,787-rod run.

TABLE 14
 COMPARISONS OF TIME STEP AND ROD SIZE
 IN THE QKS 1842 SIMULATION AT 24.3 kV

a. With 10 steps per cyclotron period and 4,000 rods maximum (average gain = 5.23 dB; average efficiency = 35.0%)

<u>Cycle</u>	<u>Anode Current (A)</u>	<u>Sole Current (A)</u>	<u>RF Drive Power (kW)</u>
1 (starting)	8.55	14.24	98.740
2	13.0	24.21	44.370
3	14.89	9.49	51.840
4	13.64	26.61	55.114
Average over cycles 2-4	13.84	20.10	50.441

b. With 20 steps per cyclotron period and 4,000 rods maximum (average gain = 8.53 dB; average efficiency = 35.8%)

1 (starting	10.81	6.80	70.952
2	11.14	15.16	32.920
3	18.19	22.18	23.665
4	18.43	23.16	14.054
average over cycles 2-4	16.59	20.33	23.546

c. With 20 steps per cyclotron period and 10,000 rods maximum (average gain = 12.58 dB; average efficiency = 36.7%)

1 (starting)	1.46	2.30	57.558
2	15.94	14.54	15.414
3	16.53	23.25	4.412
4	21.72	17.00	8.016
average over cycles 2-4	18.06	18.26	9.281

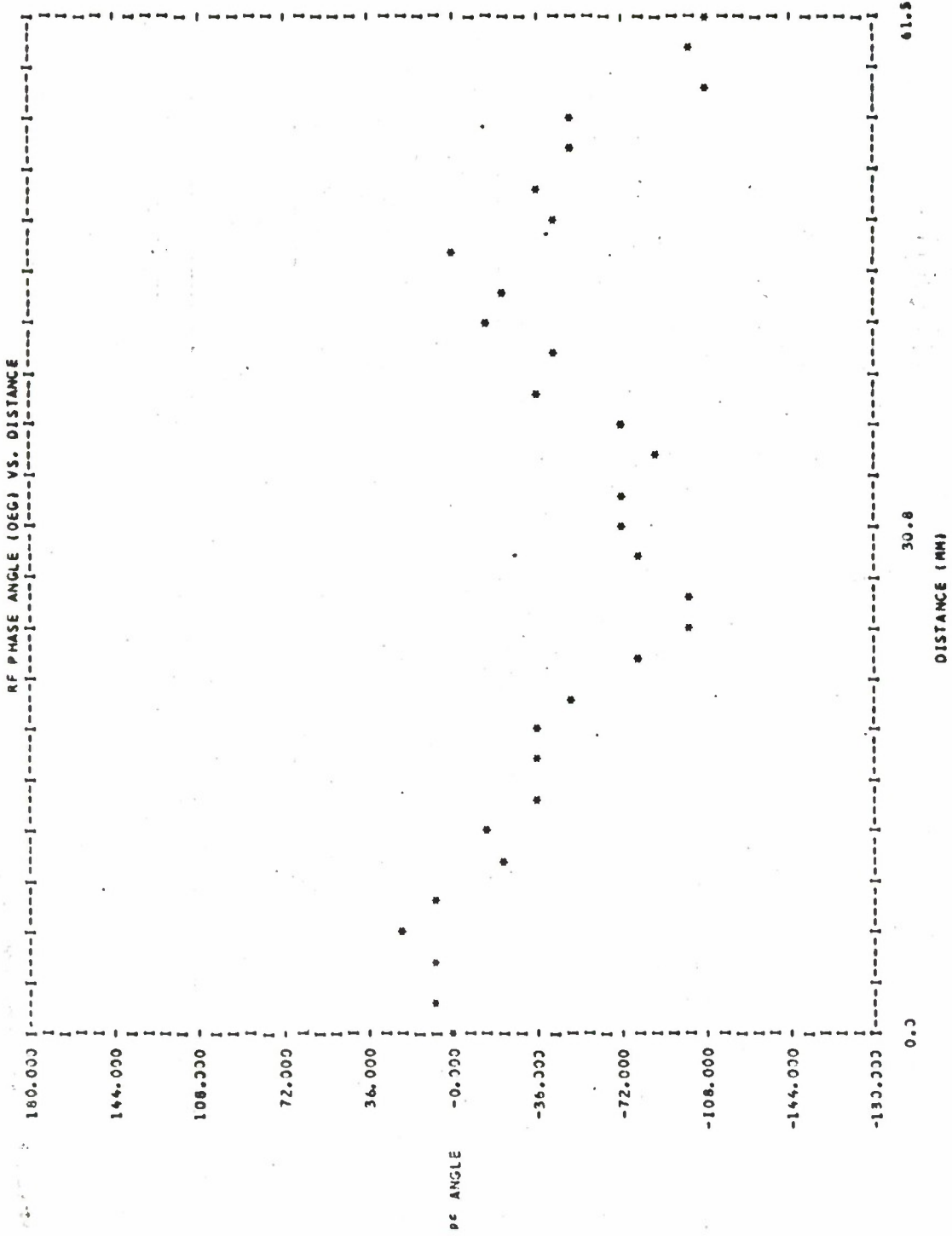


FIG. 11 COMPUTED RF CURRENT PHASE LAG IN BACKWARD-WAVE CFA WITH 6,787 SIMULATION RODS.

The equations of motion have been amended (subsequent to the runs presented in this report) so that the position advance of a particle is performed as a single step per time step. The previous algorithm is described in Appendix F of the November 1976 report;³ the present algorithm is given in Appendix C of this report. The change produces quantitative differences in the computed anode current and drive power (see Table 15) but no important differences in the qualitative behavior of the model. As before, cycles 2 and 3 differ and the current and voltage lose synchronism, as shown in Fig. 12 for these two cycles.

Among several possible methods of distributing the model charge over the 48 x 96 mesh and deriving the electric fields from the potential are the nearest-grid-point method and the cloud-in-cell method.⁹ These are illustrated in Fig. 13. The present model uses the nearest-grid-point method with the additional step of smoothing the charge density. This is done by distributing the charge equally over the nine nearest mesh points, or equivalently replacing the charge at each mesh point by the average of itself and the charge at its eight neighboring points before solving Poisson's equation. The components of potential gradients at a given point are computed from the first-order differences of values spaced two mesh intervals apart. In the area-weighting method, the four nearest points to the particles are used both for the assignment of charge and for interpolating the electric field. The charge smoothing procedure

TABLE 15

COMPUTED RESULTS IN THE QKS 1842 AT 24.3 kV
BEFORE AND AFTER AMENDMENT OF EQUATIONS OF MOTION

a. Before

<u>Cycle</u>	<u>Anode Current (A)</u>	<u>Sole Current (A)</u>	<u>RF Drive Power (kW)</u>
1 (starting)	7.82	3.62	104.453
2	12.36	17.94	41.460
3	15.07	20.58	11.562

b. After

1 (starting)	5.35	9.27	46.938
2	11.59	16.29	24.060
3	10.47	3.39	12.079

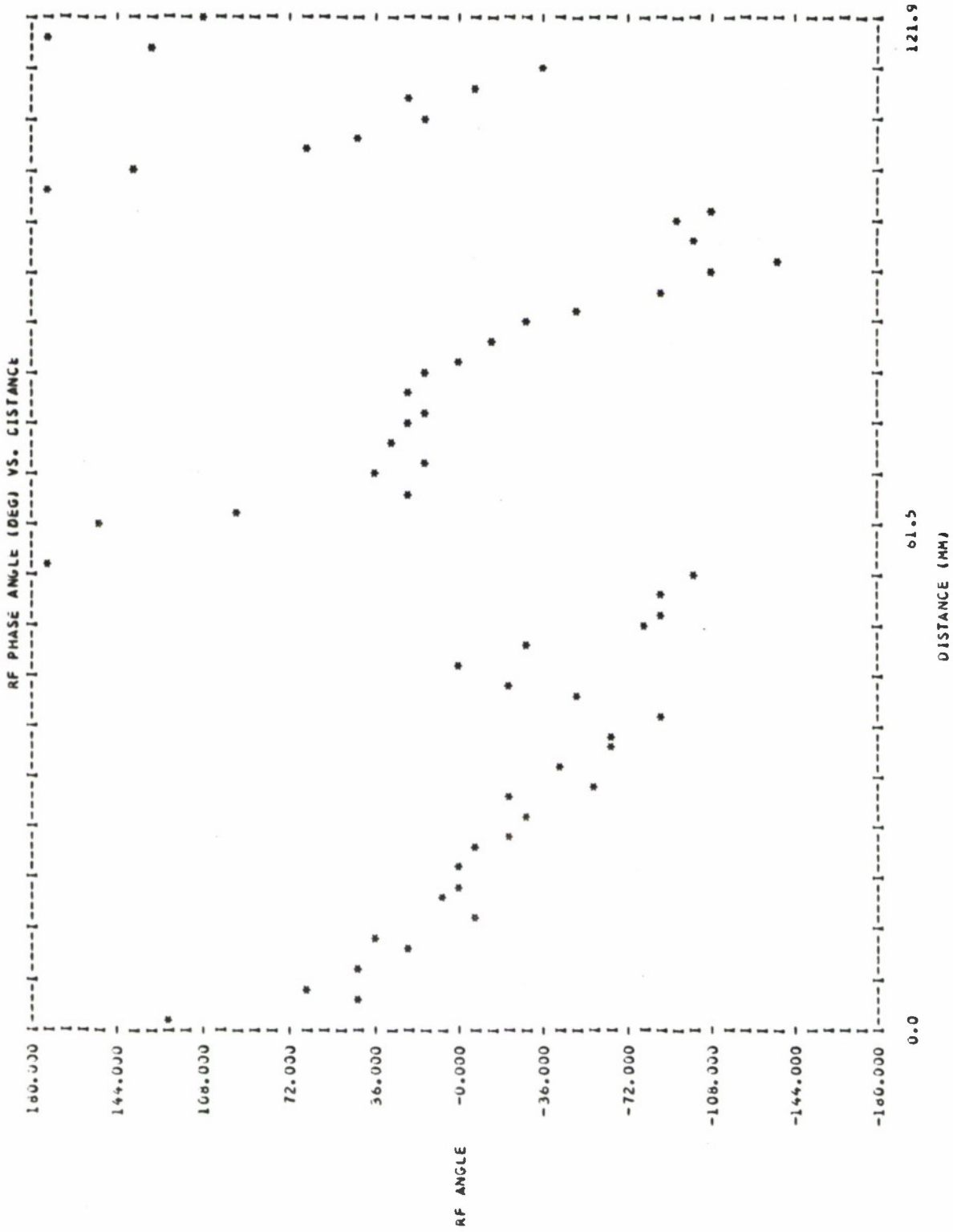
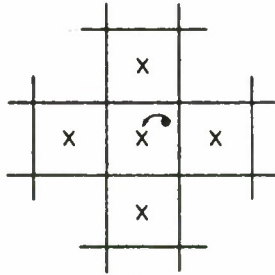
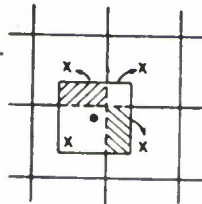


FIG. 12 COMPUTED RF CURRENT PHASE LAG IN THE QKS 1842 WITH AMENDED EQUATIONS OF MOTION.



Nearest-Grid-Point Method



Cloud-in-Cell Method

FIG. 13 METHODS OF ASSIGNING THE CHARGE OF A PARTICLE ON A DIFFERENCE MESH FOR THE SOLUTION OF POISSON'S EQUATION.
(Potter⁹)

is omitted. A test of this latter method shows it to be unsuitable because it is found that the computed sole bombardment and the secondary-emission current are too low to maintain the beam. However, the computed currents induced on the RF circuit during the first 80 time steps are almost identical for both methods. The nearest-grid-point method with charge smoothing is being retained.

IX. Starting Conditions

A. Introduction. The RF drive power required to operate a CFA depends on the minimum power level that will cause the beam to build up and synchronize with the RF wave. Here, ballistic theory for a cold secondary-emitting cathode is used for a comparison with measurements as an initial assessment of the mechanisms involved. The ballistic theory predicts the correct trend of the minimum starting power as the frequency increases on the QKS 1705. It also predicts the higher drive required in the QKS 1842, but the calculated increase of the required RF power as the magnetic field and voltage are raised is contrary to the effect measured in the QKS 1705 since the actual tube starts with a lower RF drive power at a higher magnetic field.

It is implicitly assumed that the starting process can be separated into two parts:

1. In the initial charge buildup, secondary emission must develop the beam starting with a few thermal or field-emitted electrons, and space-charge forces are negligible.

2. The subsequent buildup of RF power on the circuit may take several transits around the device and is expensive to simulate realistically.

Neither the ballistic theory nor the present SAI program (which treats a steady RF state) can predict the buildup time or the mode that eventually develops. The aim is to estimate the conditions required for starting, particularly the minimum RF drive power.

B. Experimental Results. The observed behavior of the QKS 1705 in the 9.5-9.7 GHz range is shown in Fig. 14 (supplied by Raytheon Company) and the voltage and magnetic-field data are shown in Table 16.

For the QKS 1842, similarly detailed results are not available. In general, however, the experimental data has indicated that a minimum drive power of approximately 2.5 kW (3 dB below the normal 5.5 kW operating drive) is necessary to start the tube over the range of voltages required for the full 9.5-10 GHz frequency band.

C. Analytical Theory. Shaw² has presented a simple analytical treatment. His theory is ballistic and yields the backbombardment energy of electrons that are returned to the cathode in one cyclotron period and which have a mean velocity component parallel to the cathode in synchronism with the RF wave. Eight principal factors in the theory determine the minimum RF drive power for starting:

Tube--QKS 1705, Model 270
Pulse length = 0.44 μ s
Duty factor = 0.001
Pulsed anode current = 25 A at
10 GHz

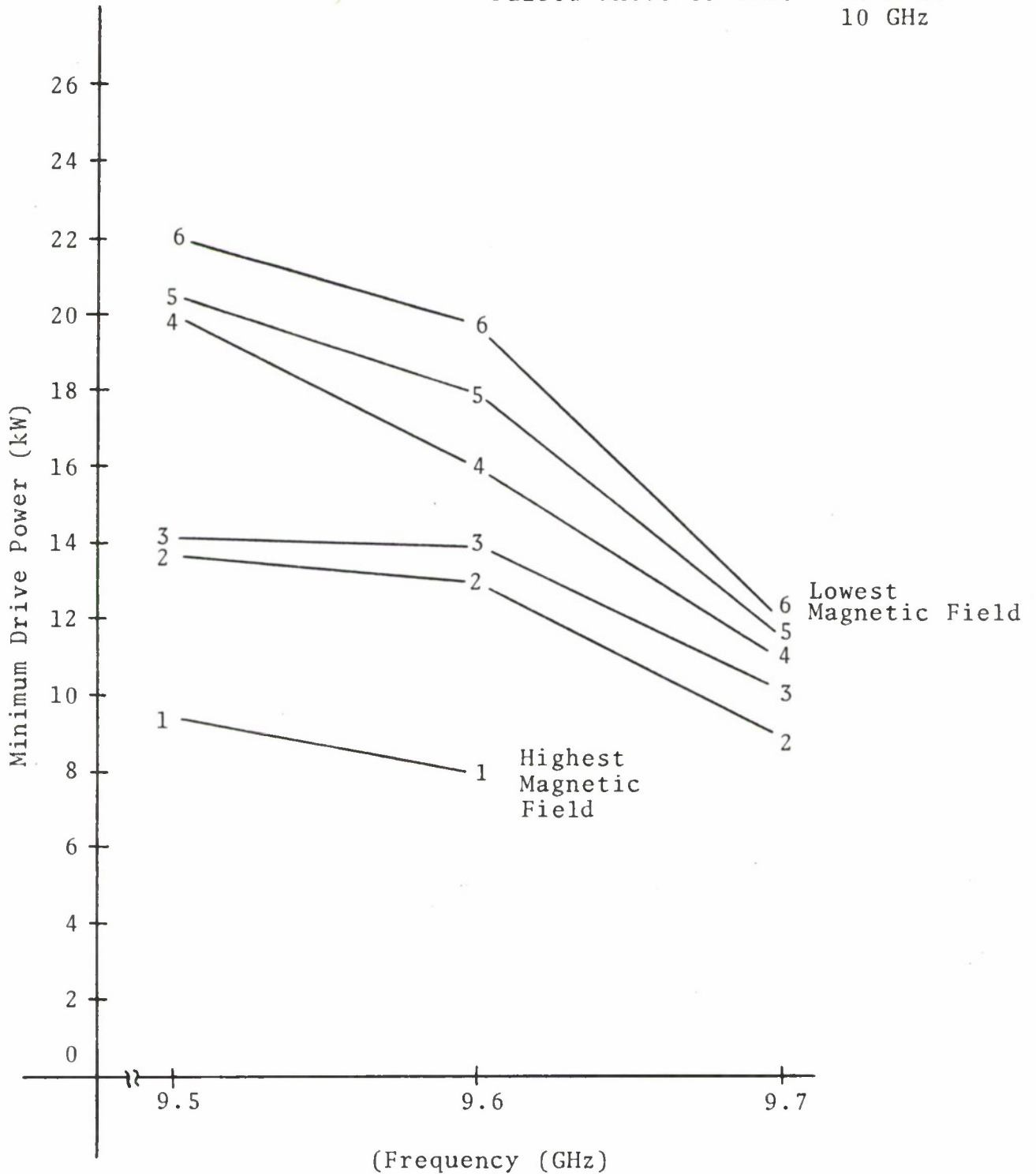


FIG. 14 MEASURED MINIMUM RF DRIVE POWER FOR STARTING THE QKS 1705 AT VARIOUS FREQUENCIES AND MAGNETIC FIELDS.*

*Furnished to J. E. Rowe by Raytheon Company, December 1976.

TABLE 16
OPERATING VOLTAGES AND MAGNETIC FIELDS USED FOR
MEASURING STARTING CONDITIONS IN THE QKS 1705 CFA

Measurement Set Number	Solenoid Current (A)	Magnetic Field (T)	Anode Voltage (kV)	
			At 9.5 GHz	At 9.7 GHz
1	0.60	0.3725	32.0	33.3
2	0.58	0.3654	31.5	32.2
3	0.55	0.3514	30.2	31.0
4	0.53	0.3421	29.4	30.0
5	0.50	0.3292	28.6	29.3
6	0.48	0.3208	27.7	28.2

1. The minimum electron impact energy for a secondary-emission coefficient greater than unity determines the threshold condition for charge buildup.

2. The higher the RF field, the greater the impact energy of electrons returned to the sole (cathode).

3. A higher RF impedance requires a lower drive power to produce a give RF field.

4. A lower value of the phase angle βa from anode to sole gives a greater RF field at the sole (cathode) for a given power level.

5. A lower magnetic field increases the height, y , attained by cycloiding electrons emitted from the sole and, hence, increases their backbombardment energy since the longitudinal RF electric field increases as $\sinh(\beta y)$.

6. Under the assumption of synchronism of the average velocity with the RF wave, the most favorable emission phase is the center of the accelerating half-cycle of longitudinal electric field.

7. If the RF wave and the crossed-field drive speed E_0/B (with space-charge forces neglected) are out of synchronism, the electrons return to the cathode in an unfavorable phase and require a higher RF field to supply sufficient impact energy.

8. As well as supplying sufficient bombardment energy, the dc and RF fields must maintain the phase of the electrons in the favorable range for repeated impacts so that secondary charge can multiply.^{2,10}

A fundamental assumption in the present ballistic theory is that the anode-sole voltage is constant in time as the charge builds up. The theory does not distinguish between cathode-pulsed and RF-pulsed operation. At least in cathode-pulsed tubes such as the QKS 1705 and QKS 1842, the anode-sole voltage builds up over several RF cycles and may overshoot if starting does not occur sufficiently rapidly. However, the results of the simple analytical calculation are of interest as a necessary first step in the investigation.

First define the following symbols:

<u>Symbol</u>	<u>Definition</u>
a	Anode-sole spacing, m
B	Magnetic field, T
b	[(Beam drift speed, E_0/B)/(RF phase velocity)] - 1
E_0	Direct electric field, V/m
P_{min}	Minimum RF drive power, W, for a given backbombardment energy
r_a	Anode radius, m
r_c	Cathode (sole) radius, m
V_a	Anode-cathode voltage, V
V_b	Backbombardment energy, eV
Z_0	Interaction impedance, Ω , on the RF circuit
z	Distance, m, along sole from the position where the RF phase gives a maximum accelerating longitudinal electric field
β	RF phase constant, m^{-1} ; ω /(phase velocity on the anode), m^{-1}
n	Electron charge /(electron mass), C/Kg

ω Angular frequency of RF signal
 ω_c Angular electron cyclotron frequency, ηB

For a given backbombardment energy V_b (eV), the RF drive power P_{\min} (W) is given by

$$P_{\min} = \frac{1}{2Z_0} V_b^2 \left(\frac{\omega_c}{\omega}\right)^4 \frac{\sinh^2 \beta a}{4\pi^2 \cos^2 \beta z} \quad (2)$$

The asynchronism parameter, b , corrected for cylindrical geometry is given by

$$1 + b = \frac{V_a \beta}{B(r_a - r_c)\omega} \cdot \frac{[(r_a/r_c) - 1](r_a/r_c)}{\ln(r_a/r_c)} \quad (3)$$

The calculated minimum drive powers at synchronism and the actual asynchronism parameters for the QKS 1705 and QKS 1842 tubes are shown in Table 17. The measured minimum RF drive powers are shown for comparison. The approximate analytical theory predicts the correct trend of lower starting power with increasing frequency in the QKS 1705 through the decrease of βa and the increase of impedance (as in Table 9). It also predicts the higher drive power required in the QKS 1842 because of the lower RF impedance and higher values of βa and ω_c/ω . It does not predict the fall of starting power with increasing magnetic field in the QKS 1705.

Shaw² makes several simplifying assumptions in deriving Eq. 2, notably

1. Planar anode and sole,
2. A single interacting RF space harmonic,
3. Near synchronism of the RF wave with the drift speed

E_0/B ,

TABLE 17

CALCULATED AND MEASURED RF DRIVE POWERS
FOR STARTING THE QKS 1705 AND QKS 1842 CFA'S

	QKS 1705 Model 270					QKS 1842		
	9.5	9.5	9.5	9.5	9.5	9.75	9.75	
Frequency (GHz)	27.5	28.5	29.5	30.5	31.5	32.0	32.5	24.3
Anode-Sole Voltage, kV	0.3208	0.3292	0.3421	0.3514	0.3614	0.3725	0.3614	0.4114
Magnetic Field, T	1.06	1.03	0.991	0.965	0.929	0.911	0.953	0.8461
(Drive Frequency/ Cyclotron Frequency), (ω/ω_c)	2.82	2.82	2.82	2.82	2.82	2.82	2.72	2.99
Normalized Anode-Sole Distance, βa	132.0	132.0	132.0	132.0	132.0	132.0	132.0	107.0
Minimum Backbombard- ment for Buildup, eV	1.20	1.20	1.19	1.19	1.17	1.16	1.17	0.99
(Anode Voltage/ Hartree Voltage)	0.19	0.21	0.20	0.21	0.20	0.20	0.15	0.03
Asynchronism Param- eter, b	1.669	1.852	2.160	2.490	2.803	3.029	1.188	3.724
Minimum Drive Power, kW, for Starting	2.160	2.040	1.950	1.400	1.360	0.920	<1.0	~2.25
Calculated*								
Measured								

*from Shaw's theory with $b = 0$

4. $\omega/\omega_c \ll 1$ so that the phase change of the RF wave is negligible along the electron path.

5. RF electric field \ll direct electric field so that the trajectories are close to the cycloids expected in the direct field alone.

Shaw² and Vaughan¹⁰ performed exact trajectory calculations but retained assumptions 1 and 2. In the SAI work described here, the full cylindrical calculation is developed.

D. Cylindrical Ballistic Computation. A new model developed by SAI computes the electron trajectories using cylindrical configuration of the actual tube. Here, this model is used to confirm the trends predicted by the analytical theory.

Details of the model are given in Appendices D and E of this report. A noteworthy feature is the RF field calculation. This uses the geometry of the vane line and a Green's function method¹¹ to give the total field, not just a single space harmonic. However, it turns out that the single backward space harmonic used in the preceding full simulations (Sections II-VIII) is in fact an excellent approximation (see Appendix E). No impedance corrections are made in these runs. The trajectories are computed with 800 time steps per cyclotron period and the CDC-6500 computer (with a precision of 14 decimal places) is used to reduce the rounding errors.

The first set of calculations is for the QKS 1842 with a fixed RF drive of 5.5 kW at 9.75 GHz, a magnetic field

of 0.4114 T and an anode voltage of 24.3 kV. In Fig. 15, the computed bombardment energy is compared with the value predicted by Eq. 8 of Shaw² as a function of the RF phase on emission. Only electrons emitted in the accelerating half cycle return to the cathode. The numerical values are shown in Table 18. With the RF drive of 5.5 kW, the maximum impact energy of 112 eV is close to the value of approximately 107 V where the secondary-emission coefficient exceeds unity. Thus, the 5.5 kW drive power is near the minimum that will allow starting. The computed phase gains relative to the RF wave between emission and impact are also shown in Table 18 and are compared with Shaw's result² for $b = 0$ in Fig. 16.

Despite the analytical approximations, the agreement between the two theories is reasonably good. The program is, of course, more powerful and has a greater capability for extension than does the simple analysis. In its present form, the program is also able to treat RF fields that are out of synchronism with the beam, interaction with higher-order space harmonics and initial emission velocities. SAI plans to develop the cylindrical RF interaction model further to simulate an operating tube.

The results of Table 18 can be used to estimate the rate of buildup of charge over successive impacts, as Vaughan¹⁰ has done for the linear tube. For the tube to start, it is necessary that sufficient space charge be built up in a single cycle for some of the charge to cross the sever region

IMPACT ENERGY (EV) ON SOLE
VS STARTING PHASE

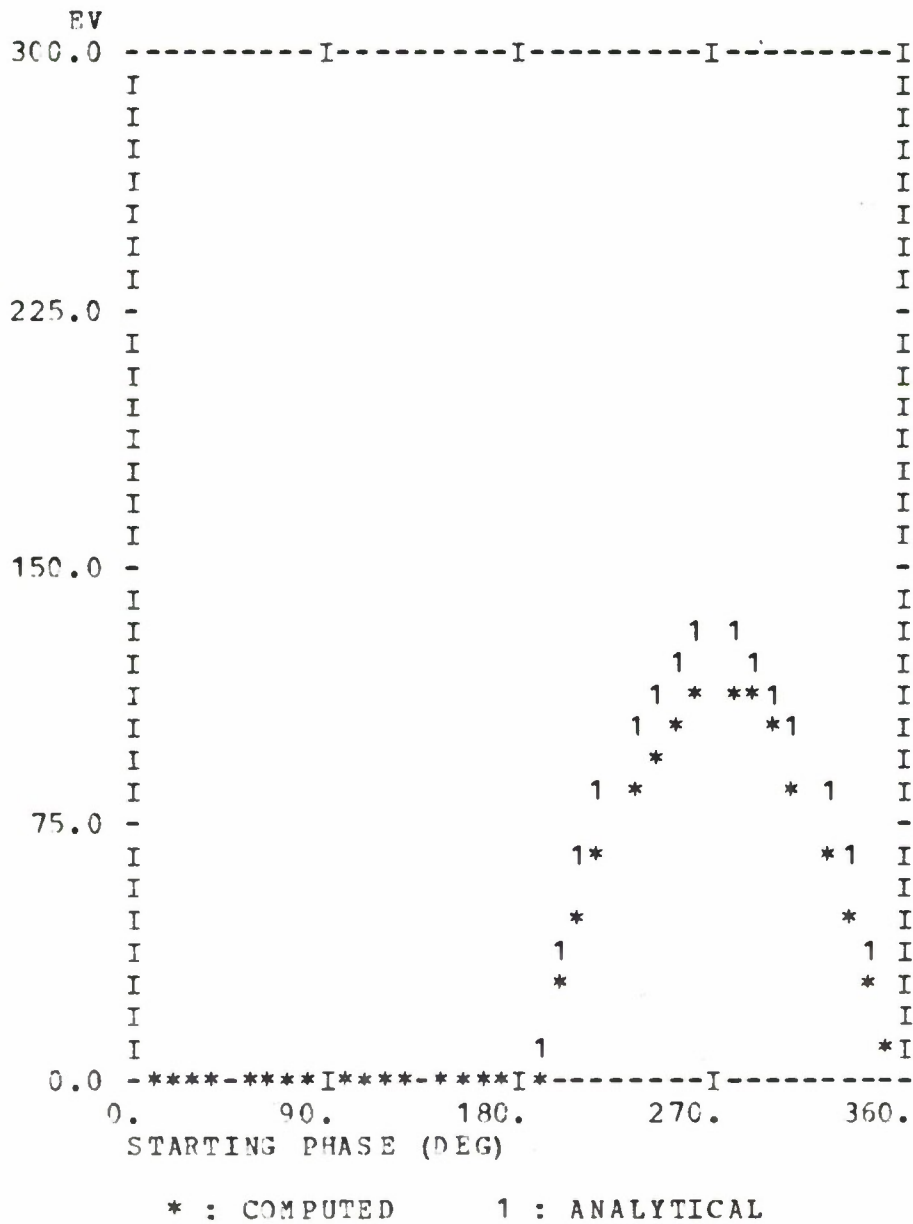


FIG. 15 COMPUTED AND ANALYTICAL CATHODE BACKBOMBARDMENT ENERGY IN THE QKS 1842 AT 9.75 GHz.

TABLE 18
 COMPUTED AND ANALYTICAL CATHODE IMPACT ENERGY
 AND PHASE GAIN IN THE QKS 1842

Emission Phase (Deg)	Impact Energy* (eV)	Impact Energy** (eV)	Computed Phase Gain	Phase Gain** with B=0
185.63	1.5	12.8	-2.9	1.9
196.88	25.0	37.8	0.4	4.0
208.13	47.5	61.4	2.2	5.5
219.38	67.4	82.7	3.5	6.7
230.63	84.3	100.7	4.5	7.6
241.88	97.8	114.9	5.3	8.4
253.13	106.8	124.7	6.0	8.9
264.38	112.3	129.7	6.5	9.3
275.63	112.3	129.7	6.7	9.5
286.88	108.3	124.7	6.8	9.5
298.13	99.0	114.9	6.6	9.4
309.38	86.6	100.7	6.3	9.0
320.63	69.6	82.7	5.6	8.4
331.88	50.4	61.4	4.6	7.4
343.13	29.1	37.8	3.2	6.1
354.38	5.5	12.8	0.6	4.0

*Computer Model

**Shaw Model

PHASE LEAD(DEG) RELATIVE TO RF WAVE
VS STARTING PHASE

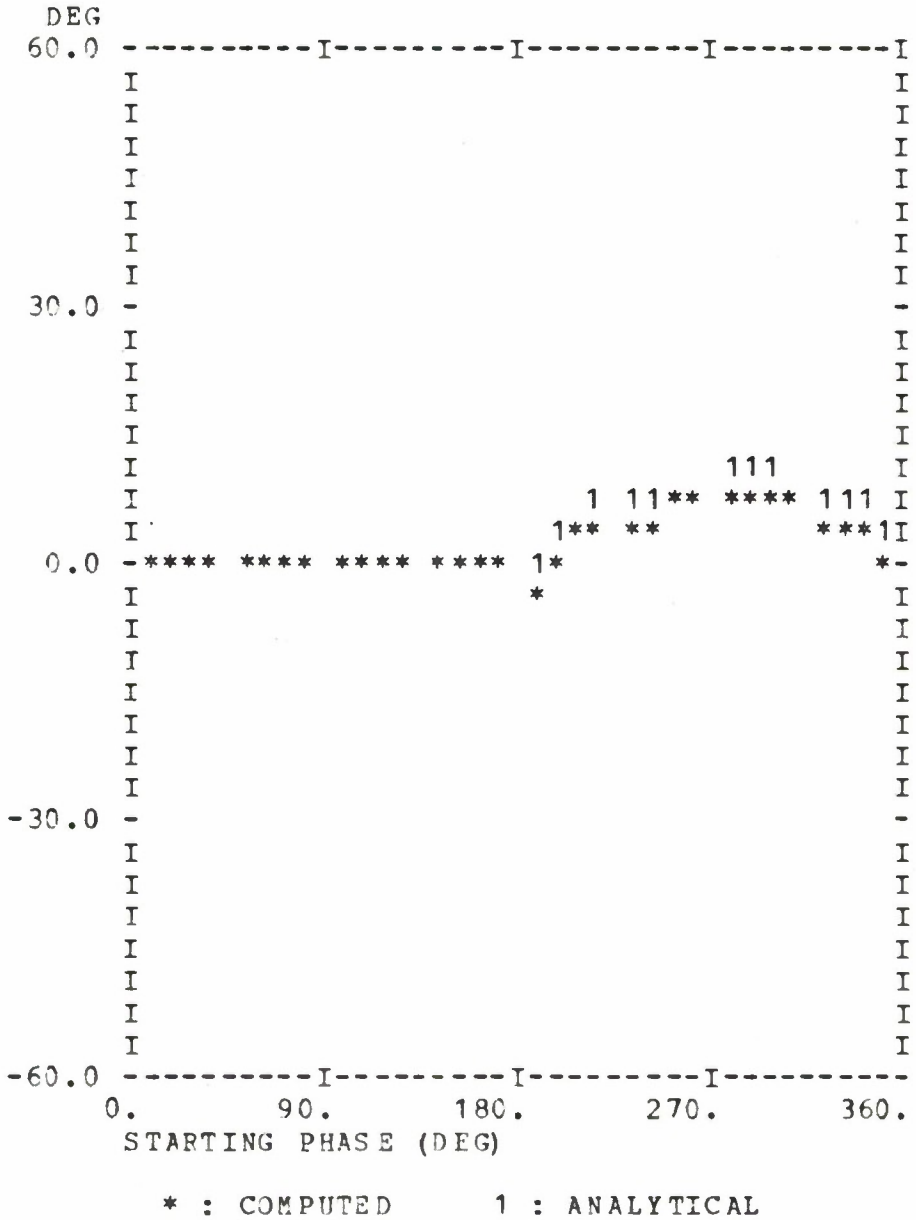


FIG. 16 COMPUTED AND ANALYTICAL PHASE GAIN PER EMISSION-IMPACT CYCLE IN THE QKS 1842.

without collection on the cathode electrode. The RF interaction region in the QKS 1842 covers seven-eighths of the circumference, or an angle of 5.5 radians.

In each cycloidal loop an electron moves approximately 0.4 radians around the tube. Thus, a maximum of thirteen successive impacts of the RF field is possible before the charge reaches the sever region. Since the RF phase change per impact is seven degrees or less in this example, all the successive impacts can lie within the favorable phase interval. However, the ballistic theory for the sever region predicts a trapping of all the cycloiding electrons because the RF field is zero there.

Inclusion of space-charge forces in the present calculation would, in principle, allow complete simulation of the buildup process. In practice, such a calculation may be very costly because of the small time step required to resolve the impact energy accurately.

The initial velocity of injection at the cathode surface has been varied in three runs, with zero emission energy, 2 eV normal to the surface and 2 eV at an angle of 30 degrees to the normal. The computed results show clearly that the trajectories are insensitive to the initial emission energy or angle. The maximum height reached above the cathode varies only between 0.503 and 0.509 of the cathode-sole distance as the emission energy is raised from 0 to 2 eV and the initial emission direction is varied from the normal to 30 degrees to the normal. The initial energy is simply

added and causes an increase of the same order of magnitude (2-4 eV) to be added to the computed impact energy, and the RF phase shift changes by two degrees or less.

The next set of runs uses the data for the QKS 1705 tube. The maximum return bombardment energies are computed at frequencies of 9.5, 9.6 and 9.7 GHz as shown in Fig. 17. The data correspond to the highest and lowest magnetic-field values, 0.3725 T and 0.3208 T, respectively, of the experimental curves of Fig. 14 and a fixed drive of 10 kW. The anode voltage is varied with the magnetic field. The qualitative trends are the same as those of Shaw's theory, despite the high values (near unity) of the parameter ω/ω_c . Notice particularly that the lower magnetic field gives a higher bombardment energy and should, therefore, require a lower minimum RF drive, not a higher value as the experimental results indicate. The computed impact energy increases with frequency, again as Shaw's Eq. 2 predicts.²

Runs with a reduced drive power of 5.5 kW show the back-bombardment energy to be proportional to the RF voltage, or to the $\sqrt{\text{drive power}}$, within two percent. The impact energy exceeds 230 eV at 10 kW drive and is well above the minimum required for charge buildup. The corresponding secondary-emission ratio is between 1.5 and 2.0 for the favorably-phased electrons even at 9.5 GHz. This result suggests that the emission threshold is not the major factor in determining the starting power in the QKS 1705 as the magnetic field is varied at a fixed frequency.

⊕ = Computed values

+ = Shaw values

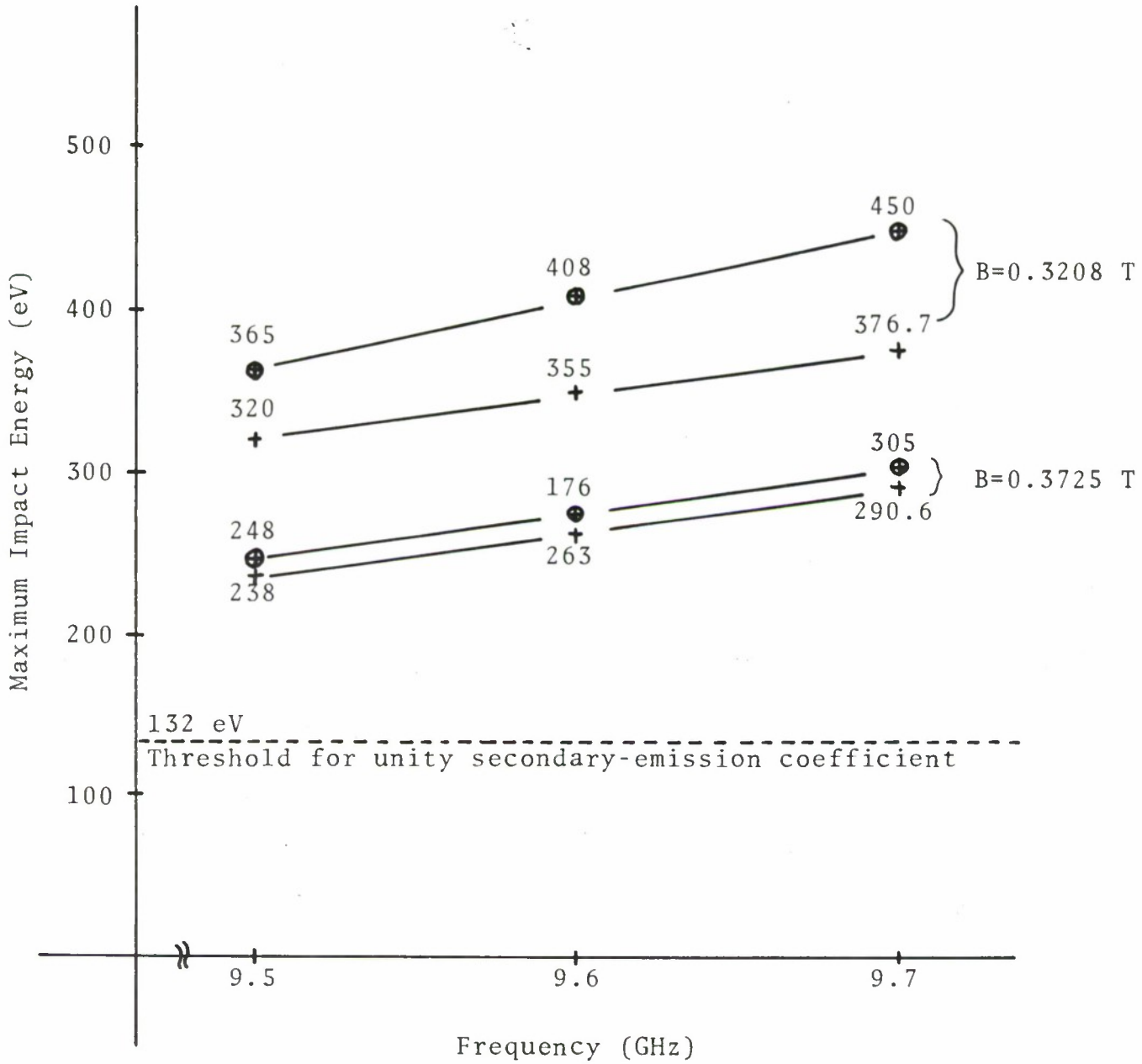


FIG. 17 COMPUTED CATHODE IMPACT ENERGY AS A FUNCTION OF FREQUENCY AND MAGNETIC FIELD IN THE QKS 1705 WITH 10 kW RF DRIVE.

The corresponding phase gains per emission-impact cycle (Fig. 18) fall slowly with increasing frequency and are almost independent of magnetic field because the anode voltage is adjusted for each run (see the operating data of Table 16). The high positive values of the phase gain suggest, however, that for synchronism these voltages should be lower (or the magnetic-field values higher) by an estimated seven percent (using Eq. 14 of Ref. 2).

The angle subtended on the axis between successive impact positions in the QKS 1705 increases from 0.43 radians at the higher magnetic field to 0.50 radians as the magnetic field is reduced from 0.3725 T to 0.3208 T. This change in turn reduces the maximum number of consecutive impacts in the RF interaction region from 13 to 12 at 9.5 GHz and to 11 at 9.7 GHz as the magnetic field is reduced. Because it is relatively small, this effect is not considered to be a critical factor in the starting curves of Fig. 14.

The QKS 1705 and QKS 1842 tubes are started by supplying the dc power under constant RF drive and the exact transient anode voltage variation during the buildup of charge is unfortunately not known. For this reason, a more detailed charge-buildup calculation has not been performed at this stage of the investigation; however, the present results show that the basic ballistic mechanisms are unaffected by the refinement of the model. Clearly other factors than these simple ballistic mechanisms are involved in the experimental results of Fig. 14 for the QKS 1705.

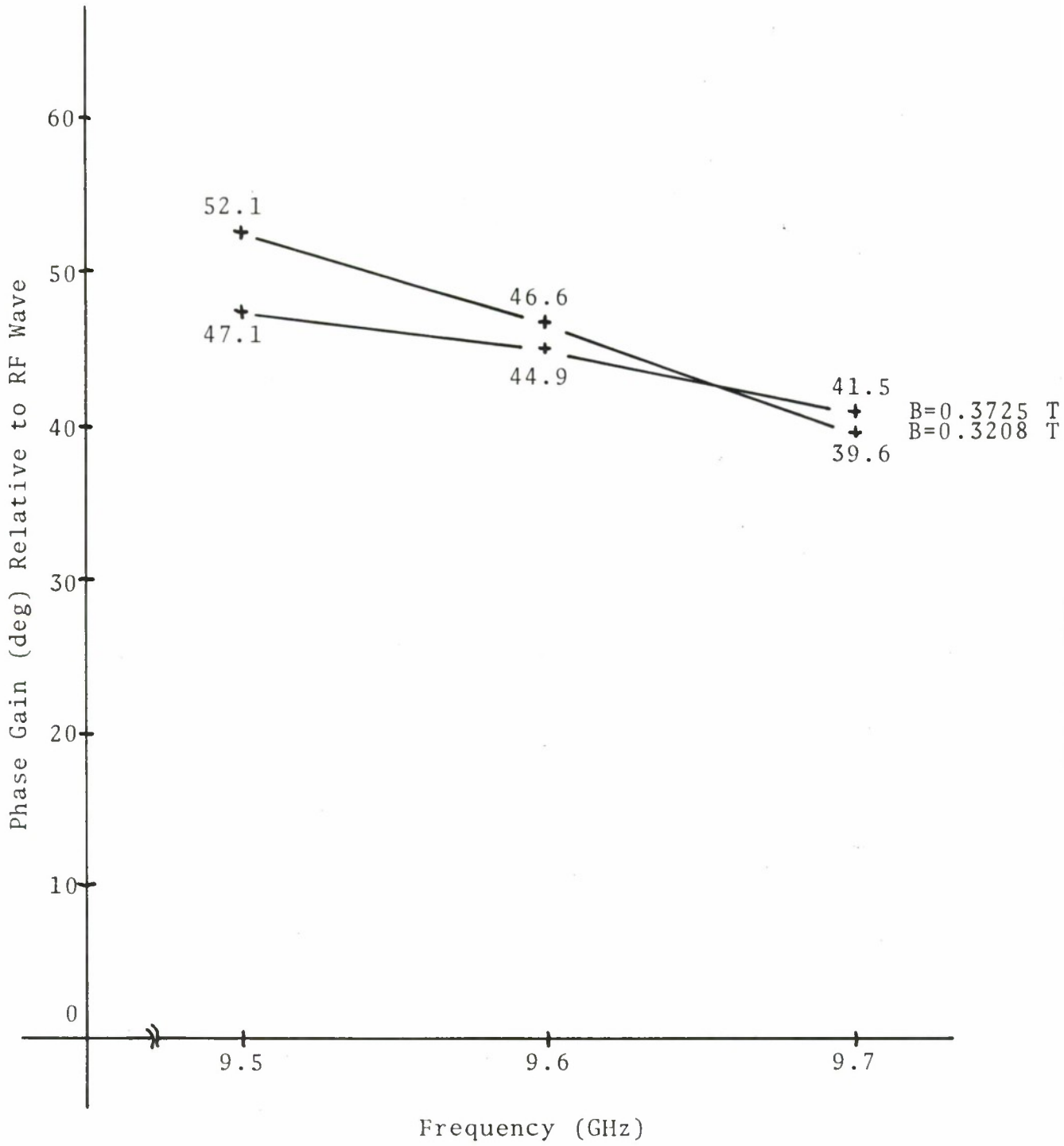


FIG. 18 COMPUTED PHASE GAIN PER IMPACT ON CATHODE IN THE QKS 1705.

E. Other Starting Mechanisms. Two other factors important in the starting process may be noise due to space-charge instabilities which may increase the sole bombardment energy and the magnitude of the RF field at the top of the hub of charge. The ratio of anode to Hartree voltage remains constant to within three percent and is apparently not a factor in the starting of the QKS 1705 under the conditions shown here. In the backward-wave CFA, power is fed back to the RF wave and flows in the opposite direction to the beam. The present simulation does not treat this transient condition. For simplification, it is assumed at present that with the magnetic field adjusted for approximate synchronism, the output power will build up once the beam has been formed.

An off-center cathode is observed to improve the starting conditions. Shaw² has described a phase-focusing mechanism for this phenomenon as the varying electric field around the tube changes the synchronism parameter, b . This mechanism requires that the cathode-anode spacing be increased at the RF input (for a forward-wave CFA) or the RF output (for a backward-wave CFA) so that the lower electric field (below the synchronous value) focuses the charge in a stable phase position relative to the RF wave as the beam buildup begins. A detailed calculation for the actual tube parameters is necessary to verify this. It would be interesting, too, to determine experimentally the effect of various directions of cathode shift on the starting conditions.

The QKS 1705 and QKS 1842 tubes operate with a constant RF drive and a pulsed anode voltage. Starting mechanisms may be influenced by the time variation of the anode-sole voltage as the pulse starts, in particular by overshoot of the voltage that can occur if starting is delayed. The transient anode voltage may also excite other modes. If a realistic time-varying voltage can be determined, it can be included in the cylindrical ballistic computation.

F. Conclusions. SAI has used a ballistic theory to study the transient behavior of a pulsed CFA with the following results:

1. The simple analytical theory is a good approximation of the detailed trajectory calculations, at least for voltages resulting in near synchronism of the electrons and the RF waves.

2. A definite minimum drive power gives a sole backbombardment energy sufficient for beam buildup by secondary emission. This drive power falls with increasing frequency in the QKS 1705, and is less in the QKS 1842, in agreement with the trend shown by the measured starting power required. However, increasing the magnetic field and voltage increases the theoretical minimum drive power while the experimental minimum drive power falls.

3. In both the QKS 1842 and the QKS 1705, the sever region is sufficiently long so that all charge is trapped under ballistic motion. The interaction region allows approximately thirteen consecutive impacts in the RF field,

which must build up space charge in a single transit around the tube.

4. The effects of the initial emission energy or angle of emission on the ballistic trajectories are negligible.

5. Ballistic theory is not sufficient to account for the observed transient behavior, at least in these tubes, in which the voltage is pulsed. Other factors are

- a. space-charge forces,
- b. feedback of RF power from the input in the opposite direction to beam motion along the backward-wave circuit,
- c. the relative magnitudes of the RF and space-charge fields at the top of a hub of charge,
- d. the transient anode voltage,
- e. possible excitation of other modes of RF interaction with different conditions of synchronism.

X. Alternative Simulation Methods

A. Statement of the Problem. The power balance in the CFA can be written as follows:

$$\begin{aligned} & \text{Anode current} \times \text{anode-sole voltage} + \text{RF drive power} \\ & = \text{anode heating (interception)} \\ & \quad + \text{sole heating (backbombardment)} \\ & \quad + \text{RF attenuation loss} \\ & \quad + \text{RF output power} \end{aligned}$$

These quantities are time averages over a pulse (which covers from about 17,000 to 34,000 RF periods in the QKS 1842). The

aim of the present (single-mode) simulation program is simply stated: to compute these powers for given values of magnetic field, anode-sole voltage, RF drive and frequency, tube dimensions, secondary-emission characteristics and equivalent-network parameters defining the RF circuit.

The fundamental properties of the DECFA which make simulation more difficult than for an injected-beam device are:

1. The interdependence of anode current and RF output power, neither of which is known from the design parameters,
2. The dependence of the current on the sole bombardment through secondary emission,
3. The possibility that a steady RF amplifying state may not exist.

In practice, the anode-sole voltage is optimized by adjusting the modulator and the magnetic field is varied for selection of an operating region, taking account of the available bandwidth and the frequency and power limits set by such properties as mode boundaries, the measured efficiency, or the available average power allowed by the design of the cooling system.

B. Time-Dependent Simulation. The present time-dependent analysis treats the particle dynamics as a transient process in which the existence of a solution does not depend on the existence of a steady state in the actual CFA. To minimize the computing time and storage required, the present SAI model treats only a single retarded RF wavelength of the

device at each time step. This RF wavelength provides a moving reference frame for viewing the beam and solving the equations of motion and power transfer to the circuit. The reference frame is given a constant speed, nominally equal to the cold RF phase velocity.

For the forward-wave amplifier, the directions of motion of the beam and the reference frame are the same: from RF input to RF output in the direction of RF power gain. A trial for the backward-wave QKS 1842 has been made as an attempt to derive the RF output power directly. The results given in Table 19 were obtained by integrating from RF input to RF output, using at the start of the first cycle the beam distribution computed from a previous run. That run was made in the reverse direction, from RF output to RF input, but excluded the sever region. The first cycle shows high gain of 16.15 dB and a high anode current of 21.7 A because the beam fills most of the interaction space. However, the beam moves back toward the sole in this and the two subsequent cycles, and the anode current is progressively less.

Apparently two effects are involved here. First, when the model follows the beam in the direction of power flow, the beam modulation at the RF input is computed immediately following the sever region. On the actual beam, the modulation at the input is produced by the RF fields in the interaction region. Second, the RF power level seen by the beam at all points up to the output is less than in the actual tube as a cumulative result of the preceding effect. This lower power level in turn produces a lower RF current than on the

TABLE 19
COMPUTED RESULTS FOR THE QKS 1842 AT 24.3 kV
WITH INTEGRATION IN THE DIRECTION OF POWER GAIN

<u>Run</u>	<u>Anode Current (A)</u>	<u>RF Drive Power (kW)</u>	<u>RF Output Power (kW)</u>	<u>RF Gain (dB)</u>
Final cycle with integration from RF output to RF input	21.67	4.076	168.0	16.15
Cycle 1 from RF input to RF output	21.54	4.076 (supplied)	290.129 (derived)	18.52
Cycle 2 from RF input to RF output	3.05	4.076 (supplied)	90.302 (derived)	13.46
Cycle 3 from RF input to RF output	0.11	4.076 (supplied)	16.201 (derived)	5.99

actual beam. This is because the actual beam experiences the full output power level at the start of its passage through the interaction region. Hence, the computed gain progressively decreases in successive cycles, as the results in Table 19 indicate.

Previous tests for the QKS 1705 tube indicated similar behavior and most of the results obtained so far have been computed by integration from RF output to RF input, in the direction of the beam motion. This procedure requires the RF output power to be supplied as an input variable to the program and applied at a fixed phase relative to the time origin of the calculation. Figure 19 summarizes the situation.

Originally, it was planned to iterate the assumed RF output power until the correct drive power was obtained. However, test simulations³ of the QKS 1705 show that difficulties are caused by (a) the need to optimize the magnetic field, (b) the need of an impedance correction factor, (c) the loss of synchronism of the beam and the RF wave before the input position is reached, and (d) the lack of a steady state even after four or five cycles around the tube. For these reasons, the present results do not resolve variations of a few percent in operating conditions, as occur in practice, for example, when the drive frequency is varied.

C. Iterative Procedure. An iterative procedure has been tested involving separate calculations of the beam motion from output to input and the RF power gain from input to output. The steps in this procedure are as follows:

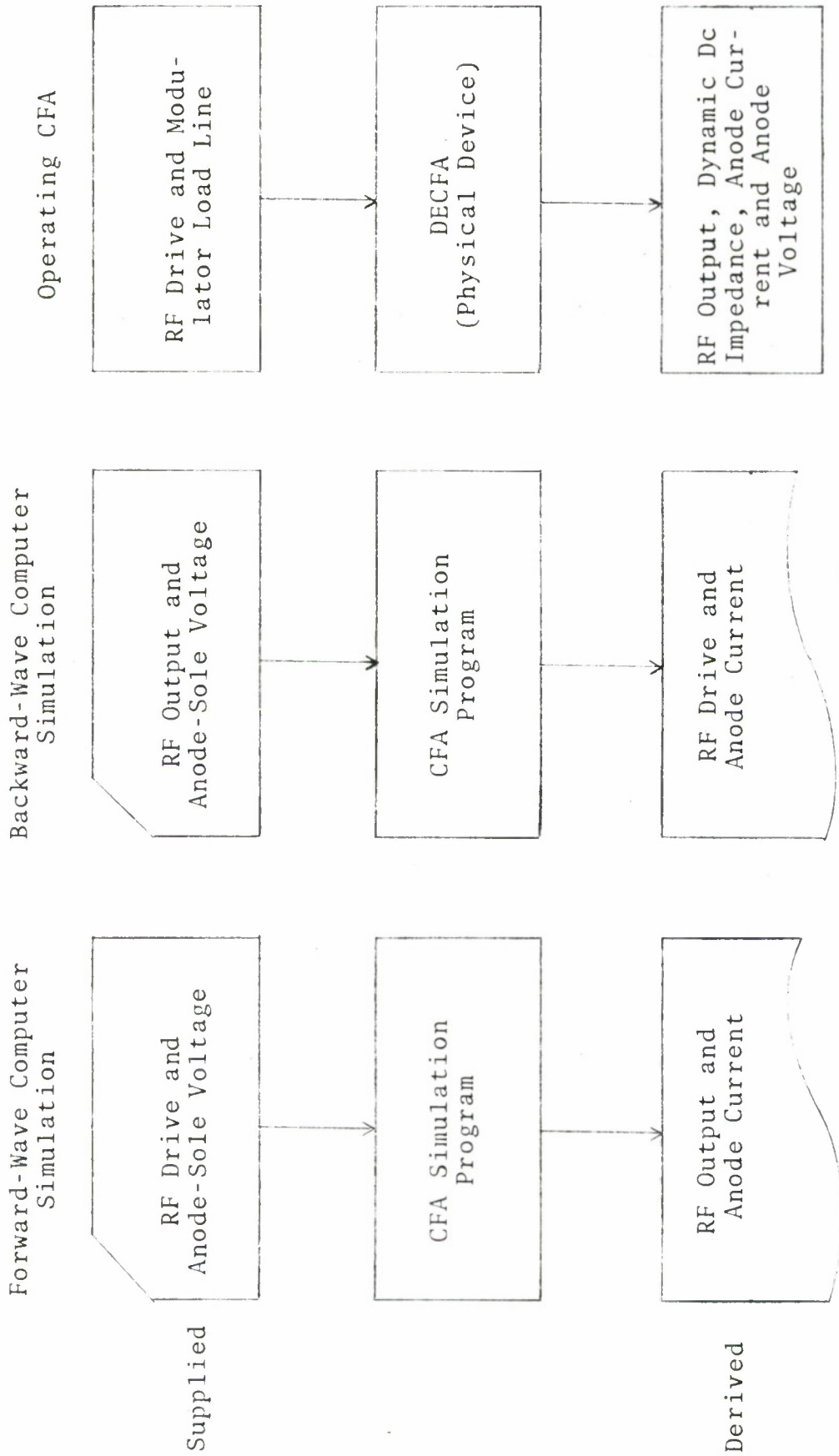


FIG. 19 COMPARISONS OF DEPENDENT AND INDEPENDENT VARIABLES IN THE CFA AND THE SIMULATION MODELS.

1. Supply an initial RF output power and an RF drive power and assume an exponential power variation from input to output. Use the cold-circuit phase velocity.

2. Compute the beam motion around the tube to derive the anode current and the RF driving currents (in phase and out of phase).

3. Integrate the RF-circuit equations from the RF input to the RF output using the previously calculated driving terms to derive a new RF power and hot phase distribution.

4. Apply the new RF power and phase to recompute the beam motion.

Steps 3 and 4 may be repeated iteratively. Trial runs have been made

1. Over two separate cycles around the QKS 1842,
2. With interaction impedances of 7.5Ω (as measured) and 15Ω , and
3. With magnetic fields of 0.35 T and 0.355 T to optimize beam-circuit synchronism.

The results for a single iteration (steps 1 through 3) are shown in Table 20. The magnetic-field increase to 0.355 T does not noticeably increase the computed gain. With a 15Ω impedance, the beam motion and the subsequently computed RF interaction with 5.5 kW RF drive and 168 kW output are nearly consistent. The iterated RF output power of 155 kW is close to the initially assumed value of 168 kW . Also, the iterated anode current of 16.4 A is close to the measured value of 17.1 A . However, with a 7.5Ω impedance value, the

TABLE 20
ITERATED ANODE CURRENT AND RF OUTPUT POWER
IN THE QKS 1842 FOR TWO VALUES OF IMPEDANCE

<u>Interaction Impedance (Ω)</u>	<u>Assumed Initial RF Power Profile</u>	<u>Anode Current (A)</u>	<u>Iterated RF Output Power (kW) with 5.5 kW Drive</u>
15.0	Exponential decrease from 168 kW at output to 5.5 kW at input	16.42	154.801
7.5	Same as above	7.05	52.794

self-consistent output power would be less than 52.8 kW with an anode current of less than 7.1 A. Clearly, this model requires an impedance of 15Ω , not 7.5Ω as measured.

This method is considered to be only partly successful for three reasons:

1. The iterated output power depends on the initial beam conditions and changes after successive cycles around the tube.

2. The iterated output power varies with the initial RF voltage distribution, for example, when the value of the impedance is changed for a fixed power level.

3. The most serious limitation is that trial runs show that further iterations do not converge, partly because the hot phase velocity of a backward-wave circuit falls if the RF current moves ahead of the RF voltage wave. Hence, asynchronism between beam and wave increases with each iteration.

D. Assumptions and Approximations. It is worthwhile to examine the model assumptions in order to determine possible improvements. These assumptions and approximations are listed below.

1. The interaction region has a rectangular cross section perpendicular to the magnetic field. If the actual tube is cylindrical, it is assumed that the radius of curvature of the cathode is much greater than the retarded RF wavelength.

2. The sole electrode is a smooth, perfectly conducting plane.

3. For calculations of the static electric field and the intercepted power and current, the anode behaves as a smooth, perfectly conducting plane.

4. The static electric and magnetic fields are uniform between anode and sole (but may be tapered in the drift direction provided the relative change per wavelength is small). The magnetic field is axial.

5. Motion in the magnetic-field direction is zero; this is a two-dimensional model only using rods of charge to represent the beam.

6. The electron thermal velocities are negligible in the bulk interaction; however, the user may select an initial energy for primary or secondary electrons emitted from the sole.

7. There are no neutral or ionized gas atoms present.

8. The electron-electron collision time is large compared with the transit time through the amplifier. The collisionless particle-in-cell model⁹ is then applicable to treat collective space-charge interaction.

9. The beam velocity and circuit phase velocity are much less than the velocity of light ($v^2/c^2 \ll 1$) such that motion is nonrelativistic, forces due to RF magnetic fields are negligible and Laplace's equation replaces the wave equation.

10. The relative change of the local electric field during one time step of the calculations (usually 1/20 of the cyclotron period) is small.

11. The relative change of the local electric field between adjacent mesh points (96 per wavelength; 48 in the anode-sole direction) is small.

12. The computed results are relatively insensitive to the number of simulation rods used. (Actually, results have shown that up to 4,000 rods suffice at least for good order-of-magnitude results but that 7,000 rods give greater RF gain and better beam-wave synchronism.)

13. The direct anode-sole voltage is constant throughout the time of the calculation.

14. The magnetic field is constant throughout the time of the calculation.

15. A continuous-cathode CFA is simulated in up to five cycles around the tube, including one starting cycle. The results from successive cycles differ and it is assumed that arithmetic means of the computed powers and currents over the cycles (excluding the starting cycle) are realistic values.

16. For the distributed-emission CFA, the operating state is independent of the starting process. The majority of runs have been started assuming a Brillouin beam at the RF input for a forward-wave CFA or at the RF output for a backward-wave CFA.

17. Secondary emission is uniform over each retarded RF wavelength along the cathode (sole). This space smoothing compensates for the granularity of the rod model. Time smoothing is incorporated as an option but is not used in present calculations.

18. The secondary-emission coefficient is a tabulated function of primary impact energy and is independent of the angle of primary incidence.

19. Secondary emission is suppressed when the primary electron is intercepted on the sole with the electric field directed away from the sole (the space-charge-limited condition).

20. For a two-dimensional model, secondary emission is uniform over the width of the beam (in the magnetic-field direction).

21. Secondary electrons are emitted with a constant initial energy (usually 2 eV) at a fixed angle (60 degrees) to the sole surface with alternate secondaries having opposite tangential velocity components.

22. Only a single-frequency signal propagates along the circuit.

23. The actual RF circuit is equivalent to a continuous transmission line of known fundamental phase velocity, interaction impedance and attenuation on the circuit surface. However, for the backward-wave CFA, it has proven necessary to raise the measured impedance by a factor of up to 2.

24. Only the lowest-order space harmonic is assumed to receive power from the beam. The time-averaged RF power transferred to the circuit wave via the higher-order space-harmonic fields is neglected.

25. Only a single interacting RF mode exists. Thus, at least two types of spurious interactions are ignored:

space-harmonic amplification at the drive frequency and possible oscillations at other frequencies.

26. Changes in the RF field in the magnetic-field direction are ignored. The fields used are treated as average values independent of the actual transverse beam shape for a two-dimensional model. (Actual beams show maximum anode bombardment and sole emission in the center of the transverse plane.)

27. Power propagates in only one direction along the RF circuit with no reflections. The power transfer from the beam is calculated from a first-order differential equation; this neglects the backward-traveling wave.

28. The interaction may change the RF phase velocity to a "hot value" but the periodic length of the interaction region remains unchanged.

29. The variations of the RF circuit fields across the interaction region between anode and sole are the same for both hot and cold waves. (The above two approximations conveniently reduce computing time since the interaction functions need be retabulated only at the start of each run or at a circuit taper.)

30. The RF gain per wavelength is small so that the space-charge distribution and the RF wave are approximately periodic in space at each step. The RF amplitude and phase vary slowly along the tube, i.e., their fractional changes in a single wavelength are small compared to unity. The program employs the periodicity assumption in two ways:

a. for solution of Poisson's equation, assuming that space-charge forces between electrons more than a wavelength apart are negligible because of the shielding effect of the anode and sole, and

b. imposing a periodic charge distribution by shifting particles that leave either end of the interaction wavelength forward or backward by one wavelength.

31. The distribution of charge density and velocity over one RF period at a given drive position is the same as the distribution over one RF wavelength at a given instant. This assumption is correct only if all particles move in synchronism with the RF wave and gives good results with ease of computation. However, it is not applicable to the calculation of time harmonics or intermodulation products on the circuit.

32. The RF wave on the circuit and the space-charge distribution are approximately periodic in time at each position along the tube, i.e., any modulation period is large compared to the RF period. In the continuous-cathode CFA, there is probably no steady RF state (and high noise levels are observed as a result). Hence, it is not expected that results computed from successive cycles around the device will be exactly the same. Both in the real tube and in the model, it is not necessary that the transit time of a bunch or spoke of charge around the tube be an integer multiple of the RF period.

33. It is implicitly assumed that a time-stepping solution of the equations of motion combined with a space-stepping

procedure for integrating the circuit wave around the tube will yield a realistic solution. An alternative procedure, calculating the motion throughout the entire tube in time steps, requires more computing time and storage.

Of those listed, the major approximations are considered to be:

1. The continuous transmission-line model for the RF circuit with a single space harmonic as in a linear device,
2. The angular periodicity and the single mode of operation enforced by the interacting RF field treated.
3. The restriction of calculations to a single RF wavelength and the space-stepping procedure for the restricted reference frame,
4. The rectangular electrode configuration,
5. The limited number of cycles around the tube (normally not more than five),
6. The two-dimensional model.

E. Proposed Cylindrical Model. The next refinement that should be tested is to treat the entire device as a two-dimensional cylindrical interaction region. Then the positions of particles all around the tube would be known at every time step and the RF driving currents and the circuit voltage distribution would be known. Such a model has already been developed by Dombrowski and Price¹¹ and Surti¹² at the University of Connecticut for simulation of the amplitron and of a cylindrical injected-beam forward-wave CFA with beam injection in the magnetic-field direction. The latter

device has 62 vanes, including 10 in the sever region. The Connecticut calculations do not include secondary emission, use only 1,100 simulation particles and use a relatively coarse potential mesh of 128 spaces around the cylinder by 16 spaces between the anode and sole. The RF-circuit field is the total field due to the potentials on all the vane tips and is computed using a Green's function tabulated on a mesh of 49 spaces in the angular direction (covering about 22.5 degrees on each side of a given vane) by 40 spaces in the anode-sole direction. In contrast, the SAI program uses 96 spaces per retarded wavelength and 48 in the anode-sole direction for the solution of Poisson's equation, and the RF field is included in this solution with a single space harmonic. By treating the total field due to the vanes, the Connecticut^{11,12} model automatically includes all space harmonics and the corresponding amplifying modes at the drive frequency. The model is applicable equally well to forward-wave and backward-wave amplifiers.

The cylindrical model resolves the RF field into Fourier components that have angular periodicity instead of using the space harmonics appropriate to a linear structure. Dombrowski¹³ and Smith¹⁴ have suggested for a reentrant tube that the interacting space-charge waves also have angular periodicity (the rotating-wave hypothesis). Their theory was developed for the amplitron which has relatively few (11) vanes and a sever region between two adjacent vanes. However, experimental measurements by Steyskal¹⁵ suggest that the reentrant tubes such as the QKS 1705 and QKS 1842 (which

have 40 vanes including 4 within the sever region) may also behave in this way.

Under the rotating wave hypothesis, the various interacting modes at a given frequency correspond to space-charge waves of differing angular periodicity but have the same time period as the drive signal. By treating the entire tube throughout, the full cylindrical calculation imposes only the reentrancy boundary condition. It can thus treat all possible interaction modes. It can also verify whether a steady state exists without the fluctuations of output power and anode current predicted by the present model. In fact, the results of Dombrowski and Price¹² for the forward-wave CFA shows that the RF output voltage does not, in general, attain a steady-state level because of the feedthrough of beam modulation in the sever region between the RF output and input. However, no difficulties were encountered in starting the RF buildup in the simulation and realistic output powers were obtained. An increased characteristic impedance was used as a convenient means of speeding the initial buildup process.

The Connecticut method^{11,12} appears promising for a simulation of the CFA's of present interest given that sufficient computer time and memory are available. A simulation of the QKS 1842 with secondary emission would require about 60,000 particles and a 1,441 by 44 mesh in order to cover the 15 wavelengths around the device with the same resolution as at present. A coarser model may well prove adequate.

SAI has applied this method initially for a ballistic trajectory calculation in constant RF fields with the realistic geometry of the vane line (see Section IX and Appendices D and E). This computation uses only 32 particles and is economical of computer time. It has provided a convenient starting point for development of the new model.

As the next stage, it is proposed to develop the RF circuit model using the equivalent network method described by Dombrowski and Price.¹² The preliminary calculations will be made for an amplatron rather than for the present Raytheon tubes since the lower number of vanes in the amplatron requires less computing time. Initially, too, angular space-charge forces will be neglected and the cathode will be treated as a uniform thermal emitter. The results of Smith¹⁴ suggest that the model should be able to demonstrate mode selection at differing anode voltages. This property will be investigated further.

XI. Computation Time and Cost

In refining the simulation, it is necessary to consider the available machine capability and the cost. SAI has performed most of the simulations on the Michigan State University CDC-6500 computer because of the low cost. In Table 21, the cost and CPU time for a 300-step run are compared with those for other computers on which versions of the program have been run. The CDC machine has only 61,440 decimal (170,000 octal) 60-bit words available to the user. This is sufficient for up to 5,500 rods. (The 4,000-rod program

TABLE 21

COMPUTER COMPARISON FOR DECFA SIMULATION
WITH 300 TIME STEPS AND A MAXIMUM 4,000 RODS

<u>Computer</u>	<u>Elapsed Time*</u>	<u>CPU Time</u>	<u>Cost</u>
University of Michigan Amdahl 470V/6	≈ 3 minutes	2 minutes	\$60
Michigan State University CDC-6500	≈50 minutes	11 minutes	\$30
Naval Electronics Laboratory Center IBM 360/67	≈60 minutes	30 minutes	not known
Naval Electronics Laboratory Center PDP-11/40	≈8.3 hours	not known	not known

*dependent on system load

requires 52,900 decimal 60-bit words.) The 6,787-rod simulation described in Section VIII cost about \$110 per 300 steps on The University of Michigan Amdahl 470V/6 computer.

Although the cost is high, the actual time required on the University of Michigan computer is only three minutes. Thus, a larger program is certainly a practical possibility. Ample core storage of 1 million 32-bit words is also available.

A further possibility for a larger program is to use a small computer to full capacity. SAI installed an earlier version of the program on the Digital Equipment Corporation PDP-11/40 minicomputer at the Naval Electronics Laboratory Center (NELC).^{16,17} The NELC work included tests which demonstrated that the numerical precisions of the Amdahl 470V/6, the IBM 360/67, the CDC-6500 and the PDP-11/40 are adequate and do not produce significant errors in the simulation results. Because the PDP-11/40 computer uses a 16-bit word, a program cannot directly address more than 32K words. For this reason, the DECFA program had to be adapted especially for the memory partitions allowed by the hardware and it was necessary to store the rod arrays on disk. The execution time of 8.3 hours per cycle is also inconveniently long. A minicomputer which is more suitable is the Harris 6024/4, which has a 24-bit word and is about as fast as the single precision IBM 360/67.

XII. Summary and Conclusions

A. General Objectives. To reduce the high cost of experimental tube testing, it is desirable to be able to obtain theoretical predictions of the performance of a given design. Because of the complexity of crossed-field interaction, a computer simulation is necessary. The results desired for such a simulation are:

1. Clarification of the distinct physical mechanisms affecting steady-state operation.
2. Quantitative predictions of anode current, RF output power, gain, efficiency and anode and sole heating for given values of magnetic field, RF drive and frequency, anode-sole voltage, tube dimensions, secondary-emission characteristics and equivalent network parameters for the RF circuit.
3. Predictions of performance over a given frequency band, particularly variations in efficiency, anode current and voltage as the drive frequency is changed.
4. Predictions of limits to bandwidth set by loss of efficiency or interfering modes.
5. Predictions of the minimum RF drive power required for starting the CFA as a pulse begins.

Even with a reliable model, the amount of computation required to reproduce a complete performance chart would amount to tens of runs, each costing \$100 or more. Therefore, a study is restricted to specific parameter values in the vicinity of the desired operating voltage, magnetic field and RF drive power.

As the first stage in developing a useful model, the SAI program has been run for tubes of known performance in order to correlate theory and measurement. The results described in this report and summarized below show at least good qualitative agreement with experiment and give insight into the electron dynamics in both forward- and backward-wave CFA's. However, a more refined calculation is necessary for quantitative predictions.

B. Comparison of the QKS 1705 and QKS 1842 Tubes. The QKS 1842 CFA is a newer design than the QKS 1705, with a smaller anode circumference and a smaller vane spacing, which gives a reduced RF phase velocity and a reduced interaction impedance over the 9.5-10 GHz frequency band. Consequently, the QKS 1842 requires a lower beam drift speed for synchronism, which is provided by a higher magnetic field and a lower operating voltage. The Brillouin circulating current is 65 A in the QKS 1705 and 35 A in the QKS 1842 at 9.75 GHz. The QKS 1705 provides up to about 500 kW RF output. The QKS 1842 was originally designed to provide about 200 kW peak over the entire 9.5-10 GHz band, but, in fact, provides 175 kW and 17 A over a reduced bandwidth with a 5.5 kW RF drive. The efficiencies of both tubes are approximately 40 percent. The QKS 1842 tube has also given difficulties in starting.

The reasons for the low output power, the restricted bandwidth and the starting problems are not well understood.

An aim of the present simulation project was to compute such trends and thus account for the many separate physical effects with a single model.

C. Summary of Results. The noniterative backward-wave CFA program is restricted to deriving the RF drive power and anode current when the RF output power is supplied. However, the results have yielded several qualitative observations:

1. The interacting beam fills most of the interaction region and the width of a spoke of charge along the RF circuit limits the efficiency because of anode bombardment in regions of unfavorable phase.

2. The RF current induced on the circuit accelerates ahead of the RF voltage wave as the power level falls from the output toward the input.

3. The output power, phase angle and direct anode current do not show steady-state values in successive transits around the tube. The anode current, for example, varies by up to 24 percent of its mean in the forward-wave CFA calculations and by 20 percent of its mean for the QKS 1842 (backward wave). These variations are thought to be real, although their size may be exaggerated because of the limited number of rods in the model.

4. The anode currents computed in the backward-wave CFA's clearly increase with the RF output power when this is supplied to the program and are larger for the QKS 1705 than for the QKS 1842 by a factor of between two and three.

In fact, the QKS 1842 current shows good agreement with measured values (when the RF impedance is doubled). For the QKS 1705, the computed current is higher than measured, possibly because the assumed beam width of 14.8 mm is too high.

5. The runs for the QKS 1705 and QKS 1842 behave similarly, showing bunched beams of similar shape and similar RF current phase-distance characteristics. Thus, both tubes operate in the same manner (neglecting interfering modes) once they are started.

6. The efficiency of both tubes is limited to approximately 40 percent because the beam forms a broad bunch and fails to synchronize perfectly with the RF wave. Increasing the number of rods in the model improves the synchronism, however.

7. The interaction impedance must be doubled for realistic gain in the backward-wave tubes. This suggests that the computed loss of synchronism is unrealistic.

8. The model is more accurate when the ratio of RF to direct voltage is higher, as in the forward-wave SFD-243, for which the given interaction impedance needs no correction. In the backward-wave tubes, the ratio of RF to direct voltage is less by a factor of about three (Table 10). Hence, the ratio of the RF field to the space-charge field is also smaller.

9. In both the QKS 1705 and QKS 1842 simulations, the cathode maintains the beam by providing secondary electrons

and good beam stability results. However, the detailed effects of the secondary emission vs. impact energy characteristic are worth further study.

10. An off-center cathode in the QKS 1842 gives greater RF gain and greater anode current than the symmetrical cathode but a lower efficiency is computed.

11. Ballistic theory gives good order-of-magnitude predictions of the drive powers required to turn on a pulsed CFA, but an improved computer calculation should include the time-varying anode-sole voltage for a dc-pulsed tube.

D. Further Work Proposed. Continued work at SAI is aimed at improving the CFA modeling so as to obtain better quantitative agreement with measurements for a single operating point per run. It is recommended that an improved model be used to simulate the entire tube in each step of a transient calculation, not just a single wavelength as at present. SAI has developed a model for ballistic trajectory calculations using the cylindrical configuration and the exact RF fields. Next, it is proposed to incorporate the RF interaction and reproduce an operating condition, initially with a thermonic cathode, no angular space-charge forces and a limited number of particles. After this, the model will be developed further to simulate the present tubes.

APPENDIX A

POWER-TRANSFER EQUATIONS FOR THE RF CIRCUIT IN A CFA.

A.1 General Circuit Equations. The RF voltage $V(z,t)$ on the circuit at a distance z from the start of the interaction calculation and at time t is given by

$$V(z,t) = -V_1(z) \sin[\omega t - \beta(z)z - \theta(z)] \quad . \quad (\text{A.1})$$

Only a single interacting space harmonic is treated. The drive frequency is $\omega/2\pi$ and the cold phase velocity, which may be a function of position, is $\omega/\beta(z)$. The phase lag $\theta(z)$ gives the effect of the reactive power transferred from the beam, which slows the wave when $\theta(z)$ is positive.

The circuit equations of Yu et al.⁸ may be written as

$$\frac{dV_1}{dz} = -\alpha V_1 \pm \frac{Z_0 P_g}{V_1} \quad (\text{A.2})$$

and

$$\frac{d\theta}{dz} = \pm \frac{Z_0 R_g}{V_1^2} \quad . \quad (\text{A.3})$$

Here, the symbols are defined as

P_g = RF power transferred from beam to circuit per unit length (W/m)

R_g = reactive power per unit length, defined by Yu et al.⁸ as the power per unit length that would be transferred if the RF voltage were delayed in phase by one-quarter cycle.

The lower sign on the right-hand side of the equations is used for the backward-wave device. The attenuation constant α is positive for a forward wave and negative for a backward wave. Yu et al.⁸ derive Eqs. A.2 and A.3 for the forward-wave case. The minus sign for the backward-wave device in Eq. A.3 is omitted by Yu et al.,⁸ apparently in error since the analogous equation derived from the transmission-line equation includes it (Appendix B). With the present signs, Eq. A.3 states that the RF wave is accelerated in the direction of power flow when the beam is ahead of the RF wave in phase in the direction of wave motion.

The interaction region has a reference frame covering one retarded wavelength λ , or $2\pi/\beta$, moving with the cold phase velocity ω/β so that the position ℓ of the trailing end is given by

$$\beta\ell = \omega t \quad (\text{A.4})$$

in the case where β is constant, or in general, by

$$\int_0^\ell \beta(z') dz' = \omega t \quad (\text{A.5})$$

The relative longitudinal position z_1 in the interaction region is measured from the trailing end so that $0 \leq z_1 \leq \lambda$. Then the RF voltage V on the circuit is

$$V(\ell, z_1, t) = -V_1(\ell) \sin[\omega t - \beta(\ell)(\ell + z_1) - \theta(\ell)] \quad (\text{A.6})$$

Neglect the changes of amplitude and phase over one wavelength and use the values $V_1(\ell)$, $\theta(\ell)$ and $\beta(\ell)$ at the trailing end. Thus, the term z may be replaced by ℓ in Eqs. A.2 and A.3.

This model differs from that of Yu et al.⁸ by fixing the velocity of the interaction region and allowing the hot RF wave to change in phase by the angle θ .

A.2 Expressions for Power Transfer. In the forward-wave amplifier, power gain and wave motion are in the same direction, and the equations are solved by integrating in this direction. In the backward-wave CFA simulation an integration in the direction of wave motion uses equations of the same form as the forward-wave case but with the negative sign of impedance in Eqs. A.2 and A.3. The model can integrate these equations in either the direction of wave motion or in the direction of power flow. The latter gives the correct feedback effect of the beam power on the RF wave but incorrect beam motion unless an iterative procedure is utilized (Section X). The values of the terms P_g and R_g are the same for both directions; however, the actual expressions depend on the direction in which z is chosen to be positive. Expressions are derived here for both cases since the paper of Yu et al.⁸ is unclear about several details.

The term $P_g(\ell)$ is the time-averaged power per unit length transferred from the beam to the RF wave at position ℓ and is given by

$$P_g(\ell) = -\frac{h}{T} \int_0^T dt \int_0^a dy \rho \bar{v} \cdot \bar{E}_{RF}(y, \ell, t) \quad , \quad (A.7)$$

where T is the RF period, y is the height above the sole, $\rho(y, \ell, t)$ is the local charge density, \bar{v} is the velocity (\dot{y}, \dot{z})

and \bar{E}_{RF} is the RF electric field. Now the time distributions of charge density and velocity are not available from the present model because the charge distribution is made periodic in space with a fixed period λ and is not necessarily periodic in time with period T at a given position. Instead the spatial distribution of charge over the interaction region is used directly, as follows.

In Eq. A.7, replace the interval $(0, T)$ by the interval $(T_\ell - T, T_\ell)$, where

$$T_\ell = \frac{\beta \ell}{\omega} \quad , \quad (A.8)$$

the transit time of the RF wave to position ℓ . Now make the approximation

$$\rho \bar{v} \cdot \bar{E}_{RF}(y, \ell, t) = \rho \bar{v} \cdot \bar{E}_{RF}\left[y, \ell + \left(\frac{\omega}{\beta}\right)(T_\ell - t), T_\ell\right] \quad (A.9)$$

for $T_\ell - T \leq t \leq T_\ell$, replacing the unknown time distribution with the known space distribution over one retarded wavelength. Finally, make the change of variables

$$z_1 = \omega(T_\ell - t)/\beta \quad . \quad (A.10)$$

These transformations give Yu et al.'s⁸ equation for P_g as

$$P_g(\ell, T_\ell) = -\frac{\hbar}{\lambda} \int_0^\lambda dz_1 \int_0^a dy \rho_{beam} (\dot{y} E_{yRF} + \dot{z} E_{zRF}) \quad , \quad (A.11)$$

where the charge density, velocity and components E_{yRF} and E_{zRF} are now evaluated at time T_ℓ and position $\ell + z_1$.

The reactive power, R_g , per unit length is then derived by replacing (ωt) by $(\omega t - \pi/2)$ in the expressions for the electric field E , or equivalently, replacing (βz_1) by $(\beta z_1 + \pi/2)$. This derivation applies both for forward and backward waves; in both cases, R_g is defined as the component of power flow to the electric field behind the beam by one-quarter of the RF cycle.

The term P_g/V_1 has the dimensions of current per unit length and is a measure of the RF current induced on the circuit.

A.3 RF Current Phase Lag and Total Voltage Phase Delay.

The local RF phase lag ψ of this current from the RF wave at a given position is given by

$$\psi = \arctan(R_g/P_g) \quad (\text{A.12})$$

and is zero when R_g is zero. The quantity ψ (in degrees) appearing on lineprinter plots is designated as the "RF ANGLE."

To relate this angle to the observed total phase delay between RF output and input, notice that from Eq. A.3 the value of θ at the end of the circuit, $z = \ell_0$, is given by

$$\theta(\ell_0) = \pm \int_0^{\ell_0} d\ell \frac{Z_0}{V_1^2} P_g \tan \psi(\ell) \quad (\text{A.13})$$

When the angle $\theta(\ell_0)$ is positive, the measured hot phase delay in the direction of wave motion as seen by the beam exceeds the cold phase delay by the phase angle $\theta(\ell_0)$ or by a time equal to $\theta(\ell_0)/\omega$ seconds.

The external phase delay ϕ_{hot} as measured from input to output over a distance ℓ_o is given by the equation

$$\phi_{\text{hot}} = \beta \ell_o + \theta(\ell_o) \quad (\text{A.14})$$

for the forward-wave circuit or by the equation

$$\phi_{\text{hot}} = \pi \frac{\ell_o}{p} - [\beta \ell_o + \theta(\ell_o)] \quad (\text{A.15})$$

for the backward-wave circuit, with straps connecting alternate anode vanes, where p is the pitch of the RF circuit. The quantity ϕ_{hot} (in degrees) appears on lineprinter plots, designated as "RF DELAY."

It is seen from Eq. A.13 that when the phase lag ψ and the power transfer P_g to the circuit have the same sign the phase lag $\theta(z)$ of the hot wave increases in the direction of wave motion for the forward wave and decreases for the backward wave. It thus increases in the direction of power flow for both types of wave. Equations A.14 and A.15 then show that the observed phase difference between input and output increases in both forward-wave and backward-wave amplifiers when the circuit current lags the RF wave. If the beam and wave were in perfect synchronism throughout the tube, the phase delay would be unaltered by the interaction.

A.4 Calculation of Power Transfer for Integration in the Direction of Wave Motion. The RF voltage varies over the interaction region as

$$V_{RF} = -V_1(\ell) \sin[\omega T_\ell - \beta\ell - \beta z_1 - \theta(\ell)] \frac{\sinh \beta y}{\sinh \beta a}, \quad (\text{A.16})$$

where a is the anode-sole spacing. Hence, the RF voltage on the anode as seen by the moving frame is given by

$$V_{RF} = V_1(\ell) \sin[\beta z_1 + \theta(\ell)] \quad (\text{A.17})$$

and is used as a boundary value for the solution of Poisson's equation in the interaction region.

For computing the power transfer factors P_g and R_g , the RF electric field components are given by

$$E_{yRF} = -\frac{\partial V_{RF}}{\partial y} \quad (\text{A.18})$$

and

$$E_{zRF} = -\frac{\partial V_{RF}}{\partial z_1} - \frac{\partial V_{RF}}{\partial \ell} \cong -\frac{\partial V_{RF}}{\partial z_1}, \quad (\text{A.19})$$

neglecting $dV_1/d\ell$ and $d\theta/d\ell$ relative to βV_1 . Equation A.16 then gives

$$E_{yRF} = -\beta V_1(\ell) \sin[\beta z_1 + \theta(\ell)] \frac{\cosh \beta y}{\sinh \beta a} \quad (\text{A.20})$$

and

$$E_{zRF} = -\beta V_1(\ell) \cos[\beta z_1 + \theta(\ell)] \frac{\sinh \beta y}{\sinh \beta a}. \quad (\text{A.21})$$

Hence, P_g and R_g are given in the SAI model by

$$\begin{aligned} \frac{P_g}{V_1} &= \frac{h\beta}{\lambda} \int_0^\lambda dz_1 \int_0^a dy \rho_{\text{beam}}(y, z_1) \left\{ \dot{y} \frac{\cosh \beta y}{\sinh \beta a} \right. \\ &\quad \left. \cdot \sin[\beta z_1 + \theta(\ell)] + \dot{z} \frac{\sinh \beta y}{\sinh \beta a} \cos[\beta z_1 + \theta(\ell)] \right\} \quad (\text{A.22}) \end{aligned}$$

and

$$\frac{R_g}{V_1} = \frac{h\beta}{\lambda} \int_0^\lambda dz_1 \int_0^a dy \rho_{\text{beam}}(y, z_1) \left\{ \dot{y} \frac{\cosh \beta y}{\sinh \beta a} \cdot \cos[\beta z_1 + \theta(\ell)] - \dot{z} \frac{\sinh \beta y}{\sinh \beta a} \sin[\beta z_1 + \theta(\ell)] \right\} . \quad (\text{A.23})$$

It remains to derive the actual equations used in the computer program. Define expressions AIN and AOUT by the equations

$$\text{AIN} = \sum_{\text{all charge in interaction frame}} \text{CG} \left[\text{VY} \left(\frac{\cosh \beta y}{\sinh \beta a} \right) (\sin \beta z_1) \left(\frac{\Delta y}{\Delta z} \right) + \text{VZ} \left(\frac{\sinh \beta y}{\sinh \beta a} \right) \cos \beta z_1 \right] \quad (\text{A.24})$$

and

$$\text{AOUT} = \sum_{\text{all charge in interaction frame}} - \text{CG} \left[\text{VY} \left(\frac{\cosh \beta y}{\sinh \beta a} \right) (\cos \beta z_1) \left(\frac{\Delta y}{\Delta z} \right) - \text{VZ} \left(\frac{\sinh \beta y}{\sinh \beta a} \right) \sin \beta z_1 \right] . \quad (\text{A.25})$$

The terms VY and VZ are the normalized rod velocity components (relative to a fixed reference frame) given by

$$\text{VY} = \frac{\dot{y} \Delta t}{2 \Delta y} \quad (\text{A.26})$$

and

$$\text{VZ} = \frac{\dot{z} \Delta t}{2 \Delta z} , \quad (\text{A.27})$$

where Δy and Δz are the y- and z-spacings of the computational mesh and Δt is the time step used in the calculation.

The term CG is the number of units of normalized charge carried by a given rod (variable in order to allow for a noninteger secondary-emission coefficient).

Combining Eqs. A.22 through A.25 and replacing the terms $\rho dz_1 dyh$ by the rod charge q (a negative number), it can be seen that

$$\frac{P_g}{V_1} = \beta \left(\frac{\Delta z}{\Delta t} \right) \left(\frac{2q}{\lambda} \right) (A_{IN} \cos \theta - A_{OUT} \sin \theta) \quad (A.28)$$

and

$$\frac{R_g}{V_1} = \beta \left(\frac{\Delta z}{\Delta t} \right) \left(\frac{2q}{\lambda} \right) (-A_{IN} \sin \theta - A_{OUT} \cos \theta) \quad (A.29)$$

In some versions of the program code (subroutine CIR2), the terms P_g/V_1 and R_g/V_1 are computed with a minus sign, using the terms ADRV and ACOUT to represent the expressions $-P_g \Delta t / (\beta \Delta z V_1)$ and $-R_g \Delta t / (\beta \Delta z V_1)$, respectively. The corresponding sign reversals are also made in the program equivalents of Eqs. A.2 and A.3. The multiplier ZCN3 used in the program equals the expression $2(Z_0/V_a)(\Delta z/\Delta t)$. Here, V_a is the anode-sole voltage, which is used to normalize the RF voltage.

A.5 Calculation of Power Transfer for the Backward-Wave CFA by Integration in the Direction of Power Flow. The longitudinal coordinate z is now positive in the direction of power flow and negative in the direction of wave motion. Therefore, the differential equations are modified by

replacing z by $-z$ and using the lower sign in Eqs. A.2 and A.3, giving

$$\frac{dV_1}{dz} = \alpha V_1 + \frac{Z_o P_g}{V_1} \quad (\text{A.30})$$

and

$$\frac{d\theta}{dz} = \frac{Z_o R_g}{V_1^2} \quad (\text{A.31})$$

The attenuation constant α is a negative number and the impedance Z_o is positive. The RF voltage is now given by

$$V(y,z,t) = V_1(\ell) \sin[\omega t + \beta(\ell + z_1) - \theta(\ell)] \frac{\sinh \beta y}{\sinh \beta a}, \quad (\text{A.32})$$

defining a reference wavelength $\ell \leq z \leq \ell + \lambda$ and a relative z -coordinate z_1 as before. The anode voltage in the reference frame is

$$V(a,z,t) = V_1(\ell) \sin[\omega t + \beta\ell + \beta z_1 - \theta(\ell)] \quad (\text{A.33})$$

The reference frame is assigned the speed ω/β in the opposite direction to the beam and the wave so that

$$V(a,z,t) = V_1(\ell) \sin[2\beta\ell + \beta z_1 - \theta(\ell)] \quad (\text{A.34})$$

Differentiating Eq. A.32 gives the electric-field components now as

$$E_{y\text{RF}} = -\beta V_1 \sin(\beta z_1 + 2\beta\ell - \theta) \frac{\cosh \beta y}{\sinh \beta a} \quad (\text{A.35})$$

and

$$E_{z\text{RF}} = -\beta V_1 \cos(\beta z_1 + 2\beta\ell - \theta) \frac{\sinh \beta y}{\sinh \beta a} \quad (\text{A.36})$$

at time $t = \beta\ell/\omega$.

Using the spatial distribution of charge density and velocity in Eq. A.7 for P_g yields, after a change of variables, the same equation as before:

$$P_g = -\frac{h}{\lambda} \int_0^y dz_1 \int_0^a dy \rho_{\text{beam}} (\dot{y} E_{y\text{RF}} + \dot{z} E_{z\text{RF}}) , \quad (\text{A.37})$$

or substituting Eqs. A.35 and A.36 gives

$$P_g = \frac{h\beta}{\lambda} \int_0^\lambda dz_1 \int_0^a dy \rho_{\text{beam}}(y, z_1) \left[\dot{y} \frac{\cosh \beta y}{\sinh \beta a} \cdot \sin(\beta z_1 + 2\beta\ell - \theta) + \dot{z} \frac{\sinh \beta y}{\sinh \beta a} \cos(\beta z_1 + 2\beta\ell - \theta) \right] . (\text{A.38})$$

Define expressions AIN and AOUT exactly as in Eqs. A.24 and A.25. The expression for P_g becomes

$$\frac{P_g}{V_1} = \beta \left(\frac{\Delta z}{\Delta t} \right) \left(\frac{2q}{\lambda} \right) \left[\text{AIN} \cos(\theta - 2\beta\ell) + \text{AOUT} \sin(\theta - 2\beta\ell) \right] . (\text{A.39})$$

The corresponding expression for R_g is derived by replacing ωt by $\omega t - (\pi/2)$, or equivalently, by replacing θ by $\theta + (\pi/2)$ to give

$$\frac{R_g}{V_1} = \beta \left(\frac{\Delta z}{\Delta t} \right) \left(\frac{2q}{\lambda} \right) \left[-\text{AIN} \sin(\theta - 2\beta\ell) + \text{AOUT} \cos(\theta - 2\beta\ell) \right] . (\text{A.40})$$

For computational convenience, the term $-2\beta\ell$ is included in the definition of $\theta(\ell)$, and the equivalent of Eq. A.31 actually solved by the program is

$$\frac{d\theta}{d(\beta\ell)} = -2 + \frac{Z_0 R_g}{\beta V_1^2} . \quad (\text{A.41})$$

APPENDIX B

LINEARIZED TRANSMISSION-LINE EQUATIONS

B.1 Analytical Equations. The basic one-dimensional transmission-line equation is given by Rowe⁷ as

$$\frac{\partial^2 V(z,t)}{\partial z^2} - \frac{1}{v_o^2(z)} \frac{\partial^2 V(z,t)}{\partial t^2} - \frac{\partial}{\partial z} \ln \left[\frac{Z_o(z)}{v_o(z)} \right] \frac{\partial V(z,t)}{\partial z} - \frac{2\alpha(z)}{v_o(z)} \cdot \frac{\partial V(z,t)}{\partial t} = \pm \frac{Z_o(z)}{v_o(z)} \left[\frac{\partial^2 \rho(z,t)}{\partial t^2} + 2v_o(z)\alpha(z) \frac{\partial \rho(z,t)}{\partial t} \right] \quad (B.1)$$

The notation used is as follows:

- z = distance along the tube in the beam-drift direction (m),
- t = time (s),
- $V(z,t)$ = potential (V) in the interaction region as measured at the level of the RF circuit,
- $v_o(z)$ = cold-circuit phase velocity (m/s); may be tapered by the designer,
- $Z_o(z)$ = interaction impedance at the level of the RF circuit (Ω), may be tapered,
- $\alpha(z)$ = exponential decay constant for cold-circuit voltage loss (m^{-1}), corresponding to $\omega Cd(z)/v_o(z)$ in Rowe's⁷ equation,
- $\rho(z,t)$ = charge per unit length (C/m) induced on the circuit at position z and time t .

The plus sign on the right-hand side is used for the backward-wave device. The attenuation constant α is positive for a forward wave and negative for a backward wave.

Let the voltage V be given by

$$V(z,t) = \text{Re}\{jV_1(z) \exp j [\omega t - \beta(z)z - \theta(z)]\} \quad (B.2)$$

The amplitude $V_1(z)$ varies slowly; i.e., its fractional change in one RF wavelength ($2\pi/\beta$) is small. The term β is the cold-circuit phase constant, $\omega/v_0(z)$, and varies with position only if the slow-wave structure is physically tapered.

The charge per unit length is given by

$$\rho(z,t) = \text{Re}\{j(C + jD) \exp j[\omega t - \beta(z)z - \theta(z)]\} \quad , \quad (\text{B.3})$$

where $C + jD$ is the complex amplitude of the time harmonic of frequency $\omega/2\pi$ and the space harmonic of wave number β for the induced charge per unit length on the circuit.

Substituting Eqs. B.2 and B.3 in Eq. B.1, neglecting the second derivatives, and assuming that $d\theta/dz \ll \beta$ gives the linearized equations as follows:

$$\frac{dV_1}{dz} = -\alpha V_1 \pm \frac{Z_0}{2\omega} (-\omega^2 D + 2\alpha v_0 \omega C) \quad (\text{B.4})$$

and

$$\frac{d\theta}{dz} = \pm \frac{Z_0}{2\omega V_1} (-\omega^2 C - 2\alpha v_0 \omega D) \quad . \quad (\text{B.5})$$

The interaction region is a reference frame of length $2\pi/\beta$ moving with the speed ω/β so that the position ℓ of the trailing end is given by

$$\beta \ell = \omega t \quad (\text{B.6})$$

in the case where β is constant, or by

$$\int_0^\ell \beta(z) dz = \omega t \quad (\text{B.7})$$

for a tapered circuit. Let the coordinates relative to the reference frame be (y, z_1) . Then the Fourier components C and D are given as

$$C = \frac{2h}{\lambda} \int_0^\lambda dz_1 \int_0^a dy \rho_{\text{beam}}(y, z_1) \frac{\sinh \beta y}{\sinh \beta a} \sin[\beta z_1 + \theta(\ell)] \quad (\text{B.8})$$

and

$$D = -\frac{2h}{\lambda} \int_0^\lambda dz_1 \int_0^a dy \rho_{\text{beam}}(y, z_1) \frac{\sinh \beta y}{\sinh \beta a} \cos[\beta z_1 + \theta(\ell)] \quad (\text{B.9})$$

where

- h = beam width in the magnetic-field direction,
- λ = periodic length, $2\pi/\beta$, of the interaction region,
- a = anode-sole spacing,
- y = height above the sole surface,
- ρ_{beam} = charge per unit volume in the beam, treated as uniform over the width h ,
- z_1 = distance from the left end of the reference frame in the direction of the RF phase velocity.

Here the time distribution required in Eq. B.3 is replaced by a spatial distribution over the interaction region $\ell \leq z \leq \ell + \lambda$, and the variations of θ and V_1 over the wavelength λ are neglected.

In the program, the voltage and distance are normalized and the integrals in Eqs. B.8 and B.9 are replaced by sums over the rods in the interaction region at each time step. Notice that the hot RF wave changes phase relative to the interaction region as the phase θ varies.

It can be shown that the present equations become identical to those of Yu et al.⁸ under the following conditions:

1. The term A_r of Yu et al.⁸ equals βV_1 of Eqs. B.4 and B.5.
2. The terms $2\alpha v_0 \omega C$ and $2\alpha v_0 \omega D$ in Eqs. B.4 and B.5 are neglected.
3. The impedance Z_0 and the impedance defined by Yu et al. in terms of power flow are taken to be equal.
4. The electrons all move with the velocity components given by $dy/dt = 0$ and $dz/dt = \omega/\beta$.
5. The term $[\beta z + \theta(z)]$ of Eq. B.3 equals the term $\int_0^z \beta(z') dz'$ of the equations of Yu et al.⁸
6. The plus sign is taken for both forward and backward waves in Eq. B.5. (This appears to be an error in the Yu et al. paper.⁸)

B.2 Program Equations. To derive the equations of the computer program, define expressions AIN and AOUT by the equations

$$AIN = \sum_{\substack{\text{all charge in} \\ \text{interaction} \\ \text{frame}}} CG \frac{\sinh \beta y}{\sinh \beta a} \cos \beta z_1 \quad (B.10)$$

and

$$AOUT = \sum_{\substack{\text{all charge in} \\ \text{interaction} \\ \text{frame}}} CG \frac{\sinh \beta y}{\sinh \beta a} \sin \beta z_1 \quad (B.11)$$

using the same notation as in Appendix A. Then, combining Eqs. B.8 through B.11, it can be seen that

$$C = \frac{2q}{\lambda}(AIN \sin \theta + AOUT \cos \theta) \quad (B.12)$$

and

$$D = \frac{2q}{\lambda}(-AIN \cos \theta + AOUT \sin \theta) \quad , \quad (B.13)$$

where q is the rod charge (a negative number).

For the case of integration of the backward-wave transmission line equations in the direction opposite the wave motion, replacing z by $-z$ and using the minus sign as in Eqs. A.2 and A.3, Eqs. B.4 and B.5 become

$$\frac{dV_1}{dz} = \alpha V_1 + \frac{Z_0}{2\omega}(-\omega^2 D + 2\alpha v_0 C) \quad (B.14)$$

and

$$\frac{d\theta}{dz} = \frac{Z_0}{2\omega V_1}(-\omega^2 C - 2\alpha v_0 D) \quad . \quad (B.15)$$

Define the RF voltage now as

$$V_{RF} = \text{Re}\{-jV_1(z) \exp j[\omega t + \beta z - \theta(z)]\} \quad (B.16)$$

and the charge per unit length as

$$\rho = \text{Re}\{-j(C + jD) \exp j[\omega t + \beta z - \theta(z)]\} \quad . \quad (B.17)$$

Replacing $\omega t + \beta z$ by $2\beta\ell + \beta z_1$ and defining terms AIN and AOUT as in Eqs. B.10 and B.11, it is seen that

$$C = \frac{2q}{\lambda}[-AIN \sin(\theta - 2\beta\ell) + AOUT \cos(\theta - 2\beta\ell)] \quad (B.18)$$

and

$$D = \frac{2q}{\lambda}[AIN \cos(\theta - 2\beta\ell) + AOUT \sin(\theta - 2\beta\ell)] \quad . \quad (B.19)$$

APPENDIX C

EQUATIONS OF MOTION WITH RECTANGULAR GEOMETRY

The equation of motion of a particle of charge q and mass m in an electric field \bar{E} and magnetic field \bar{B} is

$$\frac{d\bar{v}}{dt} = \frac{q}{m}(\bar{E} + \bar{v} \times \bar{B}) \quad . \quad (C.1)$$

In the present two-dimensional model, the velocity \bar{v} has components $(0, v_y, v_z)$, the electric field \bar{E} is $(0, E_y, E_z)$ and the transverse magnetic field \bar{B} is $(B, 0, 0)$.

Computations use a discrete time step Δt , normally one-twentieth of a cyclotron period. The coordinates \bar{x}_p or (y, z) at time t and the velocity \bar{v}_p or (v_y, v_z) at time $t - \Delta t/2$ are stored between successive steps.

The integration over one time step proceeds in three stages, as follows, using a method described by Boris:¹⁸

1. Evaluate the electric field \bar{E} at position \bar{x}_p .

2. Advance the velocity in three stages:

a. Account for the effect of the electric field by letting

$$\bar{v}_1 = \bar{v}_p + \left(\frac{q}{m}\right)\left(\frac{\bar{E}}{2}\right)\Delta t \quad . \quad (C.2)$$

The assumption is implicit that the electric field \bar{E} changes negligibly in one step.

b. Apply the rotation caused by the magnetic field by defining

$$\bar{v}_2 = \bar{v}_1 \left(\frac{1 - \phi^2}{1 + \phi^2} \right) + \frac{2\phi}{1 + \phi^2} \frac{\bar{v}_1 \times \bar{B}}{|\bar{B}|} \quad , \quad (C.3)$$

where

$$\phi = \tan\left(\frac{qB}{2m}\right) . \quad (C.4)$$

(This solution has an error of order $|E/B|\phi^2$ and is exact in the absence of the electric field.) The rod charge q is negative for an electron stream, and the magnetic field B is negative if it is directed in the negative x direction, as when the electron stream is traveling in the negative z direction.

c. Advance the velocity again to give

$$\bar{v}_N = \bar{v}_2 + \left(\frac{q}{m}\right)\left(\frac{\bar{E}}{2}\right)\Delta t . \quad (C.5)$$

3. Advance the particle position so that

$$\bar{x}_N = \bar{x}_p + \bar{v}_N\Delta t . \quad (C.6)$$

4. Check for interception at the anode or sole and correct the z -coordinate by adding or subtracting one wavelength if the particle has left the left or right end of the interaction region. Particles intercepted are removed from the calculation and are counted to determine currents, bombardment energies and the number of secondary electrons to be emitted at the sole before the next step.

5. Finally, store the new position and velocity, \bar{x}_N and \bar{v}_N , for the charge-density calculation and the next step.

In an alternative scheme, also described by Boris,¹⁸ the equation of motion is transformed by defining

$$\bar{v}_1 = \bar{v} - \frac{\bar{E} \times \bar{B}}{B^2} \quad (C.7)$$

and becomes

$$\frac{d\bar{v}_1}{dt} = \frac{q}{m}(\bar{v}_1 \times \bar{B}) \quad , \quad (C.8)$$

as can be seen by direct substitution with $\bar{E} \cdot \bar{B} = 0$. The above equation is solved as in step 2 above. This method gives the exact velocity for constant \bar{E} . Both methods have been tested in the present model with almost identical results.

A third scheme is described by Yu et al.⁸ and was used in previous versions of this program for motion relative to a moving frame. The equations of this scheme give cycloidal motion for both positions and velocities and include the magnetic force due to the frame motion as an equivalent electric field. Unfortunately, these equations have proven to be numerically unstable, even with no RF drive and negligible space-charge forces, causing charge to drift to the anode instead of maintaining an average direction of motion perpendicular to the electric and magnetic fields. Consequently, this method has been replaced by the finite-step method described above.

In developing the cylindrical method (Appendix D), SAI has used a fourth scheme, which has also been used by Vaughan¹⁰ with a rectangular geometry. These equations also give exact cycloidal trajectories for uniform fields. The solution is stable even for a time step as large as one-third the cyclotron period; however, the method of Eqs. C.1 through C.5 is computationally faster.

APPENDIX D

EQUATIONS OF MOTION WITH CYLINDRICAL GEOMETRY

This procedure uses a coordinate transformation to a local rectangular coordinate system.¹⁸ Let the particle coordinates and velocity be (r, θ) and $(\dot{r}, r\dot{\theta})$ in cylindrical coordinates (r, θ, z) . At the start of the time step, define local coordinates as

$$x_p = 0 \tag{D.1}$$

and

$$y_p = r \tag{D.2}$$

and the velocity as

$$v_{xp} = r\dot{\theta} \tag{D.3}$$

and

$$v_{yp} = \dot{r} \tag{D.4}$$

with the local electric field components

$$E_x = E_\theta \tag{D.5}$$

and

$$E_y = E_r \tag{D.6}$$

Next, the particle equation of motion (Eq. C.1) is solved for the new position (x_n, y_n) and velocity (v_{xn}, v_{yn}) . The scheme described by Vaughan¹⁰ is used to give cycloidal

trajectories which would be exact in a uniform electric and magnetic field. (The velocity part of this algorithm is equivalent to Eqs. C.7 and C.8.)

Finally, the new cylindrical coordinates are computed using the equations

$$r_n = \sqrt{x_n^2 + y_n^2} \quad (\text{D.7})$$

and

$$\theta_n = \tan^{-1}(x_n/y_n) + \theta_p, \quad (\text{D.8})$$

where θ_p is the previous angular position, and the new velocity $(\dot{r}_n, r_n \dot{\theta}_n)$ is given by

$$\dot{r}_n = v_{yn} \frac{y_n}{r_n} + v_{xn} \frac{x_n}{r_n} \quad (\text{D.9})$$

and

$$r_n \dot{\theta}_n = -v_{yn} \frac{x_n}{r_n} + v_{xn} \frac{y_n}{r_n}, \quad (\text{D.10})$$

a rotation of the coordinate system through the angle $\tan^{-1}(x_n/y_n)$.

The dc electric field is radial and equal to $-V_a/r \ln(r_a/r_s)$ at radius r , where V_a is the anode-sole voltage, r_a is the anode radius and r_s is the sole radius. Space-charge fields are not included. The RF field is calculated as described in Appendix E.

To compute accurately, the impact energy requires a small time step since a small percentage error in the total potential

and kinetic energy (which includes the anode-sole voltage of several kV) leads to a significant error in the sole bombardment energy, which is only a few eV. At the point where a trajectory intercepts the sole, the motion is recomputed over the interception step with a reduced time interval. This procedure gives the interception energy and phase more precisely. (The RF fields are not recomputed during these reduced time steps.) The number of reduced time intervals used is an input variable. At present, one-tenth the normal time step is used.

With time steps of $1/10$, $1/20$, $1/200$, $1/400$ and $1/800$ the cyclotron period, the total kinetic and potential energy are conserved to within 2.96, 1.48, 0.14, 0.07 and 0.04 percent, respectively, for a single particle in the direct field.

To reduce rounding error, the program is run on the Michigan State University CDC-6500 computer which gives approximately 14 decimal places in single precision compared with 7.2 decimal places on The University of Michigan Amdahl 470V/6 computer. For the results presented in Section IX, 800 time steps per cyclotron period are used. From a comparison of runs with 800 and 400 such steps, the estimated computational error in the impact energy is about 9 eV for an anode-sole voltage of 24,300 V and a maximum impact energy of 112 eV.

APPENDIX E

RF-CIRCUIT FIELDS IN THE CYLINDRICAL CFA MODEL

The anode is treated as a set of segments (vanes) equally spaced around the interaction region. The RF voltage and phase are given for vane j as V_{RFj} and ϕ_j . Then the RF field (E_r, E_θ) at position (r, θ) at time t is given by

$$E_r(r, \theta) = \sum_{j=1}^{NVANES} V_{RFj} G_r[r, (\theta - \theta_j)] \cos(\omega t - \phi_j) \quad (E.1)$$

and

$$E_\theta(r, \theta) = \sum_{j=1}^{NVANES} V_{RFj} G_\theta[r, (\theta - \theta_j)] \cos(\omega t - \phi_j) , \quad (E.2)$$

where θ_j is the angular position of vane j .

The vector (G_r, G_θ) is the Green's function which equals the electric field due to a single vane at unit potential. The electric field is assumed to be uniform in the gaps between adjacent vanes. The corresponding potential has been derived by Surti.¹¹ The present model stores the electric field components in two separate arrays for greater accuracy.

Define the following notations:

θ_B = one-half the angle subtended at the axis by the gap between adjacent vanes.

θ_G = one-half the pitch angle subtended by one vane and its adjacent gap,

r_a = anode radius,

r_s = sole radius.

Then the fields $G_r(r, \theta)$ and $G_\theta(r, \theta)$, with θ relative to a vane at $\theta_j = 0$, are given by

$$G_r = - \sum_{k=1}^{\infty} f_k \left[\left(\frac{r}{r_a} \right)^{k-1} + \left(\frac{r_s}{r_a} \right)^{2k} \left(\frac{r}{r_a} \right)^{-(k+1)} \right] \cos k\theta \quad (E.3)$$

and

$$G_\theta = \sum_{k=1}^{\infty} f_k \left[\left(\frac{r}{r_a} \right)^{k-1} - \left(\frac{r_s}{r_a} \right)^{2k} \left(\frac{r}{r_a} \right)^{-(k+1)} \right] \sin k\theta \quad , \quad (E.4)$$

where

$$f_k = \frac{2 \sin k\theta_B \sin k\theta_G}{\pi k \theta_G r_a \left[1 - (r_s/r_a)^{2k} \right]} \quad . \quad (E.5)$$

Following Surti,¹¹ the coefficients f_k have been derived by Fourier analysis of the electric field on the anode. The field (G_r, G_θ) has zero divergence and curl to satisfy Maxwell's equations for a quasistatic field.

In the model, 100 terms of the series suffice up to half way from the sole to the anode. At greater radii, 500 terms are used. The fields are evaluated on a 41 x 41 mesh. Because of the symmetry in θ , only the fields for positive θ need to be stored. The mesh covers values of θ up to 2.5 vanes distant from the reference vanes, as trials show that the field components are less than six percent of their maximum values outside this range. On the anode, the radial field is extrapolated linearly from the two nearest mesh points and the angular field is known exactly. The local

field at position (r, θ) is calculated for a given particle by area-weighting the contributions from the four nearest mesh points, treating the mesh as locally rectangular.

The vane RF voltage V corresponding to RF power P is given by

$$V_0 = \sqrt{2Z_0 P} \quad , \quad (E.6)$$

where Z_0 is defined as the input impedance of the vane circuit. The corresponding interaction impedance Z_{int} for the fundamental space harmonic is given by

$$Z_{int} = \frac{E_{RF}^2}{2\beta^2 P} \quad , \quad (E.7)$$

where E_{RF} is the fundamental space harmonic amplitude of the electric field on the circuit and β is the corresponding wavenumber.

The wavenumber β is related to the vane period p and the phase shift ϕ per vane (as seen by the beam) by

$$\beta p = \phi \quad . \quad (E.8)$$

Neglect the reentrancy of the structure, assume that the total electric field is uniform between the vane tips and perform a spatial Fourier analysis to relate the terms E_{RF} and V_{RF} . The result is¹⁹

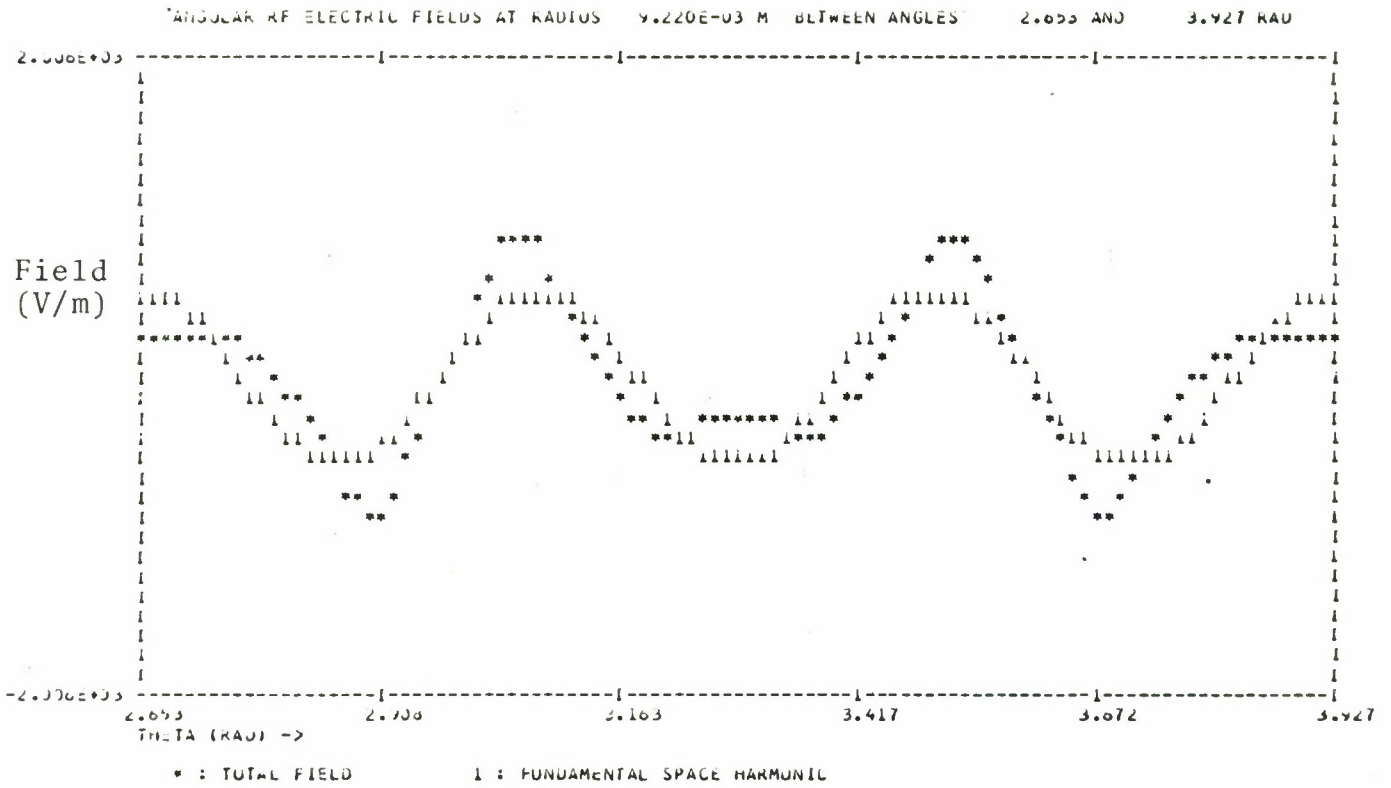
$$\frac{Z_{int}}{Z_0} = \left(\frac{\sin \phi/2}{\phi/2} \frac{\sin \alpha\phi/2}{\alpha\phi/2} \right)^2 \quad , \quad (E.9)$$

where α is the ratio (gap length)/(vane period), or θ_B/θ_G , in the previous notation. Then the RF space-harmonic amplitude V_{RF} is given as

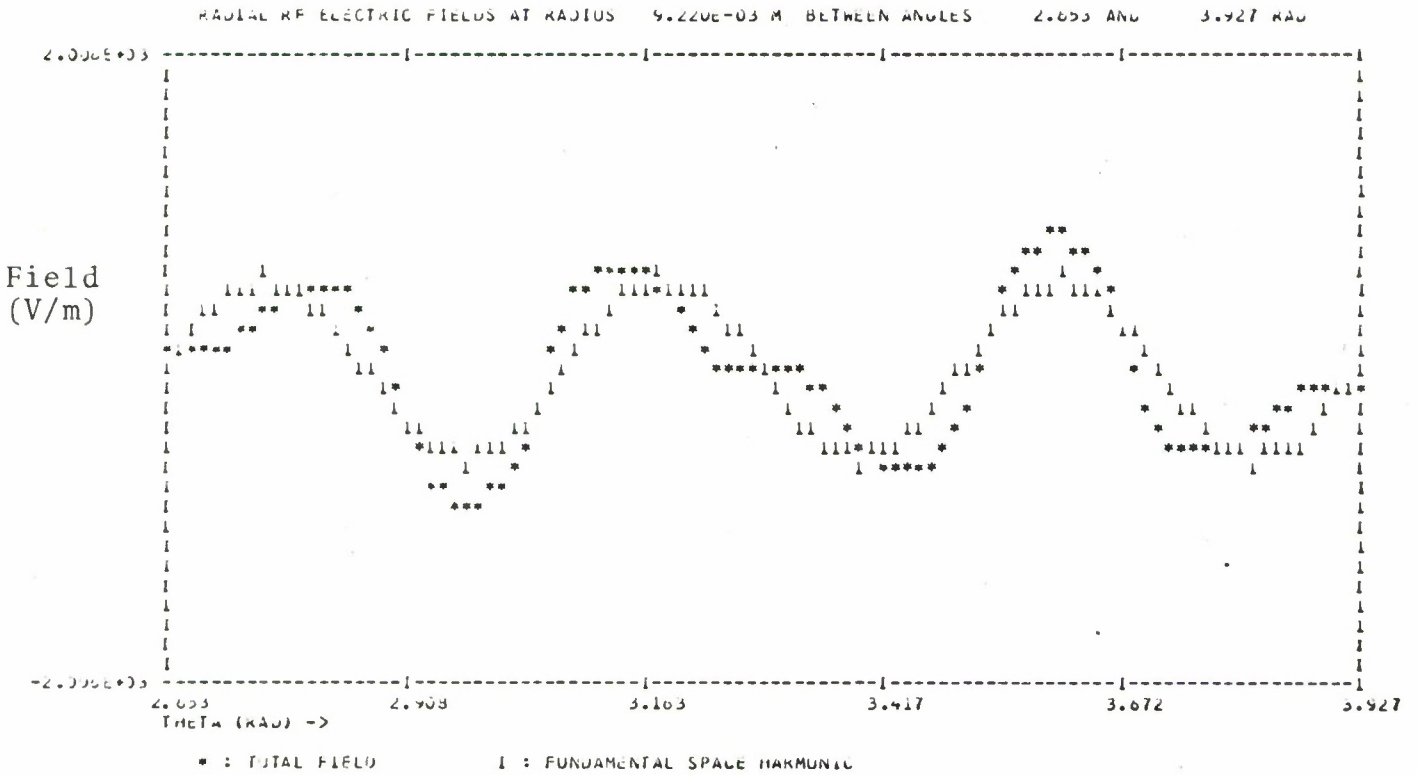
$$V_{RF} = \sqrt{2Z_{int}P} \quad . \quad (E.10)$$

In Figs. E.1, E.2 and E.3, the total fields are compared with the analytical values for the fundamental space harmonic in rectangular coordinates. The single space harmonic is used in the rectangular CFA program and the field expressions are given in Appendix A. The numerical values correspond to the QKS 1842 tube with an anode radius of 9.708 mm and a sole radius of 7.748 mm. All the vanes have the same voltage amplitude of 287 V (corresponding to an RF power of 5.5 kW). The voltage on successive vanes differs in phase by 133 degrees in the direction of wave motion as seen by the beam in the backward-wave tube. Equivalently, the phase shift in the input-output direction is 47 degrees since the voltages on alternate vanes have opposite signs because of the strap connections.

The single space harmonic is a good approximation at radii of 9.2 mm and less (Fig. E.1). Closer to the anode, the exact field shows more rapid variations than the simple cosine curve (Fig. E.2). Both fields are negligible throughout 70 percent of the sever region (Fig. E.3).

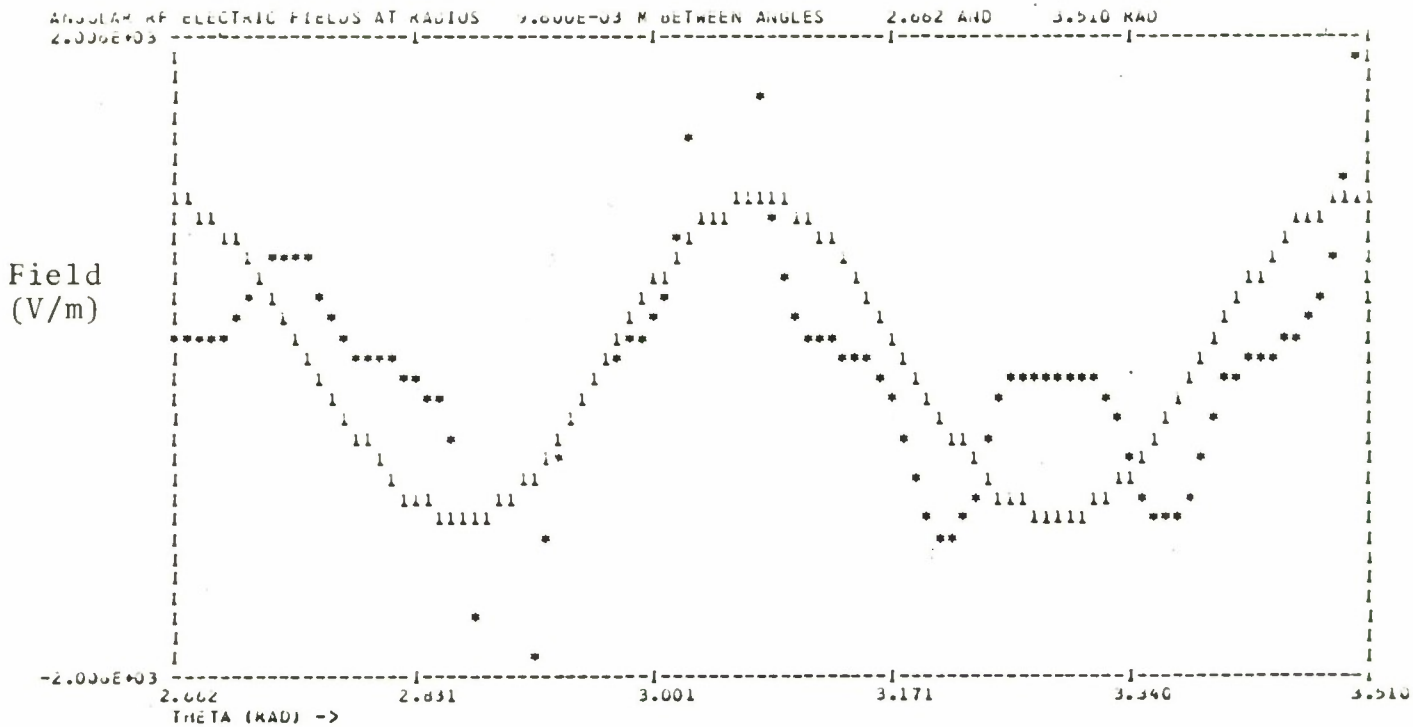


a. Angular Fields

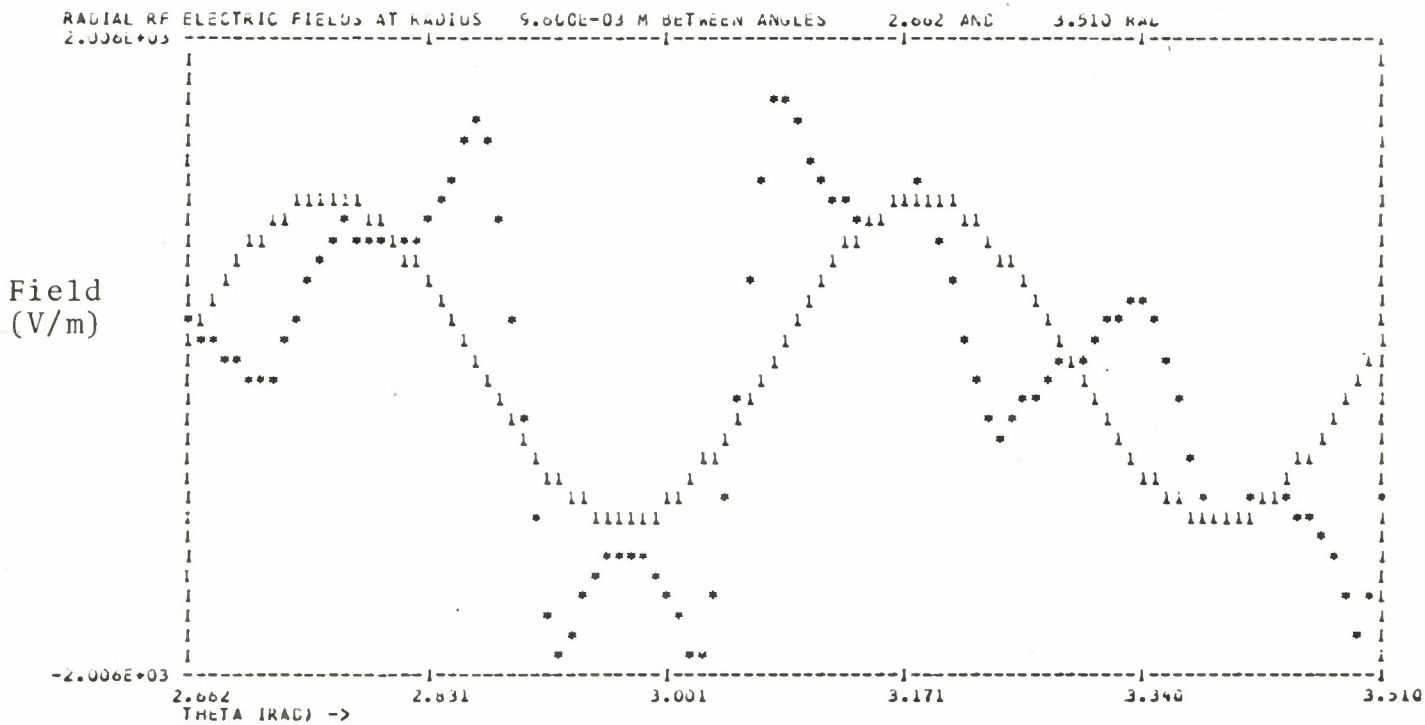


b. Radial Fields

FIG. E.1 COMPARISON OF EXACT VALUES AND SINGLE SPACE HARMONIC OF RF-CIRCUIT FIELDS IN THE QKS 1842 AT RADIUS 9.2 mm.

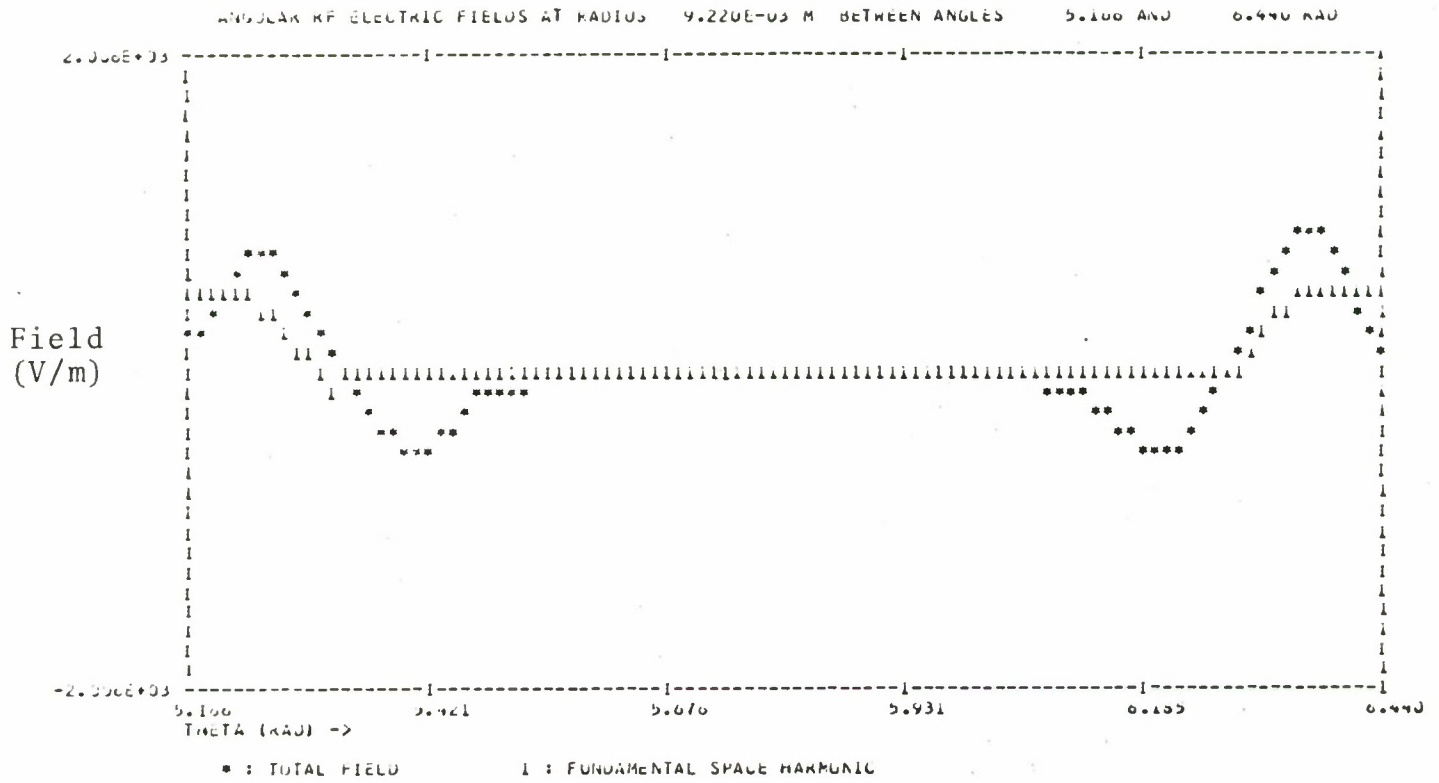


a. Angular Fields

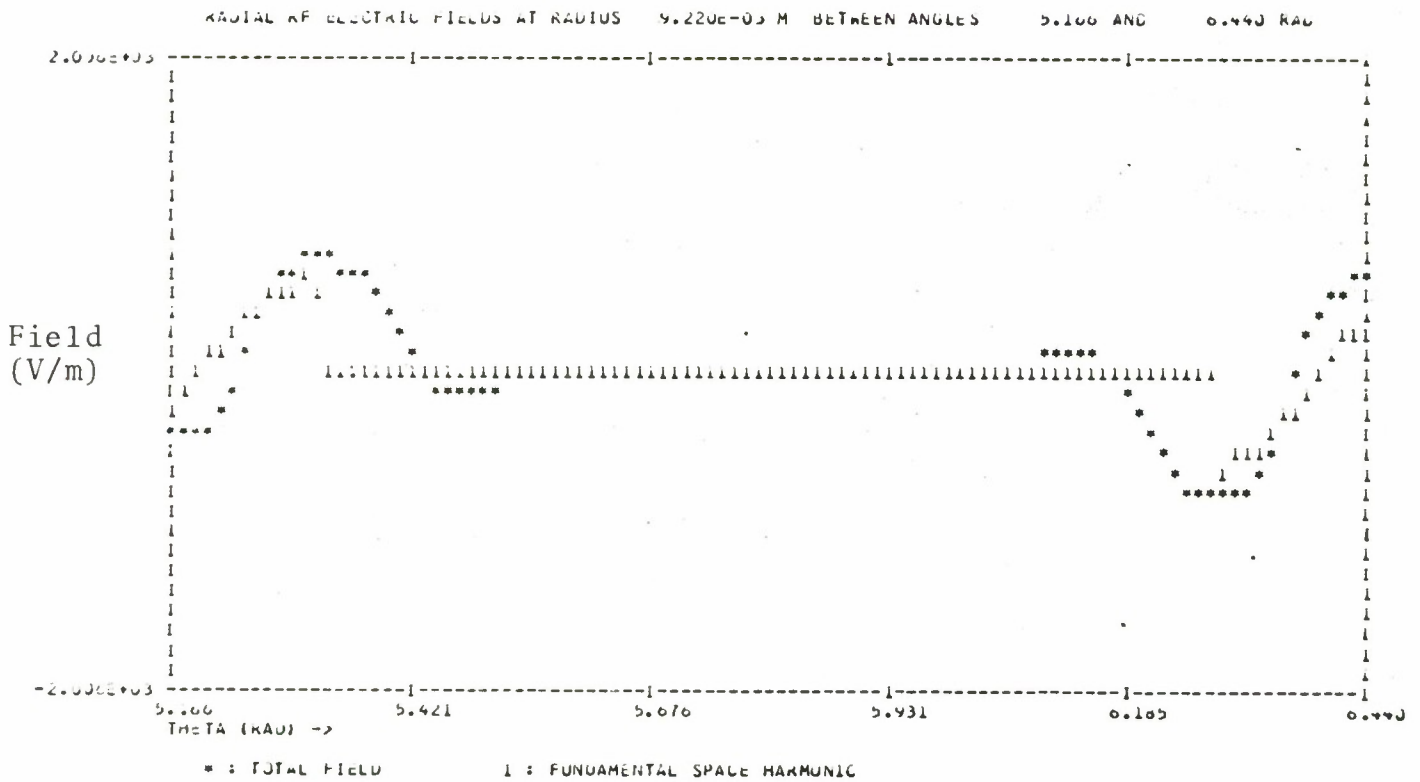


b. Radial Fields

FIG. E.2 COMPARISON OF EXACT VALUES AND SINGLE SPACE HARMONIC OF RF-CIRCUIT FIELDS IN THE QKS 1842 AT RADIUS 9.6 mm.



a. Angular Fields



b. Radial Fields

FIG. E.3 COMPARISON OF EXACT VALUES AND SINGLE SPACE HARMONIC OF RF-CIRCUIT FIELDS IN SEVER REGION OF THE QKS 1842.

REFERENCES

1. D. M. MacGregor and J. E. Rowe, "Analysis of Distributed-Emission Crossed-Field Amplifiers," Progress Report, MIT Lincoln Laboratory, Purchase Order CX-1256, Shared Applications, Inc., Ann Arbor, MI; January 1977.
2. E. K. Shaw, "Starting in the Cold Cathode Distributed Emission Crossed Field Amplifier," IEEE Trans. Electron Devices, vol. ED-24, No. 1, pp. 22-26; January 1977.
3. D. M. MacGregor and J. E. Rowe, "Computer Modeling and Simulation of Crossed-Field Amplifiers," Final Report, MIT Lincoln Laboratory, Purchase Order CX-1109, Shared Applications, Inc., Ann Arbor, MI; November 1976.
4. "CFA Design Improvement Program," Semi-Annual Report July 1, 1975-December 31, 1975, Contract No. N00123-75-C-1294, Varian Associates, Beverly, MA; March 1976.
5. "CFA Design Improvement Program," Second Semi-Annual Report, January 1, 1976-June 30, 1976, Contract No. N00123-75-C-1294, Varian Associates, Beverly, MA; October 1976.
6. J. W. Sedin, "A Large-Signal Analysis of Beam-Type Crossed-Field Traveling-Wave Tubes," IRE Trans. Electron Devices, vol. ED-9, No. 1, pp. 41-50; January 1962.
7. J. E. Rowe, Nonlinear Electron-Wave Interaction Phenomena, Academic Press, New York; 1965.
8. S. P. Yu, G. P. Kooyers and O. Buneman, "Time-Dependent Computer Analysis of Electron-Wave Interaction in Crossed Fields," J. Appl. Phys., vol. 36, No. 8, pp. 2550-2559; August 1965.
9. D. Potter, Computational Physics, John Wiley & Sons, New York; 1973.
10. J. R. M. Vaughan, "Beam Buildup in a DEMATRON Amplifier," IEEE Trans. Electron Devices, vol. ED-18, No. 6, pp. 365-373; June 1971.
11. G. E. Dombrowski and W. C. Price, "Analytic and Experimental Study of Reentrant Stream Crossed-Field Amplifiers," NASA CR-72442, University of Connecticut, Storrs, CT; 1968.
12. K. K. Surti, "Computer Simulation of Microwave Devices," Ph.D. Thesis, University of Connecticut; 1974 (University Microfilms Order No. 74-21811, Ann Arbor, MI).

13. G. E. Dombrowski, "Theory of the Amplitron," IRE Trans. Electron Devices, vol. ED-6, No. 4, pp. 419-428; October 1959.
14. W. A. Smith, "A Wave Treatment of the Continuous Cathode Crossed-Field Amplifier," IRE Trans. Electron Devices, vol. ED-9, No. 5, pp. 379-387; September 1962.
15. H. Steyskal, "Continuous Cathode Crossed-Field Amplifiers," IEEE Trans. Electron Devices, vol. ED-10, No. 2, pp. 95-96; March 1963.
16. D. M. MacGregor and J. E. Rowe, "Manual for Crossed-Field Amplifier Analysis Program," prepared for Naval Electronics Laboratory Center, Shared Applications, Inc., Ann Arbor, MI; August 1976.
17. D. M. MacGregor and J. E. Rowe, "Computer Program for Crossed-Field Amplifier Analysis," Final Report, Task Order 75-382; Project Period 30 June 1975-15 August 1976, prepared for Battelle Columbus Laboratories and Naval Electronics Laboratory Center, Shared Applications, Inc., Ann Arbor, MI; August 1976.
18. J. P. Boris, "Relativistic Plasma Simulation-Optimization of a Hybrid Code," Proc. Fourth Conf. on Numerical Simulation of Plasmas, Washington, D.C., pp. 3-67; November 2-3, 1970.
19. J. C. Walling, "Interdigital and Other Slow Wave Structures," J. of Electronics and Control, vol. 3, pp. 239-258; September 1957.